Ocean-atmosphere interactions in cyclones and their predictability

Tropical and extra-tropical cyclones

Alison Cobb

Supervisor: Dr. Arnaud Czaja

Department of Physics
Imperial College

This dissertation is submitted for the degree of
Doctor of Philosophy

February 2019

Declaration

I hereby declare that except where specific reference is made to the work of others, the contents of this dissertation are original and have not been submitted in whole or in part for consideration for any other degree or qualification in this, or any other university. This dissertation is my own work and contains nothing which is the outcome of work done in collaboration with others, except as specified in the text and Acknowledgements. Part of this work has been submitted for publication [1]

Alison Cobb
February 2019

[1] Cobb, A. & Czaja, A. (2018). Mesoscale signature of the North Atlantic Oscillation and its interaction with the ocean. Submitted to Geophysical Research Letters, October 2018

Copyright declaration

The copyright of this thesis rests with the author and is made available under a Creative Commons Attribution Non-Commercial No Derivatives licence. Researchers are free to copy, distribute or transmit the thesis on the condition that they attribute it, that they do not use it for commercial purposes and that they do not alter, transform or build upon it. For any reuse or redistribution, researchers must make clear to others the licence terms of this work.

Acknowledgements

I wish to give a huge thank you to my supervisor Dr. Arnaud Czaja. I am truly inspired by our discussions and I aspire to being as knowledgeable a scientist one day. Along with help and encouragement with the PhD work, I thank you for your emotional support, with a constant belief in what I can achieve. I also thank Magdalena Balmaseda and Frederic Vitart at ECMWF for useful discussions and Paul Dando at ECMWF for being an amazing help with data access. Finally, thank you to my parents for supporting my return to study and being a great sounding board, and to Jesse who is always there to make me smile.

Abstract

The first chapter investigates sea surface temperature (SST) as a predictor of western North Pacific tropical cyclones intersecting a domain over southern and central China. Models exist for seasonal prediction of tropical cyclones, but generally they are basin-wide and issued ~3 months before the storm season. This study has revealed a robust empirical signal relating SST off the east coast of mainland China, in the East China Sea and in the Bay of Bengal ~18 months prior to the tropical cyclone season, to activity within the selected domain; however, failed to produce a skilful empirical forecast.

The following two chapters focus on the impact of the Gulf Stream on North Atlantic extra-tropical cyclones. The primary diagnostic analysed is turbulent kinetic energy (on scales of 10 to 100 kms), motivated by Sheldon et al., 2017. They proposed a mechanism for the interaction between ocean and atmosphere, the 'warm path', in which the Gulf Stream warm tongue influences atmospheric instability within an overlying cyclone. A single storm in an 11 member ensemble hindcast, a control forecast, and ERA-Interim reanalysis were analysed. However, even with a very similar warm tongue set up in all ensemble members, the magnitude of turbulent kinetic energy was variable by more than 60%.

For the final chapter, mesoscale signatures of the North Atlantic Oscillation (NAO) in the atmosphere and ocean were identified. In positive NAO winters, an extension of the Gulf Stream warm tongue is observed, along with a displacement and acceleration of surface currents. Mesoscale activity in the atmosphere appears to follow this extension of the warm tongue, which is a new feature of NAO air-sea interactions embedded within the basin scale NAO patterns. This result highlights the importance of model resolution and the presence of unresolved processes in many climate models, which may have downstream impacts and climate implications.

Table of contents

List of figures **xv**

List of tables **xxvii**

List of abbreviations **xxix**

1 Introduction **1**
1.1 Thesis outline 4

2 Background physics **5**
2.1 Formation and structure 5
2.2 Storm tracks and intensity 10
2.2.1 Influence of the ocean 10
2.2.2 Influence of atmospheric environmental conditions 12
2.3 Tropical cyclone variability in the West Pacific 13
2.4 Extra-tropical cyclone variability in the North Atlantic 17
2.5 Long-term variability 20
2.6 Observational record 21
2.7 Representation in GCMs 22
2.8 Atmospheric forces in cyclones 23
2.8.1 Geostrophic balance 24
2.8.2 Gradient wind balance 24
2.8.3 Gravitational instability and upright convection 25
2.8.4 Inertial instability and horizontal movement 26
2.8.5 Symmetric instability and slantwise convection 27
2.9 Conclusion 30

3 Seasonal predictability of tropical storms in southern and central China **31**
3.1 Introduction 31

3.1.1 Tropical storm forecasting techniques . . . 31
3.2 Research question . . . 33
3.2.1 Aims . . . 34
3.3 Methods . . . 34
3.3.1 Tropical storm data . . . 34
3.3.2 Large-scale environmental data . . . 36
3.3.3 Correlation analysis . . . 37
3.4 Results . . . 37
3.4.1 Storm activity . . . 37
3.4.2 Correlation between storm activity and large-scale variables . . . 38
3.4.3 Statistical model using SST . . . 53
3.5 Discussion . . . 56
3.6 Conclusions . . . 59

4 Variability of shear instability in an extra-tropical cyclone 61
4.1 Introduction . . . 61
4.1.1 The Gulf Stream . . . 61
4.1.2 The ‘warm path’ . . . 63
4.2 Research question . . . 65
4.2.1 Aims . . . 65
4.3 Data . . . 65
4.3.1 ECMWF Integrated Forecasting System (IFS) . . . 65
4.3.2 Operational forecast . . . 68
4.3.3 Ensemble hindcast . . . 69
4.3.4 Reanalyses . . . 69
4.4 Method . . . 70
4.4.1 Mesoscale diagnostics . . . 70
4.5 Results . . . 73
4.5.1 Ensemble hindcast . . . 73
4.5.2 Operational forecast and ERA-Interim . . . 78
4.5.3 Summary comparison of all datasets . . . 82
4.6 Discussion . . . 83
4.7 Conclusions . . . 86

5 Mesoscale signatures of the North Atlantic Oscillation and interaction with the ocean 87
5.1 Introduction . . . 87

5.2 Research question 88
5.2.1 Aims 88
5.3 Data 89
5.4 Method 90
5.5 Results 92
5.5.1 Mesoscale signature in the ocean 92
5.5.2 Mesoscale signature in the atmosphere 93
5.5.3 Potential vorticity (PV) 96
5.5.4 Comparison with ERA-Interim 100
5.6 Discussion 102
5.7 Conclusions 106

6 Conclusions **109**
6.1 Summary and discussion 109
6.2 Perspectives 111

References **113**

List of figures

1.1 Schematic representation of the trade-offs in climate modelling. Triangles represent surface of approximately constant computer power. Source: Challinor et al. (2009). 1

1.2 The ratio of predictable components (RPC) for seasonal hindcasts of December-January-February (DJF) mean sea level pressure. Stippling identifies where RPC is significantly different to one at the 90% level. Regions of negative correlation are masked out as they imply zero skill. Source: Eade et al. (2014). 3

1.3 Modelled response to Oyashio Extension shift, with variability in this frontal region projecting onto the larger-scale. The mean December–March difference in 300 hPa geopotential height over the North Pacific for the a) high resolution (0.25°) and b) low resolution (1°) simulations. The black contour denotes areas significant at the 95% confidence level based on a Student's t test. Source: Smirnov et al. (2015). 4

2.1 Comparison of a tropical cyclone and an extra-tropical cyclone. The top schematics show horizontal maps of the surface temperature, pressure, and wind fields associated with a tropical cyclone (left) and an extra-tropical cyclone (right). Colours indicate temperature (blue 15°C, blue green 20°C, green 25°C). Dashed lines indicate surface wind speeds. Solid lines are isobars. The bottom schematics show vertical maps of the pressure surfaces, temperature anomalies, and circulation at the surface and tropopause. Source: Merrill (1993) 7

2.2 Conceptual models of cyclone evolution showing lower-tropospheric (e.g. 850 hPa) geopotential height and fronts (top), and lower-tropospheric potential temperature (bottom). (a) Norwegian cyclone model: (I) incipient frontal cyclone, (II) and (III) narrowing warm sector, (IV) occlusion; (b) Shapiro–Keyser cyclone model: (I) incipient frontal cyclone, (II) frontal fracture, (III) frontal T-bone and bent-back front, (IV) frontal T-bone and warm seclusion. The stages in the respective cyclone evolutions are separated by approximately 6–24 h. Source: Schultz et al. (1998) 8
2.3 Schematic showing the warm conveyor belt, cold conveyor belt and dry intrusion. Source: Catto et al. (2010) 9
2.4 SST climatology 1958-2014. (a) JJASO mean (b) JJASO standard deviation (c) JFM mean (d) JFM standard deviation. 14
2.5 Tropical storm tracks during (a) the six strongest warm (El Niño) years (1965, 1972, 1982, 1987, 1991, and 1997) and (b) the six strongest cold (La Niña) years (1970, 1973, 1975, 1988, 1998, and 1999). Source: Wang and Chan (2002) 15
2.6 Point of maximum intensity (plotted by circles) and track (lines) of a) Hainan course and b) Okinawa course typhoons. The reference contoured line of 500 hPa geopotential height on day is also exhibited as a background state. The 5880 m line roughly corresponds to the periphery of the North Pacific subtropical high. Source: Hirata and Kawamura (2014) 16
2.7 The PDO over the historical record (1901–2014). Regression of global monthly SST (shading) and December-January-February (DJF) sea level pressure (contours) anomalies onto the PDO time series. A positive PDO is associated with negative central North Pacific SST anomaly. Source: Newman et al. (2016) 17
2.8 Leading empirical orthogonal functions (EOF 1) of the seasonal mean sea level pressure anomalies (1899-2001) in the North Atlantic sector (20º-70ºN, 90ºW-40ºE). The pattern is obtained by regressing the hemispheric sea level pressure anomalies upon the leading principal component time series. The contour lines are in hPa with an increment of 0.5 hPa, and the zero contour has been excluded. Source: Hurrell et al. (2003) 18
2.9 The pattern of SST anomalies that regress onto NAO+, contour interval 1/10 K, negative regions are stippled. Source: Marshall et al. (2001). 19

2.10 a) Gradient wind balance in the primary circulation of a tropical cyclone b) disruption of gradient wind balance by friction in the boundary layer leaving a net inward pressure gradient that drives the secondary circulation with inflow in the boundary layer and outflow above it. Source: Smith, 2006 . . 25

2.11 Symmetric instability in relation to isentropes and lines of constant absolute momentum (M). a) Unstable to symmetric instability, b) stable to symmetric instability. Isentropes are shown in red dashed lines and lines of constant absolute momentum (M) in solid green. Thickness of the lines increases towards higher values. Both environments are baroclinic and θe and M are low in the bottom left and high in the top right. The black arrows show direction of movement of air parcels. In both panels a and b, if a parcel is moved to the left, it is inertially stable as it is moving towards an area of reduced absolute momentum. In both panels a and b, if a parcel is moved vertically, it is gravitationally stable as potential temperature is increasing in this direction and so the parcel will return to it's original position. However, in panel a, if an air parcel is moved along arrow X, it is moving towards lower potential temperature and high M, so is symmetrically unstable. In panel b, it will move towards higher θe and low M, and is symmetrically stable. Modified from Morcrette (2004) 28

2.12 The streamfunctions for the transverse circulation to a front in a simple experiment in an idealised slantwise unstable atmosphere. The initial potential temperature (θ), wet bulb potential temperature (θw) and absolute momentum (M) are also plotted. Source: Bennetts and Hoskins (1979) . . . 30

3.1 Blue polygon highlights the domain used for this analysis, encompassing parts of southern and central China. 35

3.2 Time series of ACE ('domain') (solid blue line), ACE ('entire') (dashed blue line) and cumulative count (red line) for a) low, b) medium, c) high intensity storms. ACE units 10^4 knots^2. ACE-JJASO ('domain') uses only the 6-hourly points within the specified domain to calculate the ACE of each storm, whereas ACE-JJASO ('entire') uses all 6-hourly time steps for the entire length of the track. 38

3.3 SST-JJASO correlated with ACE (a,c,e,f) and count (b,d,f,h) over the period 1958-2014 for storms separated by intensity and all storms. Low intensity (tropical storms and tropical depressions), medium intensity (categories 1,2), high intensity (categories 3, 4, 5). Stippling indicates grid points with significant correlation at the 95th percentile and solid (dashed) contour lines are shown where correlation values are >=0.4 and <=-0.4. Storm domain shown as blue polygon. 40
3.4 SST anomaly pattern associated with an El Niño event obtained by linearly regressing monthly SST anomalies at each grid box upon the leading Principal Component (PC) time series based on the domains outlined in the black boxes. Source: https://climatedataguide.ucar.edu/climate-data 41
3.5 Time line showing lag between JJASO season in which storm count and ACE are calculated and JFM-1 in the previous year. There are 18 months between February and August of these two years. 41
3.6 SST JFM-1 correlated with ACE (a,c,e,f) and count (b,d,f,h) over the period 1958-2014 for storms separated by intensity and all storms. Low intensity (tropical storms and tropical depressions), medium intensity (categories 1,2), high intensity (categories 3, 4, 5). Stippling indicates grid points with significant correlation at the 95th percentile and solid (dashed) contour lines are shown where correlation values are >=0.4 and <=-0.4. Storm domain shown as blue polygon. Red and purple boxes highlight areas of strong opposing correlations between low and high intensity storm counts. 42
3.7 SST JFM correlated with ACE (a,c,e,f) and count (b,d,f,h) over the period 1958-2014 for storms separated by intensity and all storms. Low intensity (tropical storms and tropical depressions), medium intensity (categories 1,2), high intensity (categories 3, 4, 5). Stippling indicates grid points with significant correlation at the 95th percentile and solid (dashed) contour lines are shown where correlation values are >=0.4 and <=-0.4. Storm domain shown as blue polygon. 43
3.8 The Pacific Decadal Oscillation Index time series 1958-2014. Cold, warm and mixed phases marked. 44

3.9 SST-JJASO correlated with count during (a,d) 1958-1975, (b,d) 1976-1997, (c,f) 1998-2014 for low (tropical storms and tropical depressions) and high intensity storms (categories 3, 4, 5). Stippling shows grid points with significant correlation at 95th percentile and solid (dashed) contour lines are shown where correlation values are >=0.4, <=-0.4. Storm domain shown as blue polygon. 45
3.10 SST JFM-1 correlated with count during (a,d) 1958-1975, (b,d) 1976-1997, (c,f) 1998-2014 for low (tropical storms and tropical depressions) and high intensity storms (categories 3, 4, 5). Stippling shows grid points with significant correlation at 95th percentile and solid (dashed) contour lines are shown where correlation values are >=0.4, <=-0.4. Storm domain shown as blue polygon. 46
3.11 VIT-JJASO correlated with count during 1958-2009 for low intensity storms over a) 100m, c) 300m, and e) 700 m and high intensity storms over b) 100m, d) 300m, and f) 700 m. Stippling shows grid points with significant correlation at 95th percentile and solid (dashed) contour lines are shown where correlation values are >=0.4, <=-0.4. Storm domain shown as blue polygon. 47
3.12 VIT-JFM-1 correlated with count during 1958-2009 for low intensity storms over a) 100m, c) 300m, and e) 700 m and high intensity storms over b) 100m, d) 300m, and f) 700 m. Stippling shows grid points with significant correlation at 95th percentile and solid (dashed) contour lines are shown where correlation values are >=0.4, <=-0.4. Storm domain shown as blue polygon. 48
3.13 Mean sea level pressure climatology 1958-2014. (a) JJASO mean (b) JJASO standard deviation (c) JFM mean (d) JFM standard deviation. 48
3.14 MSLP-JJASO correlated with count during 1958-2013 for (a) low and (b) high intensity storms. MSLP-JFM-1 correlated with count for (c) low and (d) high intensity storms. Stippling shows grid points with significant correlation at 95th percentile and solid (dashed) contour lines are shown where correlation values are >=0.4, <=-0.4. Storm domain shown as blue polygon. 49
3.15 Heat flux climatology 1958-2013. (a) JJASO mean (b) JJASO standard deviation (c) JFM mean (d) JFM standard deviation. 50

3.16 Heat flux and SST correlation schematic. Red arrows represent direction of heat flux into the ocean or atmosphere. Plus and minus signs represent anomaly in heat flux and SST. Positive heat flux is from the ocean to the atmosphere. 51
3.17 HF-JJASO correlated with count during 1958-2013 for (a) low and (b) high intensity storms. HF-JFM-1 correlated with count for (c) low and (d) high intensity storms. Stippling shows grid points with significant correlation at 95th percentile and solid (dashed) contour lines are shown where correlation values are >=0.4, <=-0.4. Storm domain shown as blue polygon. 51
3.18 February SST correlated with heat flux in (a) December, (b) January, (c) February, (d) March, (e) April (1958-2012). Stippling shows grid points with significant correlation at 95th percentile and solid (dashed) contour lines are shown where correlation values are >=0.4, <=-0.4. Storm domain shown as blue polygon. 52
3.19 August SST correlated with heat flux in (a) June, (b) July, (c) August, (d) September, (e) October (1958-2012). Stippling shows grid points with significant correlation at 95th percentile and solid (dashed) contour lines are shown where correlation values are >=0.4, <=-0.4. Storm domain shown as blue polygon. 53
3.20 Time series of count-JJASO observed values (blue lines) and those predicted from the model (green lines) for the a) low intensity and b) high intensity storms. 54
3.21 Time series of ACE-JJASO observed values (blue lines) and those predicted from the model (green lines) for the a) low intensity and b) high intensity storms. ACE units 10^4 knots^2 55
3.22 Scatter plots of a) observed and predicted ACE-JJASO values and b) observed and predicted count-JJASO values for the low intensity (green dots) and high intensity (red dots) storms. ACE units 10^4 knots^2 55
3.23 Difference between Joint Typhoon Warning Center (JTWC) and China Meteorological Agency (CMA) of storm counts that intersected the domain during JJASO (1958-2014). Negative values when CMA>JTWC count and positive values when JTWC>CMA count. 57

4.1 The Gulf Stream, revealed through SST data, made from the AVHRR (Advanced Very High Resolution Radiometer) sensor carried on a NOAA satellite. Source: https://science.nasa.gov/earth-science/oceanography/physical-ocean/currents 62

4.2 Hydrographic section of potential temperature at 37°N. Purple arrow indicates location of warm tongue. Source: http://www.ewoce.org 62
4.3 Number of back trajectories (circles) with height 5km at t=24h and reaching low levels over the ocean at t=0h: red for CNTL, blue for COOL and green for SMTH. The arrows indicate a measure of oceanic forcing when comparing CNTL,SMTH or CNTL,COOL. Normalized such that the number for CNTL at 12km resolution is unity. Source: Sheldon et al. (2017) 63
4.4 Trajectories reaching upper levels flow along the contours of warm SST. Source: Sheldon et al. (2017) 64
4.5 The ECMWF hindcast schedule on 12th January 2017. 20 hindcast years (back to 1996) is run. Each ensemble is made up of 10 members plus 1 control, which reduce in resolution at day 15 and run for a total of 46 days. 'MO' is the Met Office experiment, 'I' is initialisation and 'A' is analysis. . 70
4.6 Domain used to create the low pass for the hindcast data. The hindcast data is at 0.2° resolution and so 15 grid points were used, to give a 2.8° spatial filter. At each grid point, all values within this domain are averaged to create the low pass at that point. 72
4.7 Shear production at 4.5 km (coloured contours) and SST (black contour lines) every 2°C at 12UTC 15th January 2004 in the Met Office a) CNTL and b) SMTH experiments. White dot is location of low pressure centre. . . 73
4.8 Shear production at 500 hPa (coloured contours) and SST (black contour lines) every 2°C between 20°C and 30°C in the hindcast control and 10 ensemble members at 12UTC 15th January. The member name and minimum sea level pressure are given for each plot. Members that were initialised with the same SST share the same colour label. Low pressure centre marked by white dot. The result for the Met Office control run (MO CNTL) at 12UTC 15th January is repeated for comparison (units mW/kg). 74
4.9 Distribution of shear production over the ocean (land masked) at 500 hPa at 12UTC 15th between 25-42°N, 85-60°W. The box extends from the lower to upper quartile values of the data, with a red horizontal line at the median. The whiskers reach from 5th to 95th percentile. Outlier points are not shown. 75

4.10 Shear production at 500 hPa (coloured contours) and SST (black contour lines) every 2°C between 20°C and 30°C in the hindcast control and 10 ensemble members at 00UTC 16th January. The member name and minimum sea level pressure are given for each plot. Members that were initialised with the same SST share the same colour label. Low pressure centre marked by white dot. 76
4.11 Shear production 95th percentile for the Met Office CNTL and SMTH experiments at 12UTC 15th and the hindcast control and members at a) 12UTC 15th and b) 00 UTC 16th. Filled blue dot is the hindcast ensemble control. 77
4.12 Shear production at 500 hPa (coloured contours), SST (black contour lines) every 2°C between 20°C and 30°C and mean sea level pressure every 5 hPa from 900 to 1020 hPa in the hindcast control and 10 ensemble members at 00UTC 17th January. The member name and minimum sea level pressure are given for each plot. Members that were initialised with the same SST share the same colour label. 78
4.13 Ensemble member 9 at a,d,e) 00UTC 16th, b,e,h) 12UTC 16th, c,f,i) 00UTC 17th. Top panel shows shear production at 500 hPa (coloured contours). Middle panel shows potential temperature at 500 hPa (coloured contours). Bottom panel shows 12 hour precipitation accumulation, centred on time step. All panels show SST (black contour lines) and mean sea level pressure (grey contour lines). 79
4.14 Ensemble member 9 vertical cross-sections at 00 UTC 17th at a) 58°W and b) 45°W. Relative humidity is shown in filled contours and isentropes are shown in white contour lines. Wind bars are calculated using meridional (v) and vertical (ω) winds. The grey circles mark the fronts at 500 hPa. 'CF' and 'WF' mark the cold and warm fronts and the arrows, their direction of movement. The horizontal line plots show the shear diagnostic at 500 hPa in red and 12-hourly precipitation (mm) in blue. The vertical line plots show the mean shear production (solid red) and mean absolute shear production (dashed red). 80
4.15 Shear production at 500 hPa (coloured contours) and SST (black contour lines) every 2°C between 20°C and 30°C for a,b) forecast (0.4°) and c,d) ERA-Interim (0.75°) at a,c) 12UTC and b,d) 18UTC 15th January 2004. Low pressure centre marked by white dot. 81

4.16 Shear production against mesoscale kinetic energy (MKE) a) 95th percentile and b) median in domain 25-42°N, 85-60°W at 12UTC 15th (blue) and 00UTC 16th (red). 18UTC 15th also shown for forecast (FC) and ERA-Interim (ERA-I) (purple). Met Office control 'MO CNTL' and smooth 'MO SMTH' at 12UTC 15th shown. R squared results just apply to hindcast ensemble (10 members plus 1 control). 82

5.1 a) Difference in SST between positive and negative NAO years. Green line marked 'A' shows the position of the vertical section shown in panel e. SST in c) NAO+ and d) NAO- (21°C isotherm in bold). b) Same as (a) but for surface currents (colour). The contour line indicates where the time mean current equals 0.5 m/s. e) Same as (a) but for potential temperature at 72.5°W (colour). Black contours indicate the mean potential temperature (ci = 2K) from Roemmich and Gilson (2009). For (a-d) the NAO years are 2009-10, 2010-11 for NAO- and 2011-12, 2013-14, 2014-15, 2015-16 and 2016-17 for NAO+. For (e) the NAO years are 2009-10, 2010-11 for NAO- and 2011-12, 2013-14 and 2014-15 for NAO+. All data averaged over DJF. 92

5.2 Large scale time mean EKE at 200 hPa for a) positive and b) negative NAO years and c) the difference between positive and negative NAO winters. Calculated from hourly ERA5 data. 93

5.3 Distribution of mesoscale kinetic energy, eq. (4.1), integrated over the upper atmosphere (300-600 hPa) in (a) positive (c) and negative NAO phases and the lower atmosphere (625-925 hPa) in (b) positive (d) and negative NAO phases. The difference between positive and negative NAO winters is displayed in (e) upper atmosphere and (f) lower atmosphere. Stippling indicating statistical significance at the 95% level. The 21 °C SST isotherm is shown in black contours in panels a,b,c,d. At positive saturation, white is shown. The units in all panels are kJm^{-2}. 94

5.4 Distribution of positive buoyancy integrated over the upper atmosphere (300-600 hPa) in (a) positive (c) and negative NAO phases and the lower atmosphere (625-925 hPa) in (b) positive (d) and negative NAO phases. The difference between positive and negative NAO winters is displayed in (e) upper atmosphere and (f) lower atmosphere. Stippling indicating statistical significance at the 95% level. The 21 °C SST isotherm is shown in black contours in panels a,b,c,d. At positive saturation, white is shown. The units in all panels are Wm^{-2}. 95

5.5 Distribution of surface heat flux: sensible ($SSHF$) in (a) positive and (c) negative NAO phases, and latent ($SLHF$) in (b) positive and (d) and negative NAO phases. Fluxes are negative in the upward direction. Difference in NAO positive-NAO negative for (e) sensible heat flux and (f) latent heat flux. The 21 °C SST isotherm is shown in black contours. At positive saturation, white is shown. 96

5.6 Distribution of positive shear production integrated over the upper atmosphere (300-600 hPa) in (a) positive (c) and negative NAO phases and the lower atmosphere (625-925 hPa) in (b) positive (d) and negative NAO phases. The difference between positive and negative NAO winters is displayed in (e) upper atmosphere and (f) lower atmosphere. Stippling indicating statistical significance at the 95% level. The 21 °C SST isotherm is shown in black contours in panels a,b,c,d. At positive saturation, white is shown. The units in all panels are Wm^{-2}. 97

5.7 Frequency (percentage of DJF) of negative PV averaged over the upper atmosphere (300-600 hPa) in (a) positive (c) and negative NAO phases and averaged over the lower atmosphere (625-925 hPa) in (b) positive (d) and negative NAO phases. Difference in frequency of negative PV NAO positive-NAO negative in the (e) upper atmosphere and (f) lower atmosphere. Isentropic PV at 315 θ for (g) NAO positive, (h) NAO negative, (i) NAO positive-NAO negative. The 21 °C SST isotherm is shown in black contours. At positive saturation, white is shown. 98

5.8 Stacked contour plot of a) negative PV frequency as %DJF and b) mean negative PV at 925, 700, 500, 300 hPa. SST isotherms shown in black contour lines. Results shown for NAO+ but similar distribution for NAO- (not shown). 99

5.9 Histogram of negative PV in domain 80-40°W 30-60°N for NAO+. Bin size 0.5, range -20 PVU to 0 PVU. Results shown for NAO+ but similar distribution for NAO- (not shown). Mean negative PV values at each level given in same colour as line. 100

5.10 ERA-Interim: Distribution of positive shear production integrated over the upper atmosphere (300-600 hPa) in (a) positive (c) and negative NAO phases and the lower atmosphere (625-925 hPa) in (b) positive (d) and negative NAO phases. The difference between positive and negative NAO winters is displayed in (e) upper atmosphere and (f) lower atmosphere. The 21 °C SST isotherm is shown in black contours in panels a,b,c,d. At positive saturation, white is shown. The units in all panels are Wm^{-2}. 101
5.11 ERA-Interim: Distribution of positive shear production integrated over the lower atmosphere (625-925 hPa) for years pre-2002 (1° ocean resolution) in (a) positive (c) and negative NAO phases and (e) difference; and years post-2002 (0.5-0.05° ocean resolution) in (b) positive (d) and negative NAO phases and (f) difference. Stippling indicating statistical significance at the 95% level. The 21 °C SST isotherm is shown in black contours. At positive saturation, white is shown. 103
5.12 Monthly analysis of the difference in SST between positive and negative NAO years (colour) and surface currents (black lines). Solid black lines are 0.5 m/s and dashed lines are -0.5 m/s. a) Months preceding NAO positive or negative winter (June-November). The years are 2009, 2010 for NAO- and 2011, 2013, 2014, 2015, 2016 for NAO+. b) Months during NAO positive or negative winter (December-February). The years for December as those listed above, and the years for January and February are 2010, 2011 for NAO- and 2012, 2014, 2015, 2016, 2017 for NAO+. 104
5.13 Mesoscale kinetic energy (MKE) as a percentage of eddy kinetic energy (EKE), integrated over the upper atmosphere (300-600 hPa) in (a) positive (c) and negative NAO phases and the lower atmosphere (625-925 hPa) in (b) positive (d) and negative NAO phases. The difference between percentage contribution of MKE to EKE in positive and negative NAO winters is displayed in (e) upper atmosphere and (f) lower atmosphere. The 21 °C SST isotherm is shown in black contours in panels a,b,c,d. At positive saturation, white is shown. 106

List of tables

1.1 Summary of interpretation of RPC (Eade et al., 2014) 2

2.1 Summary table of the effect of ENSO on tropical cyclones in the west Pacific. * mean values taken from (Zhan et al., 2011). 14

3.1 Details of atmospheric and oceanic datasets used 36
3.2 Interpretation of correlation coefficient (Boddy and Smith, 2009) 37
3.3 Cross-correlations of ACE-JJASO ('domain'), ACE-JJASO ('entire') and count over 57 years (1958-2014). Bold indicates significance at p<0.01. ACE-JJASO ('domain') uses only the 6-hourly points within the specified domain to calculate the ACE of each storm, whereas ACE-JJASO ('entire') uses all 6-hourly time steps for the entire length of the track. 38
3.4 Years in cold, warm and mixed PDO periods, defined using the Pacific Decadal Oscillation Index time series. 44
3.5 Regions used for statistical SST model. These are boxes taken from within the red and purple boxes presented in figure 3.6 54

4.1 Some available ECMWF products in 2017 configuration 67
4.2 Operational forecast resolution. *The operational model in 2004 is used in this analysis. 68
4.3 Low pass filter dimensions for ensemble hindcast, ERA-Interim and operational forecast 72

5.1 Table of differences between ERA-Interim and ERA5 89
5.2 NAO positive and negative winters (DJF) 90
5.3 SST and SIC products used in ERA-Interim 91
5.4 ERA-Interim NAO+ and NAO- winters. *Post-2002. ** Weak signal (both indices <=0.4). Counts of seasons in brackets are those once the seasons with weak signals have been removed. 102

List of abbreviations

ACE	Accumulated Cyclone Energy
AGCM	Atmospheric General Circulation Model
AVHRR	Advanced Very High Resolution Radiometer
*CMIP*5	Coupled Model Intercomparison Project 5
CSI	Conditional Symmetric Instability
DLM	Deep layer mean
ECMWF	European Centre for Medium-Range Weather Forecasts
EDA	Ensemble Data Assimilation
EKE	Eddy Kinetic Energy
ENSO	El Niño Southern Oscillation
*ERSSTv*4	Extended Reconstructed SST version 4
GCM	Global Climate Model
IBTrACS	International Best Track Archive Climate Stewardship
IFS	Integrated Forecast System
IPCC	Intergovernmental Panel on Climate Change
ITCZ	Intertropical Convergence Zone
JFM	January February March
JJASO	June July August September October

JTWC	Joint Typhoon Warning Center
MABL	Marine Atmospheric Boundary Layer
MetUM	Met Office Unified Model
MJO	Madden Julian Oscillation
MKE	Mesoscale Kinetic Energy
MSLP	Mean sea level pressure
NAO	North Atlantic Oscillation
NEMO	Nucleus for European Modelling of the Ocean
NOAA	National Oceanic and Atmospheric Administration
OGCM	Ocean General Circulation Model
OSCAR	Ocean Surface Current Analysis Real-time
OSTIA	Operational Sea Surface Temperature and Sea Ice Analysis
PDI	Power Dissipation Index
PDO	Pacific Decadal Oscillation
PNA	Pacific North American
PV	Potential Vorticity
RPC	Ratio of Predictable Components
SIC	Sea Ice Concentration
SLHF	Surface Latent Heat Flux
SLHF	Surface Sensible Heat Flux
SSHS	Saffir Simpson Hurricane Scale
SST	Sea Surface Temperature
UTC	Universal Time Coordinated
VIT	Vertically Integrated Temperature

WBC	Western Boundary Current
WNP	Western North Pacific

Chapter 1

Introduction

With observational records increasing in length and spatial coverage and dynamic models increasing in complexity and resolution, model simulations of the climate are becoming more realistic on all scales. General circulation models are widely used for climate projections many decades into the future, but are also valuable tools for understanding and predicting weather in the shorter term. In running model simulations, there is a trade-off between the spatial resolution, model complexity and ensemble size or length of simulation (figure 1.1).

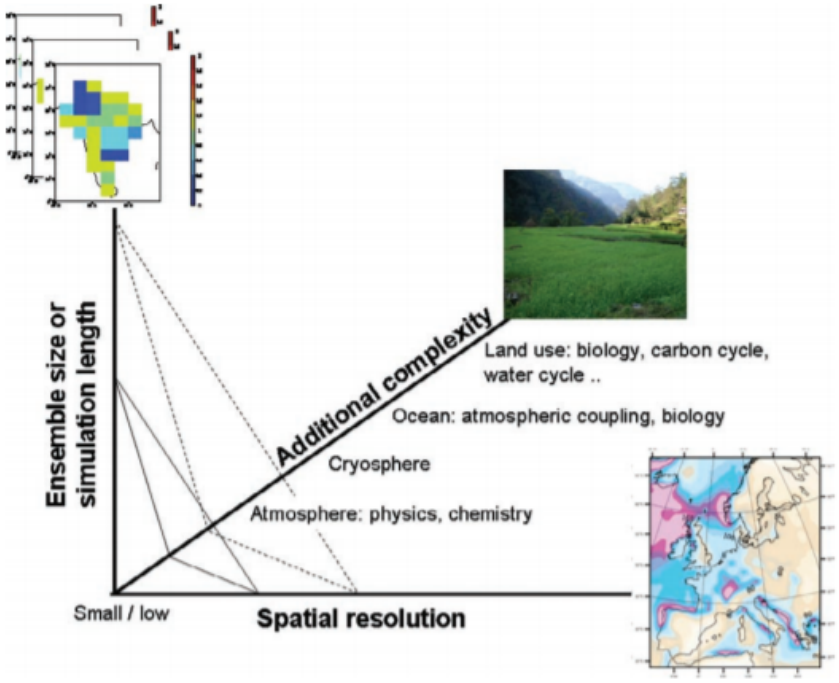


Fig. 1.1 Schematic representation of the trade-offs in climate modelling. Triangles represent surface of approximately constant computer power. Source: Challinor et al. (2009).

Unlike regional models, which assimilate boundary conditions and run over select domains at high resolution, climate models encompass the global circulation, which is necessary for capturing global teleconnections and feedbacks. However, due to this large domain, these models are generally run at coarser resolution. Models can be made more complex by including chemical and biological processes, as well as physical processes. Increasingly, fully dynamic oceans are being coupled to the atmosphere, as it has been shown that the two-way interactions are important on weather as well as climate time scales. The provision of operational quantitative probabilistic forecasts is accomplished by using an ensemble framework, whereby multiple realisations of future projections are created. Using ensemble predictions, it is possible to investigate how well the model spread reflects the real world predictability. Eade et al. (2014) defined a "ratio of predictable components (RPC)" as

$$\mathrm{RPC} = \frac{PC_{obs}}{PC_{mod}} \geq \frac{\mathrm{r}}{\sqrt{\sigma^2_{sig}/\sigma^2_{tot}}} \tag{1.1}$$

where PC is the predictable component and subscripts represent observations (obs), and model (mod). PC_{obs} can be estimated from the correlation (r) between the observations and ensemble mean of hindcasts. PC_{mod} can be estimated from the variance of a large (but finite) ensemble mean relative to the variance of individual ensemble members. The signal variance of the models ensemble mean is shown by σ^2_{sig} and the average variance of all members is σ^2_{tot}. In a forecast system that perfectly simulates real world predictability, RPC is equal to one.

Table 1.1 Summary of interpretation of RPC (Eade et al., 2014)

RPC Value	Correlation	Signal-to-noise ratio
<1	Low (does not capture observed variations)	High (overconfident)
>1	High (captures observed variations)	Low (underconfident)

In an over confident ensemble, an RPC smaller than one occurs, as model ensemble members agree with each other more than observations (high signal-to-noise ratio) but do not capture the observed variations (low correlation) (see equation 1.1) (table 1.1). Such a situation is observed in the equatorial Pacific, where El Niño predictions lack spread or contain systematic errors (figure 1.2).

An RPC greater than one suggests that the real world is more predictable than models, with a high proportion of noise (low signal-to-noise ratio) and an ensemble mean agreeing

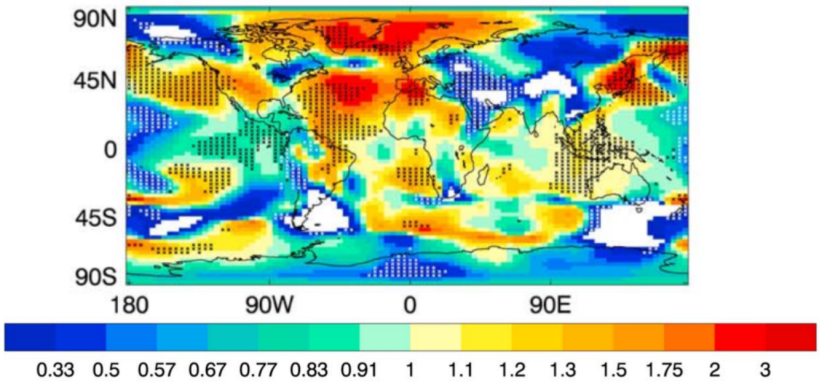


Fig. 1.2 The ratio of predictable components (RPC) for seasonal hindcasts of December-January-February (DJF) mean sea level pressure. Stippling identifies where RPC is significantly different to one at the 90% level. Regions of negative correlation are masked out as they imply zero skill. Source: Eade et al. (2014).

relatively well with observations (high correlation). This occurs in regions with known variability including the area associated with the North Atlantic Oscillation (NAO) (figure 1.2) (Baker et al., 2018; Scaife et al., 2014; Scaife and Smith, 2018), where the model may not be constrained strongly enough by the relevant drivers of predictability (Eade et al., 2014). Skilful predictions from the ensemble mean are possible, despite an unrealistically small signal-to-noise ratio (Dunstone et al., 2016; Eade et al., 2014).

The presence of an ocean component is vital for climate predictions, as it can act as a source of memory for the system. However, the importance of the ocean at shorter time scales is also important, with coupling of the operational deterministic forecast at The European Centre for Medium Range Weather Forecasts (ECMWF) recently implemented (June 2018). Numerous studies have shown that the atmosphere forces the ocean in the mid-latitudes (e.g. Frankignoul and Hasselmann, 1977), in contrast to the Tropics, where there is strong forcing of the atmosphere by the ocean. However, more recent studies have shown that the extra-tropical ocean does indeed influence the atmosphere outside of the boundary layer, but that this influence is of modest amplitude compared to internal atmospheric variability (e.g. Kushnir et al., 2002). Oceanic processes are more important to atmospheric variability in the vicinity of the western boundary currents (WBCs) and their associated SST fronts (Lee et al., 2018; Nakamura et al., 2004; Small et al., 2008; Smirnov et al., 2015), with stronger response of the atmosphere in high resolution models that resolve these fronts (Minobe et al., 2008; Smirnov et al., 2015) (e.g. figure 1.3). If the ocean is the driver of predictability, it is possible that in the El Niño region, the model is too constrained by the ocean, and in the NAO region, it is not constrained enough.

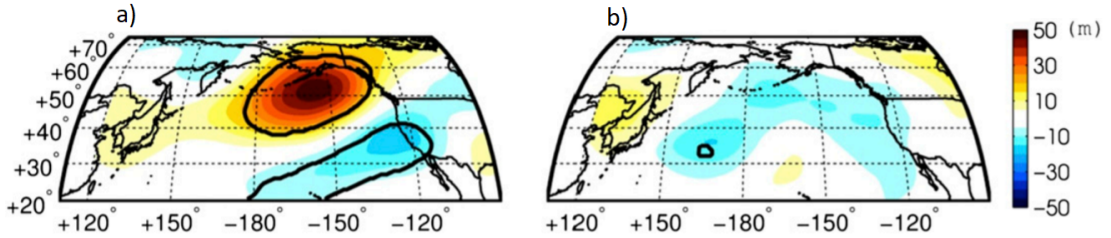


Fig. 1.3 Modelled response to Oyashio Extension shift, with variability in this frontal region projecting onto the larger-scale. The mean December–March difference in 300 hPa geopotential height over the North Pacific for the a) high resolution (0.25°) and b) low resolution (1°) simulations. The black contour denotes areas significant at the 95% confidence level based on a Student's t test. Source: Smirnov et al. (2015).

Not all processes are resolved within a model, and those that are unresolved are routinely parametrised. However, a potential mechanism that may be missing in climate models is shear instability of frontal circulations (Bennetts and Hoskins, 1979), as it is neither resolved nor parametrised. This instability releases slantwise convection, which has been shown to be associated with extra tropical cyclones over the Gulf Stream (Czaja and Blunt, 2011).

1.1 Thesis outline

This thesis uses both observational and modelling tools to examine the predictability of tropical cyclones and the representation of extra-tropical cyclones within the climate system. Small scale instabilities are analysed, to further explore the potential missing process within climate models.

In chapter 2, I discuss the background physics related to tropical and extra-tropical cyclones and their relationship with the ocean and atmosphere. Chapter 3 is the study of seasonal predictability of tropical storms in southern and central China. The dependence of shear instability in an extra-tropical cyclone on spatial resolution, and sensitivity to initial conditions is explored in chapter 4, followed by an investigation into the mesoscale signatures of the North Atlantic Oscillation and interaction with the ocean in chapter 5. Within chapters 3-5 are details of the aims, datasets, results and conclusions. Chapter 6 summarises the conclusions of these studies ends with a perspectives chapter, in which broader research ideas are proposed.

Chapter 2

Background physics

Further details of the background physics relevant to tropical and extra-tropical cyclone activity are now presented. Firstly, the formation and structure (section 2.1) of these systems is detailed, with comparison of necessary conditions for each system. The environmental controls on storm tracks and intensity are then presented (section 2.2), highlighting the importance of both the ocean (section 2.2.1) and the atmosphere (section 2.2.2). The tropical cyclone study (chapter 3) focusses on the west Pacific basin, and section 2.3 provides a more detailed description of the modes of variability affecting tropical cyclones in this region. The studies of extra-tropical cyclones in chapters 4 and 5 examine the North Atlantic region. Important factors affecting their variability in this basin is presented in section 2.4. Even though it is not a focus of this thesis, it is important to recognise the long-term variability of tropical and extra-tropical cyclones, and a brief summary of current research is detailed in section 2.5. Following sections introduce a summary of the progress and limitations of both the observational record (section 2.6) and representation of these cyclones in GCMs (section 2.7). The final section of this chapter (section 2.8) outlines key atmospheric forces in cyclones, ending with symmetric instability, which is discussed in detail in chapters 4 and 5.

2.1 Formation and structure

A tropical storm is a low pressure system that forms over tropical or sub-tropical waters (i.e. 30°N to 30°S), with organised convection and winds at low levels circulating anti-clockwise in the northern hemisphere or clockwise in the southern hemisphere. There are a number of environmental factors that need to be satisfied in order for a tropical storm to generate at a location. These are:

- Presence of a convective system

- Non-negligible Coriolis force (at least 5° from the equator) (Emanuel, 2003)
- Low wind shear (less than 12.5-15 ms^{-1} between 200 and 850 hPa) (Zehr, 1992)
- Sufficient humidity in the mid-troposphere
- Warm ocean water of at least 26.5°C throughout a sufficient depth (50m)

Tropical cyclones cannot be generated spontaneously. To develop, they require a weakly organised system with sizeable spin and low level inflow. A Coriolis force is required for gradient wind balance to occur (section 2.8.2), without which the low pressure of the disturbance cannot be maintained. Therefore, tropical cyclones seldom form equator-ward of 5° latitude (Emanuel, 2003). Large values of vertical wind shear disrupt the incipient tropical cyclone and can prevent genesis, therefore minimal wind shear is important. Relatively moist layers near the mid-troposphere (5 km, 3 miles) are important as well as a warm ocean surface to act as a source of energy. Tropical cyclones are hugely variable in terms of size, for example tropical cyclone Tracy (1974) covered less than 0.03% the area of Super Typhoon Tip (1979), with radius of gale force winds extending more than twenty times further in Tip (Dunnavan and Diercks, 1980; Merrill, 1984). Tropical cyclones tend to extend throughout the depth of the troposphere, to approximately 16 km. The Saffir-Simpson Hurricane Scale (Simpson and Saffir, 1974) is often used to categorise tropical storms by intensity based on maximum winds. Storms with winds of 17 ms^{-1} (33 knots) or less are called 'tropical depressions' and above this they are called 'tropical storms'. With increasing intensity there are category 1 to 5 'hurricanes', with categories 3, 4, 5 referred to as 'major hurricanes'. In the west Pacific basin, if maximum sustained winds reach 33 ms^{-1} (64 knots) the term 'typhoon' is used, and a 'Super Typhoon' is if the maximum sustained winds are at least 67 ms^{-1} (150 knots). The speed they move along the underlying surface, or 'translation speed' is in the range of 2-10 ms^{-1} (Emanuel, 2003).

Figure 2.1 shows the axisymmetric structure of a tropical cyclone and the frontal structure of an extra-tropical cyclone. The tropical cyclone has a warm core, with low pressure at the surface and high pressure aloft. On the other hand, an extra-tropical cyclone is a cold core cyclone, with a slanted vertical profile and low pressure throughout the depth of its core. The main parts of a tropical cyclone are the dense cirrus overcast, rain bands, eye, and the eyewall. Within a tropical cyclone, there are two distinct circulations referred to as 'primary' and 'secondary'. The primary circulation is what visibly characterises the phenomenon, with winds swirling cyclonically around the cyclone eye. The secondary circulation is the flow of air into the centre, ascending in the eye and then diverging at upper levels (see section 2.8.2).

Extra-tropical cyclones are a dominant feature of the mid-latitudes, associated with strong winds, precipitation and temperature changes. An extra-tropical cyclone is a low pressure

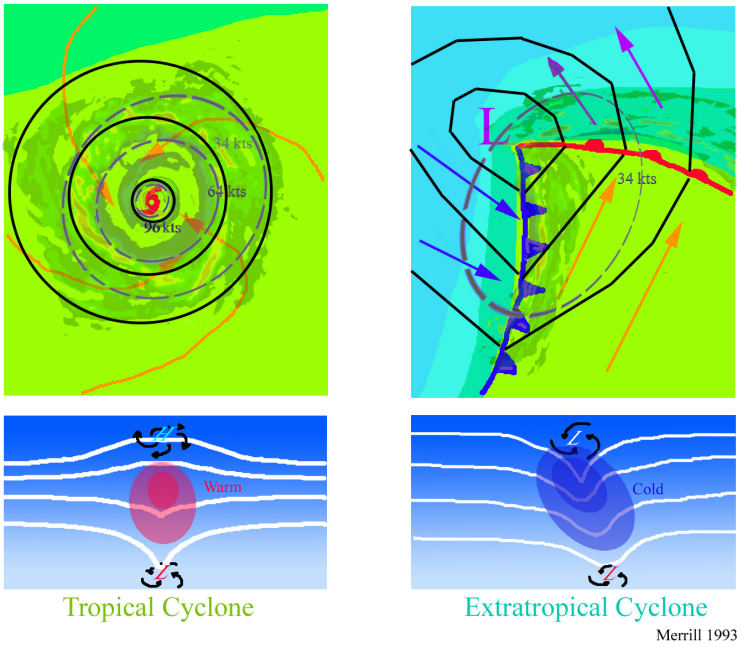


Fig. 2.1 Comparison of a tropical cyclone and an extra-tropical cyclone. The top schematics show horizontal maps of the surface temperature, pressure, and wind fields associated with a tropical cyclone (left) and an extra-tropical cyclone (right). Colours indicate temperature (blue 15°C, blue green 20°C, green 25°C). Dashed lines indicate surface wind speeds. Solid lines are isobars. The bottom schematics show vertical maps of the pressure surfaces, temperature anomalies, and circulation at the surface and tropopause. Source: Merrill (1993)

system that is a result of baroclinic instability, which is a product of horizontal temperature gradients in a rotating environment. This is in contrast to tropical cyclones, where there is little temperature contrast across them and they harness energy from the underlying ocean. Above (near the tropopause) and parallel to this baroclinic zone is often a strong jet stream, balanced by the thermal wind effect (see section 2.8.1 later in the chapter). Unlike the simple symmetric vortices seen in the tropics, extra-tropical cyclones have frontal features, i.e. they are associated with cold fronts, warm fronts, and occluded fronts. In the northern hemisphere their winds rotate counter clockwise, travelling eastward embedded in mid-latitude westerlies. Like tropical cyclones, they transport heat and moisture from the Tropics towards the poles. The following conditions favour **rapid** cyclogenesis (Stull, 2011):

- Strong baroclinicity
- Weak static stability
- Mid- or high-latitude location

- Large moisture input
- Large-amplitude wave in the jet stream

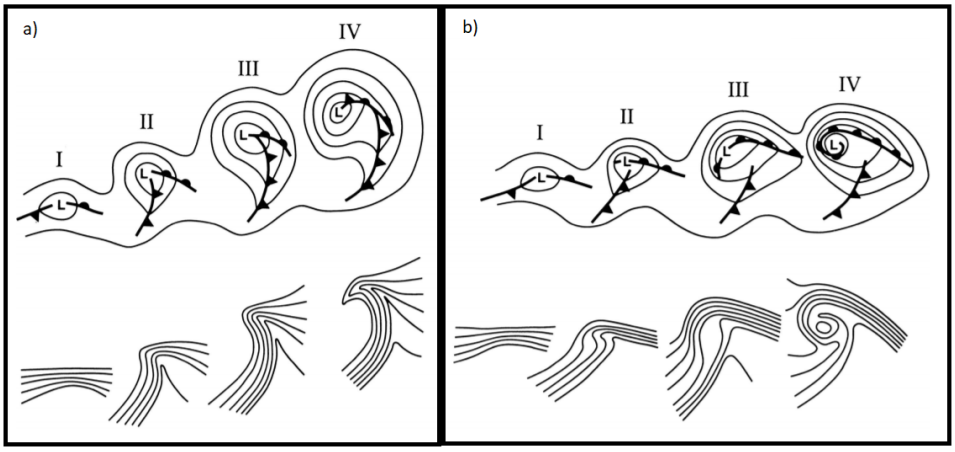


Fig. 2.2 Conceptual models of cyclone evolution showing lower-tropospheric (e.g. 850 hPa) geopotential height and fronts (top), and lower-tropospheric potential temperature (bottom). (a) Norwegian cyclone model: (I) incipient frontal cyclone, (II) and (III) narrowing warm sector, (IV) occlusion; (b) Shapiro–Keyser cyclone model: (I) incipient frontal cyclone, (II) frontal fracture, (III) frontal T-bone and bent-back front, (IV) frontal T-bone and warm seclusion. The stages in the respective cyclone evolutions are separated by approximately 6–24 h. Source: Schultz et al. (1998)

The first conceptualised model of the typical life-cycle of mid-latitude cyclones is the Norwegian model (e.g. Bjerknes, 1922). This was proposed in the 1910s and 1920s and describes the evolution of a cyclone (figure 2.2a). A wave develops on the front as an upper level low pressure system embedded in the jet stream moves over the front. As the air masses begin to rotate, defined cold and warm fronts develop. The wave intensifies and the low pressure centre deepens. The warm sector narrows as the cold front rotates around the cyclone faster than the warm front, and an occluded front develops where the cold front overtakes the warm front. As the cold front continues advancing on the warm front, the occlusion increases and eventually cuts off the supply of warm moist air, causing the low pressure system to gradually dissipate. An alternative model to the Norwegian model, is the Shapiro-Keyser model (Keyser and Shapiro, 1990) (figure 2.2b). The main difference from the Norwegian model is that the cold front moves roughly perpendicular to the warm front and they never meet. The occluded front occurs as a weakness in the cold front near the low pressure centre. An extra-tropical cyclone is typically larger than an average tropical storm (>1000 km compared to 100s of km).

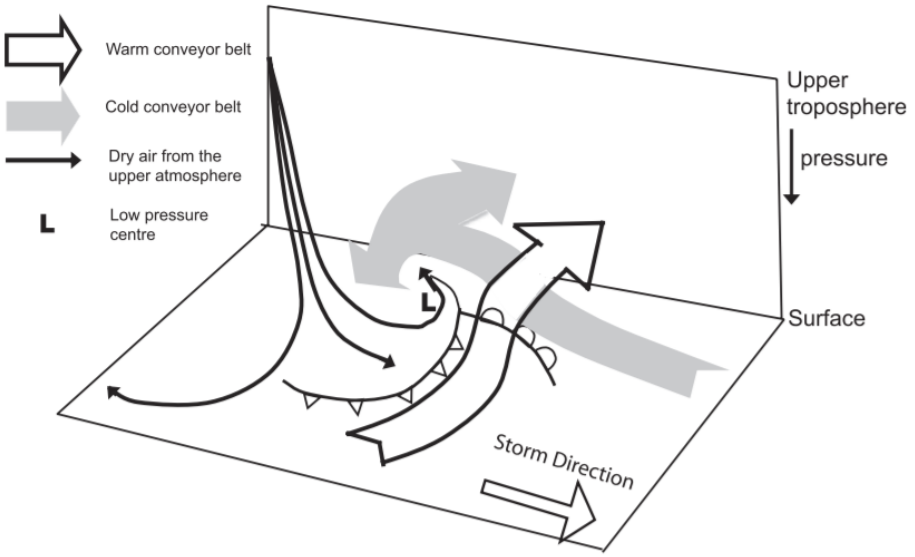


Fig. 2.3 Schematic showing the warm conveyor belt, cold conveyor belt and dry intrusion. Source: Catto et al. (2010)

The conveyor-belt model describes three air streams in the cyclone: the dry intrusion, the warm conveyor belt and the cold conveyor belt (figure 2.3). The warm conveyor belt is a stream of warm, moist air parallel to the cold front. In many extra-tropical regions, the moisture supply is related to anomalously strong surface evaporation, enforced by low relative humidity and high winds over the ocean (Pfahl et al., 2014). The warm conveyor belt is forced to rise rapidly along the moist isentropes as it reaches the surface warm front (Catto et al., 2010), and so is characterised by intense latent heat release and precipitation formation (Pfahl et al., 2014). This atmospheric flow can generate potential vorticity (PV) anomalies in both the lower and upper troposphere due to this latent heat release. Potential vorticity (PV) is the absolute circulation of an air parcel that is enclosed between two isentropic surfaces and is the product of absolute vorticity on an isentropic surface and static stability, and so has a dynamical and a thermodynamical element.

$$PV = -g(\zeta + f)\frac{\delta\Theta}{\delta p} \tag{2.1}$$

where g is gravitational acceleration, ζ is relative isentropic vorticity, f is the Coriolis parameter, Θ is potential temperature and p is pressure.

The latent heat release during this ascent generates positive low-level PV tendencies below the maximum diabatic heating and negative PV tendencies in the warm conveyor belt outflow region (Joos and Wernli, 2012; Madonna et al., 2014; Wernli and Davies, 1997). The cold conveyor belt runs parallel to the warm front and can turn cyclonically or anticyclonically

at low levels, producing a jet (Schultz, 2001). Behind the cold front, which is steeper than the warm front, there is a region of cold, dry air descending.

The Eady model (Eady, 1949) provides a theoretical view of cyclogenesis as part of a horizontal wave, in which the most unstable mode has wavenumber 7-8 (Hoskins and Revell, 1981). The growth of baroclinic eddies in this model acts to reduce the available potential energy, thus reduce the meridional temperature gradient by transporting heat polewards. The Eady growth rate is a useful measure of the climatological baroclinicity at a particular location, peaking in the two storm track entrances in the northern hemisphere. The basic mechanism and the predictions about spatial scale, growth rate and structure are well anticipated by Eady's model.

2.2 Storm tracks and intensity

Natural climate variability of the ocean and atmosphere strongly modulate the seasonal statistics of tropical and extra-tropical cyclones, affecting their distribution across the globe as well as their intensity.

2.2.1 Influence of the ocean

Variations in the ocean surface affect the overlying cyclone, with ocean-atmosphere exchanges of heat, moisture and momentum. The ocean provides a source of energy to the tropical cyclone system by air-sea sensible and latent heat fluxes, determined by the sea surface temperature (SST). Many studies have shown that the SST must exceed 26°C for tropical cyclones to form (e.g. Palmen, 1948). However, there is much research into this threshold (e.g. Dare and McBride, 2011; McTaggart-Cowan et al., 2015), highlighting basin-dependence and the importance of the ocean temperature below the sea surface. The potential intensity of a tropical cyclone is directly related to the SST below the cyclone, all else being equal (Emanuel, 1991; Holland, 1997), with higher SST promoting increased intensity. At high wind speeds, the surface wind stress generates strong turbulent mixing within the ocean. This causes entrainment of cooler water towards the surface from the thermocline, and deepens the mixed layer. The cooling of the SST is determined by the initial state of ocean, storm intensity, translation speed and storm size, and limits storm intensification, especially for slow moving storms, where this cooling effect is large (Bender and Ginis, 2000; Bender et al., 1993). During the lifetime of a storm, the wake produced can change considerably, for example typhoon Megi (2010) created a wake of 1.6°C whilst in the Philippine Sea, but once in the South China Sea, cooling increased to 7°C (D'Asaro et al., 2014). Due to this turbulent

entrainment of cold water into the oceanic mixed layer induced by the tropical cyclone, the state of ocean below the surface is also important to the cyclone system (Bender and Ginis, 2000; Shay et al., 2000). The ocean heat content (OHC) in Joules (J) is a measure of the heat content within the ocean between two reference levels:

$$OHC = c_p \int_{z1}^{z0} (T - T_{ref}) \rho dz \tag{2.2}$$

where c_p is the specific heat of sea water and ρ is density.

Tropical cyclone heat potential (TCHP) is vertically integrated heat content from the sea surface down to the 26°C isotherm, which as at depth 'D26'. If the ocean warm layer (D26) is relatively shallow, (e.g. 60 m) a positive SST anomaly is critical to intensification because the features can effectively deepen the warm layer and restrict the tropical-cyclone induced cooling. If this layer is deep, e.g.>105 m, a warm feature is not required as the background is already sufficient to overcome the negative cooling feedback (Lin et al., 2008). In the western North Pacific, intensification to category 5 requires an SST of around 29°C and subsurface heat content required depends on the storm translation speed (Lin et al., 2009). A shallow warm subsurface (D26 ~60 m) is sufficient to intensify to a category 5 in a fast moving storm, but for slow moving storms, a much deeper warm layer is required (Lin et al., 2009). In the North Atlantic, the record high ocean heat in 2017 due to anthropogenic warming increased the energy for Hurricane Harvey to intensify and also exacerbated the heavy rains and flooding due to the the huge amount of heat removed from the ocean (Trenberth et al., 2018). This highlights the coupled nature of ocean heat content and rainfall within tropical cyclones.

The SST can directly affect the local atmospheric winds through the 'pressure adjustment mechanism' (Lindzen and Nigam, 1987) and the 'vertical mixing mechanism' (Hayes et al., 1989; Wallace et al., 1989). In the former mechanism, SST gradients generate sea level pressure anomalies and the resultant SST-induced sea level pressure drives the surface flow to accelerate toward warmer water. In the vertical mixing mechanism, a warm SST anomaly acts to reduce the static stability of the near-surface atmosphere, causing intensified turbulent mixing that brings down fast-moving air from aloft and accelerates the surface wind (Xie, 2004). Wind speed perturbations are therefore positively correlated and very nearly collocated spatially with SST perturbations, and wind direction perturbations are displaced meridionally from the SST perturbations, with cyclonic flow poleward of warm SST and anticyclonic flow poleward of cool SST (O'Neill et al., 2010).

The mid-latitude storm tracks are defined as maximums in the winter atmospheric variability on a synoptic time scale of 2-6 days (Blackmon, 1976; Hoskins and Valdes, 1990; Lau and Wallace, 1979). Major extra tropical cyclone storm tracks are organised along or

just downstream of the main oceanic frontal zones, for example the Gulf Stream, (Nakamura et al., 2004), where atmosphere-ocean interactions are their strongest. As these synoptic systems cross over the oceanic fronts, from cold to warm water, there is potential for strong heat fluxes into the atmosphere and for convective instabilities to form. In the Tropics, the ocean forces the atmosphere (Visbeck et al., 2003), but in the mid-latitudes, the atmosphere generally forces the ocean (Frankignoul and Hasselmann, 1977). However, oceanic processes can be important to atmospheric variability in the vicinity of the western boundary currents (WBCs) and their associated SST fronts (Lee et al., 2018; Nakamura et al., 2004; Sheldon et al., 2017; Small et al., 2008; Smirnov et al., 2015; Vannière et al., 2017a), with stronger response of the atmosphere in high resolution models that resolve these fronts (Minobe et al., 2008). The effect of ocean fronts is not limited to the boundary layer, but is also apparent in model simulations of the free troposphere (Small et al., 2014). The SST beneath the storm as well as the SST gradient is important in local forcing of the storm, with response to these perturbations driven by latent heat release in the storm warm conveyor belt (Booth et al., 2012).

2.2.2 Influence of atmospheric environmental conditions

A cyclone exists throughout the depth of the troposphere and so the atmospheric conditions have a large effect on the phenomenon. A tropical cyclone is approximately 500-1000 km wide and 10-16 km high, set in much larger scale flow, so it can be treated as a "solid object floating in the atmosphere" (Chan, 2005). Environmental steering is typically defined as the wind within an annulus centred on the tropical cyclone, e.g. 5-7 degrees (Chan, 1985; Chan and Gray, 1982) or 3 degrees (Franklin 1996). To define the steering flow, tropospheric layer means are better than single-level analyses (Velden and Leslie, 1991), with the deep layer mean (DLM, 1000-100 hPa) or mid-tropospheric level (500-700 hPa) often used, the latter found to have the best correlation with direction and speed (Chan and Gray, 1982). The vector quantity for the difference between the environmental steering and tropical cyclone motion is termed ‘propagation’ (Carr III and Elsberry, 1990). This difference arises from variations in the Coriolis parameter and environmental vorticity across the tropical cyclone. Studies have shown that depth of the steering layer is related to the strength of the cyclone (Velden and Leslie, 1991). For a more intense storm, there is greater vertical development of the cyclonic vortex, which is then advected by an environmental flow of greater depth. If the passage of the storm is too slow, the cooling induced by the storm will inhibit intensification, and if it is moving too fast, the resulting asymmetric structure will also inhibit intensification (Zeng et al., 2007). Tropical cyclone translation after landfall is affected by terrain, circulation environment, steering flow, cyclone intensity and structure among others (Xiao-qin and

Bing-ke, 2013). Although wind is the primary atmospheric control on tropical cyclone activity, relative humidity and vorticity are also important. As already mentioned earlier in this chapter, it has been established that vertical wind shear is detrimental to tropical cyclone genesis and intensification (e.g. Chan and Gray, 1982; McBride, 1995), although mature, large tropical storms may resist relatively large wind shear (Zeng et al., 2007).

In the case of extra-tropical cyclones, a baroclinic atmosphere is required for cyclogenesis and there is often an associated strong jet stream running parallel at upper levels. Genesis occurs typically along the polar front, marking the separation between warm subtropical air and cold polar air. Jet streams are important source regions for storm development, with cyclones developing in the jet entrance, being advected downstream and then decaying in the jet exit region (Holton and Hakim, 2012), thus influencing their speed and direction of travel. In the tropics, easterly winds dominate, and in the extra-tropics westerly winds dominate, both steering the movement of these synoptic storms. The environmental conditions that a cyclone moves into affect its structure, impacting development into either a Norwegian model or Shapiro-Keyser model storm (Schultz et al., 1998).

Eddy mean flow interaction describes the process by which large-scale flow anomalies organise the structure of the eddy forcing that excited these anomalies in the first place in a way to reinforce and maintain themselves (Hoskins et al., 1983; Kidston et al., 2010; Nakamura and Wallace, 1990). There is a role of synoptic eddies in the generation of the low-frequency variability of the extra-tropical atmospheric circulation on scales of more than 1000 km, much larger than those scales investigated in this thesis.

2.3 Tropical cyclone variability in the West Pacific

Globally, there are approximately 80-100 tropical storms each year. The greatest frequency is observed in the western North Pacific (WNP), with an average of 26 per year since 1981 (Zhan et al., 2012). From 1977-2011, China had the highest rate of landfalls globally, averaging 6.4 per year (Fudeyasu et al., 2014). Not only does the west Pacific experience the greatest number of tropical storms and landfalls per year, but also the most intense and largest. Tropical storms can occur throughout the year in the west Pacific, but the most active season is from June to November. The WNP has high SST throughout the year (>28.5°C) (Chan, 2007), relative to the suggested 26.5°C threshold for genesis (sections 2.2.1). Variability in activity is related to the SST pattern, with warm anomalies favouring intensification. Tropical cyclone activity in most ocean basins including the WNP has a strong interannual signal (Landsea, 2000), with variability observed in genesis location, track, intensity, landfall and lifetime.

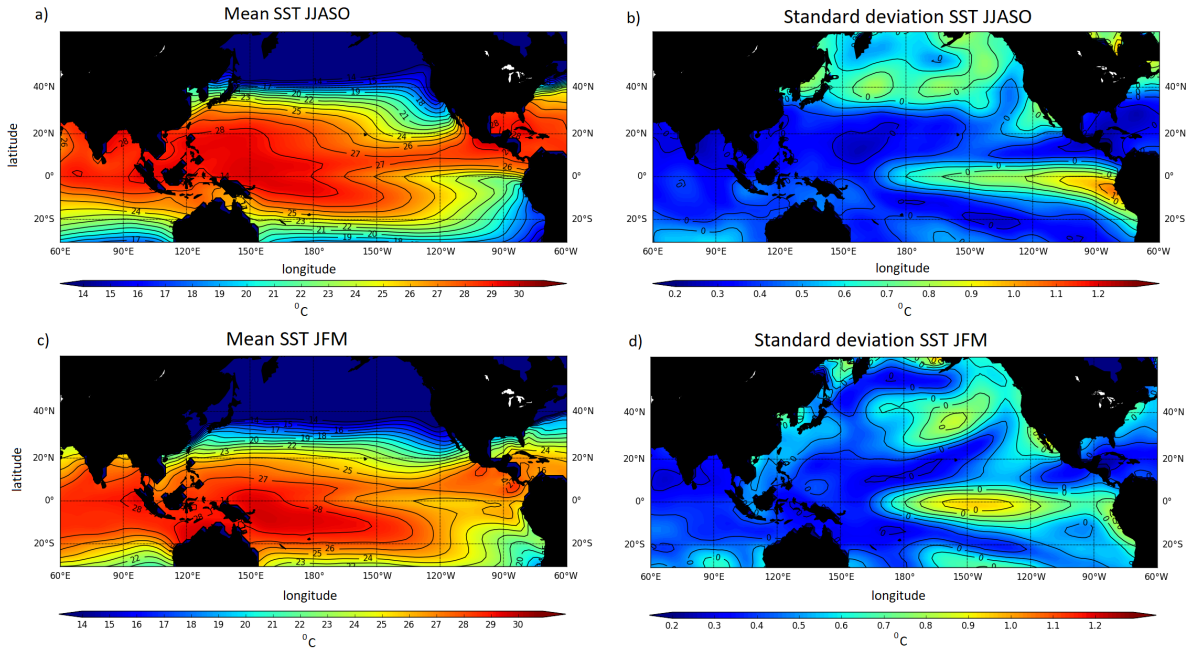


Fig. 2.4 SST climatology 1958-2014. (a) JJASO mean (b) JJASO standard deviation (c) JFM mean (d) JFM standard deviation.

Figure 2.4 shows that during the tropical cyclone season (JJASO), there is a large region of warm SSTs, well above the 26°C proposed threshold for genesis (section 2.2.1). The standard deviation of the SSTs in both JJASO and JFM show the most variation year to year in the equatorial Pacific, where the SST anomalies associated with El Niño and La Niña occur.

It has been long established that the El Niño-Southern Oscillation (ENSO) is the principal driver of interannual variability in the Tropics. This phenomenon also has a marked effect on tropical storm activity in all basins. In a warm El Niño year, when the SST in the central and eastern equatorial Pacific is anomalously warm, there is a zonal displacement of annual mean tropical storm genesis location eastward (Lander, 1994; Zhan et al., 2011). These storms tend to have a longer lifetime and can reach higher intensities before they recurve or meet land (Camargo et al., 2007; Chan, 2007; Chan et al., 1998). In contrast, during La Niña years, the main region of genesis shifts westwards, with fewer intense storms. Although El Niño has been shown to have a significant impact on tropical storm genesis location, the annual storm numbers have been shown to lack an ENSO signal (Lander, 1994). Zhan et al. (2011) found that the total number of tropical cyclones and frequency of weak tropical cyclones were actually correlated with the East Indian Ocean SST.

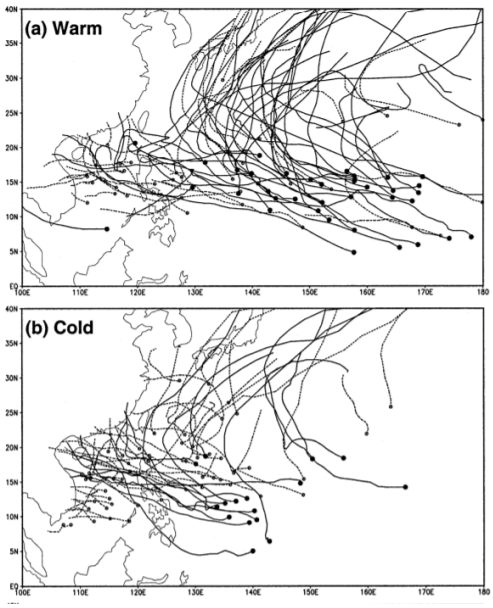


Fig. 2.5 Tropical storm tracks during (a) the six strongest warm (El Niño) years (1965, 1972, 1982, 1987, 1991, and 1997) and (b) the six strongest cold (La Niña) years (1970, 1973, 1975, 1988, 1998, and 1999). Source: Wang and Chan (2002)

Results from Wang and Chan (2002) (figure 2.5) show the tropical cyclone tracks in 6 warmest (i.e. El Niño) and 6 coldest (i.e. La Niña) years, with a clear difference in landfall location between these phases. During El Niño, with more storms generated in the south-east quadrant of the WNP, they tend to recurve before landfall and affect Japan and Korea, with fewer across the Philippines and South China Sea (Liu and Chan, 2008; Wang and Chan, 2002). Whereas in La Niña years, the storms generate further westwards and are straight moving, with increased landfalls observed in China (Camargo et al., 2007; Wang and Chan, 2002).

Table 2.1 Summary table of the effect of ENSO on tropical cyclones in the west Pacific. * mean values taken from (Zhan et al., 2011).

	Genesis	Number of intense storms (annual mean)	Lifetime	Track
El Niño	shifts SE	More (10.2*)	Longer	Recurved
La Niña	shifts W	Fewer (4.2*)	Shorter	Straight-moving

Tropical cyclone activity in the west Pacific also has large variations in the years preceding and following El Niño and La Niña events, with different areas of development and steering patterns (Chan, 2000). After the mature phase of an El Niño, tropical cyclone activity over the

entire ocean basin tends to be below normal, whereas after a La Niña event, the entire basin generally has more tropical cyclones (Chan, 2000). In the year prior to a La Niña event, no significant relationship with tropical cyclones has been found, but there is a relationship with more TCs in September and October over the South China Sea and fewer in the southeast of Japan in the year before an El Niño event (Chan, 2000).

The subtropical high and mid-tropospheric flow pattern are important to tropical cyclone movement (Chan and Gray, 1982). The strength and extent of the subtropical high influence where a tropical cyclone will recurve. The typhoon tracks shown in figure 2.6 have been selected based on their location, either 'Hainan course ' or 'Okinawa course'. The tracks appear largely regulated by the westward extension or the eastward retreat of the North Pacific subtropical high.

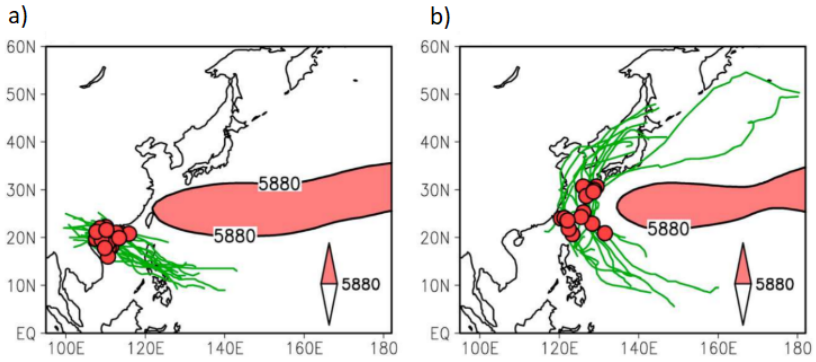


Fig. 2.6 Point of maximum intensity (plotted by circles) and track (lines) of a) Hainan course and b) Okinawa course typhoons. The reference contoured line of 500 hPa geopotential height on day is also exhibited as a background state. The 5880 m line roughly corresponds to the periphery of the North Pacific subtropical high. Source: Hirata and Kawamura (2014)

The Intertropical Convergence Zone (ITCZ) is the area encircling the earth near the equator where the north-east (in northern hemisphere) and south-east (in southern hemisphere) trade winds converge. Where the ITCZ is drawn into and merges with a monsoonal circulation, it is sometimes referred to as a monsoon trough. Most of the tropical cyclones that form in the WNP develop in the monsoon trough (Lander, 1994) and its location exhibits primary control on the distribution of tropical cyclones in the WNP (Wu et al., 2012). The monsoon trough is a climatological feature of low pressure, convergence and increased vorticity, and it exhibits substantial migrations and changes of shape (Lander, 1996). When the monsoon trough is defined as the contiguous region where long-term (1988-2010) mean July-November 850 hPa relative vorticity is positive, 73% of all July-November tropical cyclones form within it (Molinari and Vollaro, 2013). This percentage displays interannual variation correlated with the Niño 3.4 index, with more tropical cyclones forming in the monsoon trough in an El

Niño phase (Molinari and Vollaro, 2013). The shift in genesis with ENSO phase has been related to the eastward extension of the monsoon trough and the reduction in vertical wind shear near the date line (Lander, 1994, 1996; Wang and Chan, 2002).

The Madden-Julian Oscillation (MJO) is a tropical mode of variability that has an intraseasonal time scale (30-90 days). It is characterised by an eastward progression of large regions of both enhanced and suppressed tropical rainfall, observed mainly over the Indian and Pacific Ocean. Over the WNP, tropical cyclone activity appears to be strong when MJO related convection is centred in the WNP (Kim et al., 2008), however, no significant relationship with intensity has been found (Liebmann et al., 1994). As well as affecting the preferable region for genesis, tropical cyclone tracks respond to the large-scale steering flows related to the MJO. When convection is in the equatorial Indian Ocean, tracks migrate eastward, and when over the tropical WNP, they migrate westward (Kim et al., 2008).

The Pacific Decadal Oscillation (PDO) describes variations in North Pacific SST over a decadal (20-30 years) time scale. It is similar to ENSO, with positive and negative SST anomalies, although it is on a much longer time scale and the most pronounced variations are at high latitudes, rather than in the Tropics (figure 2.7). The PDO Index is defined as the leading empirical orthogonal function (EOF) of North Pacific (20–70°N) SST monthly averaged anomalies, defined as departures from the climatological annual cycle after removing the global mean SSTs (Mantua et al., 1997). This north-south dipole of geopotential height over the WNP affects the subtropical high extension and intensity as well as the zonal winds (Liu and Chan, 2008).

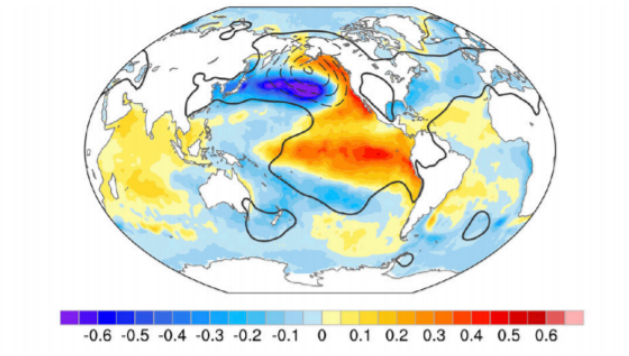


Fig. 2.7 The PDO over the historical record (1901–2014). Regression of global monthly SST (shading) and December-January-February (DJF) sea level pressure (contours) anomalies onto the PDO time series. A positive PDO is associated with negative central North Pacific SST anomaly. Source: Newman et al. (2016)

2.4 Extra-tropical cyclone variability in the North Atlantic

Extra-tropical storms are driven by strong temperature gradients and are at their maximum when surface baroclinicity is strongest, i.e. during winter. In the North Atlantic, they often develop in the baroclinic zone over the Gulf Stream, where strong oceanic fronts help to maintain the strong baroclinicity that is required to maintain them (Hoskins and Valdes, 1990; Nakamura et al., 2008, 2004). In the marine atmospheric boundary layer (MABL), the Gulf Stream directly influences air temperature and pressure fields, but it also has effects throughout the entire troposphere, with upper-tropospheric divergence exhibiting a structure similar to the surface convergence and precipitation patterns, all meandering with the Gulf Stream (Minobe et al., 2008). Many studies have examined air-sea interactions associated with western boundary currents (Cayan, 1992; Czaja and Frankignoul, 2002; Czaja and Marshall, 2001; Kelly et al., 2010; Kwon et al., 2010; Ma et al., 2015; Minobe et al., 2008; Shaman et al., 2010; Smirnov et al., 2015), and it has been shown that the Gulf Stream plays an important role in the climate of the northern hemisphere, mainly through affecting the eddy driven jet and associated extra-tropical cyclones (Booth et al., 2012; Nakamura et al., 2008; Sampe et al., 2010; Small et al., 2014; Vannière et al., 2017a,b; Woollings et al., 2012).

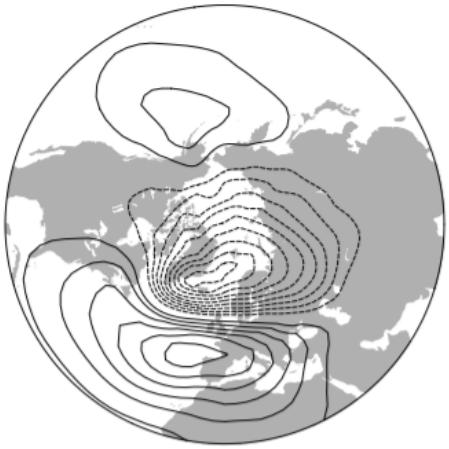


Fig. 2.8 Leading empirical orthogonal functions (EOF 1) of the seasonal mean sea level pressure anomalies (1899-2001) in the North Atlantic sector (20º-70ºN, 90ºW-40ºE). The pattern is obtained by regressing the hemispheric sea level pressure anomalies upon the leading principal component time series. The contour lines are in hPa with an increment of 0.5 hPa, and the zero contour has been excluded. Source: Hurrell et al. (2003)

In the North Atlantic, the leading mode of winter climate variability is the North Atlantic Oscillation (NAO), which is related to SST and storm track activity (Vallis and Gerber, 2008), describing the structure and variability of the North Atlantic eddy-driven jet stream

(Thompson et al., 2003). The NAO is measured by the large-scale change in pressure between the subpolar Icelandic Low and subtropical Azores High (figure 2.8). This pressure difference determines the strength of westerly winds blowing across the North Atlantic, and the negative phase (NAO-) occurs when this pressure difference is small and the positive phase (NAO+) occurs when this is large. The positive phase is associated with a stronger Atlantic jet stream and a northward shift of the storm track, with increased storminess and warmer temperatures over northern Europe associated with the air masses that arrive from lower latitudes, with more frequent occurrence of extreme cyclones due to the presence of a larger area suitable for growth (Pinto et al., 2009). In the negative phase, storms have a much more zonal path and the Icelandic low is weaker, with cold and dry weather over north-west Europe. The persistence of the NAO on intra-seasonal time scales (10–100 days) has been shown to be related eddy mean flow interaction (section 2.2.2), in which there is a positive feedback with eddies, reinforcing the displacement of the jet (Gerber and Vallis, 2007). There are also drivers of the NAO external to the mid-latitude troposphere, including the tropical influence of ENSO and remote stratospheric effects. El Niño events lead to a weakening of the stratospheric polar vortex (SPV), which can then propagate down into the troposphere with a negative NAO response in late winter (Hall et al., 2015). External forcing such as solar variability and tropical volcanic eruptions can also affect the NAO, with a positive NAO response to a solar maximum lagged by a few years (Scaife et al., 2013). A tropical volcanic eruption leads to a cooling of the Earth's surface as the aerosols reflect solar radiation, but a warming of the equatorial lower stratosphere through absorption of terrestrial IR and near-IR solar radiation (Stenchikov et al., 2006). The resultant increased meridional temperature gradient in the stratosphere strengthens the SPV, with a positive NAO anomaly having been observed in winter 2 years after an eruption (Hall et al., 2015). Other causes of NAO variability include cryospheric effects from sea-ice extent and snow cover, where robust relationships are limited, as well as oceanic effects from North Atlantic SST and the Quasi Biennial Oscillation (Hall et al., 2015).

Changes in the wind forcing related to the NAO phase cause significant changes in air–sea heat fluxes and Ekman transport (net motion of fluid due to Coriolis and turbulent drag forces), which induce SST anomalies (Marshall et al., 2001). The leading pattern of SST variability in boreal winter shows a tripole structure, with cold anomalies in the subpolar and subtropical regions, and a warm anomaly in the mid latitudes centred off Cape Hatteras (figure 2.9). There is anomalous cooling in areas associated with enhanced trade winds and westerlies at 50°N. Between these regions, in the western part of the basin there is warming due to a strengthening of subtropical high with southerly flow on its western flank (Wallace et al., 1990). Fluxes at the air-sea interface are proportional to the wind speed, therefore

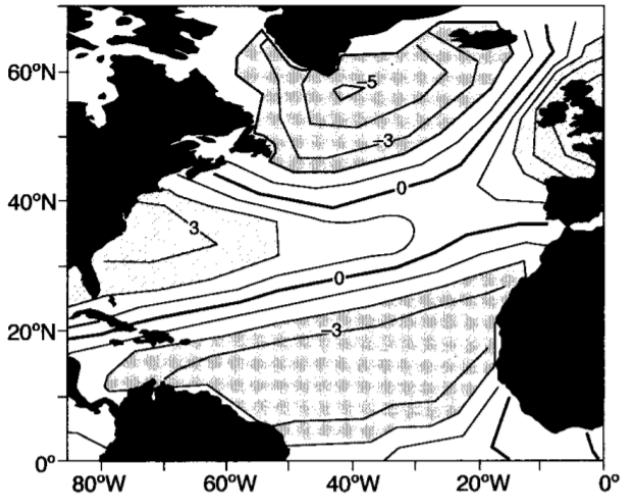


Fig. 2.9 The pattern of SST anomalies that regress onto NAO+, contour interval 1/10 K, negative regions are stippled. Source: Marshall et al. (2001).

patterns of atmospheric circulation that most strongly modulate wind speed are most effective in forcing SST anomalies.

On timescales shorter than the NAO, blocking events are observed. Blocking occurs when the prevailing westerly winds are obstructed by a large-scale stationary system, usually an anticyclone (Woollings, 2011). Shabbar et al. (2001) showed that approximately 30% of the variation in wintertime blocking in the North Atlantic is accounted for by the NAO, with 75% more blocking days in winter NAO- than during NAO+, with on average longer blocking episodes in NAO-.

As well as the interannual variability seen in the NAO and associated SST tripole, there is also a lower frequency mode with a broader pattern of SST variability, investigated by Bjerknes (1964) and revisited by Deser and Blackmon (1993). More recent studies refer to this pattern as the Atlantic Multidecadal Oscillation (AMO) or Atlantic Multidecadal Variability (AMV), and it has a period of 60-80 years. Many model studies have found that the AMO is driven by variability in the oceanic thermohaline circulation, the Atlantic Meridional Overturning Circulation (AMOC) (e.g. Delworth et al., 1993; Knight et al., 2005), with it suggested that salinity is overly important because of cold temperature biases in their relevant convective regions (Ba et al., 2014).

A 20 to 30 year variability is apparent at subpolar latitudes of the North Atlantic in observations (Chylek et al., 2011) and in models (e.g. Gastineau et al., 2018; Menary et al., 2015), and it has been suggested that this decadal variability is caused by large-scale baroclinic instability of the mean flow (Gastineau et al., 2018; Wu and Liu, 2005). The

coupling of the ocean and atmosphere in the North Atlantic region provides a delayed negative feedback as the atmosphere responds to the SST tripole anomaly (Wu and Liu, 2005). This feedback is predominantly associated with the adjustment of the subtropical gyre in response to the anomalous wind stress curl in the subtropical Atlantic. In modelling experiments, atmospheric stochastic forcing can drive SST patterns similar to those in the fully coupled ocean–atmosphere system, but fails to generate any preferred decadal time scales (Wu and Liu, 2005). Removing the impact of the Pacific climate variability can reduce the variance of the North Atlantic decadal fluctuations but cannot disrupt the North Atlantic decadal cycle. Therefore, the North Atlantic decadal variability is a coupled ocean–atmosphere mode local to the Atlantic (Wu and Liu, 2005).

2.5 Long-term variability

Warming of the climate system is unequivocal (Stocker et al., 2013), and as the internal energy available to weather systems such as tropical cyclones changes, activity of these phenomena is also expected to change. Warming of the ocean accounts for 93% of the increase in the Earth's energy between 1971-2010, with 64% of this in the upper ocean (0-700 m) (Rhein et al., 2013).

Modelling studies have consistently projected that greenhouse warming is likely to cause increases in the global average intensity of tropical cyclones and related rainfall rates (e.g. Bender et al., 2010; Elsner et al., 2008; Hill and Lackmann, 2011; Knutson et al., 2010), but some suggest that this is within the range of natural variability. Many studies have shown that with an increase in SST in the coming decades, tropical cyclones will have increasing wind speeds (Bender et al., 2010; Elsner et al., 2008; Emanuel, 2005; Knutson et al., 2010; Murakami et al., 2012; Webster et al., 2005), with Emanuel (2005) suggesting that for every increase in SST of 1°C, peak wind speed would increase by 5%. The assumption is that the dominant effect of increasing carbon dioxide on tropical cyclones is through an increase in tropical mean SST (Zhao et al., 2013). However, modelling studies show that both spatial patterns of SST warming and higher atmospheric carbon dioxide affect tropical cyclones independent of global SST warming.

Pinto et al. (2009) proposed that in the future climate, the total number of North Atlantic cyclones will be reduced by 10% apart from near the British Isles, which will experience an increase in track density and intensity of extreme cyclones due to an intensified jet stream close to Europe. A study of CMIP5 models (Zappa et al., 2013b) found a future increase in cyclone frequency in central Europe and a decrease in the Norwegian and Mediterranean

Seas in boreal winter, with the total number of cyclones decreasing in winter by 24% and summer by 22%.

Alongside SST warming, the effect of global sea level rise has consequences for damage caused by cyclones. Global sea level has risen 10 to 20 cm over last 100 years (Solomon, 2007) and it is very likely that the rate of global mean sea level rise during the 21st century will exceed the rate observed during 1971-2010 (Church et al., 2013), so cyclone-induced storm surge will become an increasingly damaging phenomenon. The water-holding capacity of air is a function of temperature, approximately doubling with each 10°C increase in the range -20 to +45°C (Fowler and Hennessy, 1995). Therefore, in a warmer climate, precipitation from cyclones will be more intense. There is strong evidence that climate change will affect damages from extra tropical and tropical cyclones, with a large variation of projected changes in losses (Ranson et al., 2014). Some uncertainty associated with future projections of both tropical and extra-tropical cyclones derives from the model error in resolving all of the small scale processes, as well as different approaches for identifying and tracking such phenomena (section 2.7).

2.6 Observational record

The historic record of tropical storm activity is longest for the North Atlantic, where records start in 1851 (Landsea et al., 2004). Over the following decades, there has been a significant change in the methodology used to record such storms. In the early period, the main method for identifying tropical cyclones was by records of landfalling storms or from ships at sea (Vecchi and Knutson, 2008). Further back in time, there were fewer ships and shipping lanes as well as fewer people living in the tropical and subtropical coastal regions (Landsea, 2007), therefore it was possible that many storms were unrecorded. Aircraft reconnaissance in the West Pacific began near the end of the second World War and ended in 1987 (Knapp et al., 2013), and since then tropical storms have been monitored primarily by satellite (Lander, 1994). It is well established that although records begin many decades ago for some basins, they are only really trusted since the satellite era, i.e. around the 1970s (Landsea, 2007) when global observations were possible. The observed time series of WNP tropical cyclone activity appears to be affected by artefacts of the changing observing system (Knapp et al., 2013; Lander, 1994), including the increasing use of satellite data and method refinement, e.g. the Dvorak technique.

There are a number of agencies that produce Best Track records of tropical storm activity. The International Best Track Archive Climate Stewardship (IBTrACS) (Knapp et al., 2010) database consists of data from the World Meteorological Organization (WMO) Regional

Specialized Meteorological Centres (RSMC) and Tropical Cyclone Warning Centres (TCWC) (Knapp et al., 2010). In the West Pacific region, data from the following agencies are available:

- Fiji Meteorological Service (as RSMC Nadi)
- Japan Meteorological Agency (JMA) (as RSMC Tokyo)
- China Meteorological Administration's Shanghai Typhoon Institute (CMA/STI)
- Hong Kong Observatory (HKO)
- U.S. Department of Defense Joint Typhoon Warning Center (JTWC)

For the western Pacific region, JTWC storm data are most widely used (Knapp et al., 2010). These other listed agencies provide data for a specific region in the west Pacific, rather than covering the entire basin. In some cases the same storms are tracked by multiple agencies, and large differences in intensity can be found. There are also differences in storm track and lifetime, as agencies employ different procedures for determining the first and last storm track point.

Unlike tropical cyclones, there is no global database of extra-tropical cyclones, which are often referred to as 'European windstorms' in Europe. However, an extreme windstorm catalogue (XWS) has been created for 50 of the most extreme winter extra-tropical cyclones to hit Europe in the period 1979–2012 (Roberts et al., 2014). Since 2017, the UK Met Office and Met Éireann began naming severe winter storms, to allow the approach of the storm to be communicated more uniformly, increasing the awareness of the forecast event. Other countries across Europe also name their storms, but currently there lacks a consistent naming convention across the whole of Europe.

2.7 Representation in GCMs

Current CMIP5 (Coupled Model Intercomparison Project 5) models assessed in the Intergovernmental Panel on Climate Change (IPCC) Fifth Assessment Report (AR5) have horizontal resolution in the atmosphere of around 80 km up to 310 km, and vertical resolution ranging from approximately 20 to 80 levels (Zappa et al., 2013a), an increase from the previous four versions of the report. It is well established that the current generation of global climate models (GCMs) are of insufficient resolution to simulate tropical cyclones in detail due to their low resolution in comparison to the size of the storm core (Lin et al., 2012) and the complex nature of tropical cyclone structure. However, enhanced computing capabilities

and parametrisations have resulted in better representation of tropical cyclones (Bengtsson et al., 2007; Walsh et al., 2007; Zhao et al., 2009). Modern GCMs are capable of producing structures that can be recognised as similar to tropical cyclones at resolutions as coarse as 100 km (Knutson et al. 2010), but without the details of the core (McDonald et al., 2005). There is a need for very high resolution in order to simulate realistic storm intensities, (Bender et al., 2010; Emanuel et al., 2008) for example it has been suggested that 2 km or less is needed to represent important physical processes in the tropical cyclone eyewall (Gentry and Lackmann, 2010), with Chen et al. (2007) suggesting that a resolution of 1 km is required to resolve hurricane eye wall convection and wind maxima. Resolution is important for simulating storm intensity, but less critical for simulating the annual number of tropical cyclones and their geographical distribution. Zhao et al. (2009) found that a model with a resolution in the 20-100 km range was able to simulate the climatology and interannual variability of tropical storm frequency without realistic distribution of storm intensity. Similar results were found by Strachan et al. (2013), with realistic interannual variability of storm occurrence requiring resolutions of 100 km or higher, but skill was basin dependent. Different models produce substantially different annual global tropical cyclone frequencies and geographical distributions due to model resolution and physical parametrisations (Zhao et al., 2013). It has been found that there are larger differences in tropical cyclone distribution between models than in the same model at different resolutions, suggesting a greater influence of model configuration than resolution (Shaevitz et al., 2014). In a regional model with explicit convection (4.4 km grid spacing), Short and Petch (2018) showed much improved predictions for the intensities of strong storms (category 3 and above) and representation of rapid intensification (RI) events, which the global model (UK Met Office Unified Model, 17 km) was unable to resolve. The location of rainfall within intense tropical cyclones as well as the statistical distribution of rain rates is also more skilfully predicted. Although the regional model adds value, notable biases are also identified.

Zappa et al. (2013a) found systematic biases affecting the number and intensity of North Atlantic cyclones in historical CMIP5 simulations (1976–2005) compared to ERA-Interim (1979–2008). In the winter season, the North Atlantic storm track tends to be either too zonal or displaced southward, with too few and weak cyclones over the Norwegian Sea and too many cyclones in central Europe. The intensity of cyclones is generally too weak, but improves with increasing resolution in CMIP5 models (Zappa et al., 2013a) and reanalyses (Rohrer et al., 2018). The sensitivity of key characteristics of extra-tropical cyclones to model resolution has also been shown by Jung et al. (2006), but in some regions, such as the entrance regions of the major northern hemisphere storm tracks, model deficits are insensitive to increases in horizontal resolution. A global coupled model (HiGEM) with atmospheric

resolution of 0.83° x 1.2° and ocean resolution of 1/3° is able to capture the structural features of an extra-tropical cyclone, including the warm conveyor belt, cold conveyor belt and dry intrusion (Catto et al., 2010), however, the characteristics of frontal scale ocean–atmosphere interaction, such as the positive correlation between SST and surface wind stress, are only captured when the ocean component is eddy resolving (1/10°) (Bryan et al., 2010).

2.8 Atmospheric forces in cyclones

This section summarises large-scale balances and smaller scale instabilities that are relevant to the studies in this thesis.

2.8.1 Geostrophic balance

The geostrophic wind is the exact balance between the Coriolis force and the pressure gradient force and is directed parallel to isobars. This condition is called geostrophic balance and in pressure coordinates is:

$$-fu_g = \frac{\partial \phi}{\partial y} \tag{2.3}$$

$$fv_g = \frac{\partial \phi}{\partial x} \tag{2.4}$$

where f is the Coriolis parameter ($2\Omega\sin\theta$, ~$10^{-4}\mathrm{s}^{-1}$ in mid-latitudes), Ω is the rotation rate of the Earth (7.2921×10^{-5} rads^{-1}), θ is latitude in radians, u_g and v_g are geostrophic zonal and meridional winds, and ϕ is geopotential height.

In a baroclinic atmosphere, the geostrophic wind increases with height as a result of the thermal wind relation:

$$f\frac{\partial u_g}{\partial p} = \frac{R}{p}\frac{\partial T}{\partial y} \tag{2.5}$$

$$-f\frac{\partial v_g}{\partial p} = \frac{R}{p}\frac{\partial T}{\partial x} \tag{2.6}$$

where R is the specific gas constant for dry air, p is pressure and T is temperature. The thermal wind is the difference between the geostrophic wind at two vertical levels and therefore represents the vertical wind shear of the geostrophic wind and is directly proportional to the horizontal temperature gradient.

The Rossby number is the ratio of characteristic scales of velocity and Coriolis terms:

$$R_0 = U/fL \tag{2.7}$$

where U is the velocity scale, f is the Coriolis parameter, and L is the horizontal length scale. Flows with sufficiently small (<1) Rossby number are in geostrophic balance. Extra-tropical cyclones are large enough to be significantly influenced by the Earth's rotation, for example L=1000 km, U = 10 ms^{-1}, f = $10^{-4}s^{-1}$, therefore R_0 = 0.1.

2.8.2 Gradient wind balance

The basic horizontal balance in a tropical cyclone above the boundary layer is between the sum of the Coriolis and centrifugal forces, balanced by the horizontal pressure gradient force. This balance is referred to as gradient wind balance (figure 2.10):

$$\frac{v^2}{r} + fv = \frac{1}{\rho}\frac{\partial p}{\partial r} \tag{2.8}$$

The centrifugal force alters the original two-force geostrophic balance and creates a non-geostrophic gradient wind. The classic theory for hurricane intensification relies on the inflow induced by the deep convection. However, as the vortex strengthens, the boundary layer becomes increasingly important (Smith and Montgomery, 2016).

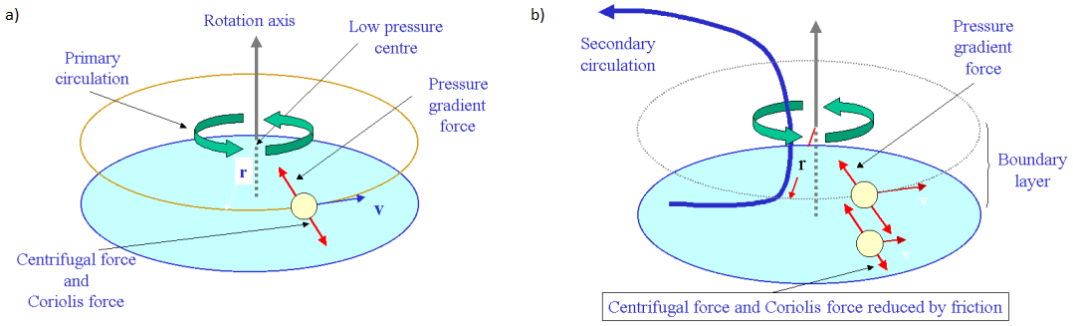


Fig. 2.10 a) Gradient wind balance in the primary circulation of a tropical cyclone b) disruption of gradient wind balance by friction in the boundary layer leaving a net inward pressure gradient that drives the secondary circulation with inflow in the boundary layer and outflow above it. Source: Smith, 2006

Surface friction in the boundary layer reduces the wind speed near the surface and therefore the centrifugal and Coriolis forces, but has little effect on the pressure field. There is therefore a net inward force in the boundary layer, driving inflow and the secondary circulation. Due to the conservation of angular momentum, objects will spin faster as they

move towards the centre of the circulation, and so wind speed increases towards the centre of the tropical cyclone.

2.8.3 Gravitational instability and upright convection

In a hydrostatically balanced atmosphere, the mean-state potential temperature (θ) increases with height. Potential temperature is not affected by vertical movements and associated expansion and compression of an air mass, and is calculated using temperature and pressure:

$$\theta = T\left(\frac{P_0}{P}\right)^{\frac{R}{cp}} \tag{2.9}$$

where P_0 is reference pressure (1000 hPa). R is the gas constant of dry air and cp is the specific heat capacity at a constant pressure, (R/cp=0.286). Equivalent (moist) potential temperature (θe) is conserved during changes to pressure, even in the presence of phase change. It is the temperature a parcel of air would have if all of the water vapour were to condense, releasing latent heat, and the parcel were brought adiabatically to a reference pressure.

If the potential temperature decreases with height, there will be overturning as the cool air sinks. This is gravitational instability, which releases upright convection and is purely vertical.

$$\frac{\partial \theta}{\partial z} < 0 \tag{2.10}$$

In the presence of a disturbance, the acceleration of an air parcel is proportional to the difference in potential temperature between the parcel (subscript p) and the atmospheric environment (subscript env) into which it has been displaced. This was described by Emanuel (1983a) as:

$$\frac{Dw}{Dt} = \frac{g}{\theta e}(\theta e_p - \theta e_{env}) \tag{2.11}$$

where w is vertical velocity and D/Dt is the Lagrangian derivative.

2.8.4 Inertial instability and horizontal movement

Whereas the gravitational instability operates in the vertical, inertial instability operates in the horizontal plane and results from an imbalance of the horizontal pressure gradient and inertial forces (centrifugal and Coriolis).

Inertial instability is detected by absolute momentum (M), which is defined by Eliassen (1962) as the rotation of the Earth plus the rotation due to variations in the wind field:

$$M = V + fx \tag{2.12}$$

where V is the frontal velocity and x is the distance along the transverse plane to the front. When the absolute momentum decreases in the x-direction then the atmosphere is unstable to horizontal motions:

$$\frac{\partial M}{dx} < 0 \tag{2.13}$$

The acceleration of a parcel following a horizontal displacement can be calculated from the difference in the absolute momentum between the parcel and its new environment as shown by Emanuel (1983a):

$$\frac{Du}{Dt} = f(M_p - M_{env}) \tag{2.14}$$

where u is the horizontal wind component in the transverse plane to the front.

The presence of inertial instability over a large area would immediately generate inertially unstable motions, which would mix the fluid laterally, just as upright convection mixes vertically.

2.8.5 Symmetric instability and slantwise convection

Symmetric instability is a combination of gravitational and inertial instability. A parcel may be inertially stable to horizontal displacements and gravitationally stable to vertical displacements, but may be unstable to slantwise displacements by symmetric instability.

A barotropic atmosphere is one where the density depends solely on pressure, whereas in a baroclinic atmosphere the density depends on both the temperature and the pressure. In a barotropic flow, potential temperature surfaces (isentropes) are horizontal and absolute momentum surfaces (M) are vertical. In a baroclinic environment, the isentropes tilt upwards on the cold side and downwards on the warm side. Only moist slantwise instability occurs in the Earth's atmosphere (Bennetts and Hoskins, 1979) and so θe is used. This instability has a 2D assumption that there is no variation in the along front direction, therefore the term 'symmetric' is often used. This instability is often referred to as conditional symmetric instability (CSI) (Schultz and Schumacher, 1999), as it is dependent upon saturation.

The M-θe relationship states that if the θe surfaces are steeper than the M surfaces, there is symmetric instability. Any slantwise displacement occurring between the slopes of

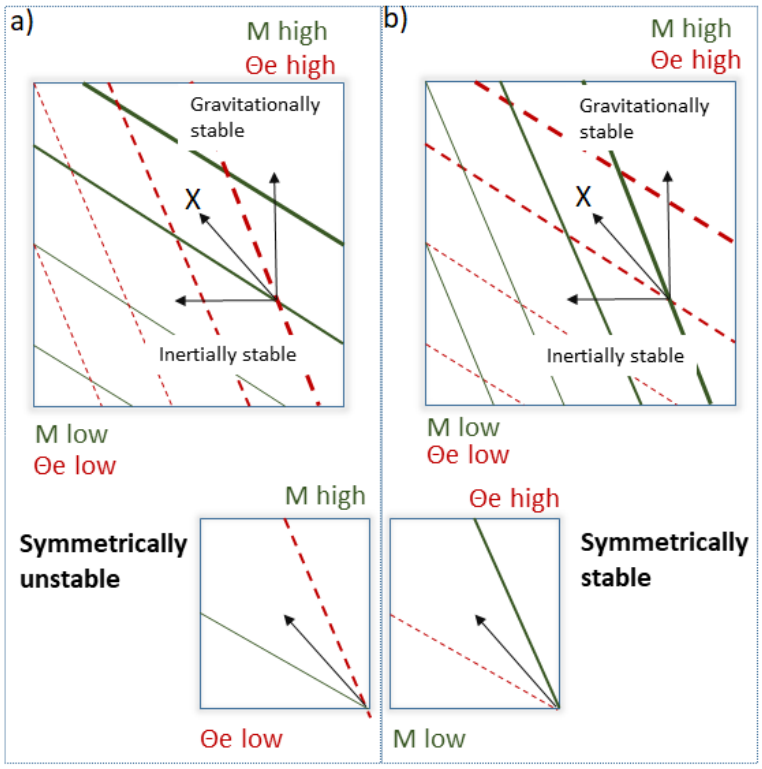


Fig. 2.11 Symmetric instability in relation to isentropes and lines of constant absolute momentum (M). a) Unstable to symmetric instability, b) stable to symmetric instability. Isentropes are shown in red dashed lines and lines of constant absolute momentum (M) in solid green. Thickness of the lines increases towards higher values. Both environments are baroclinic and θe and M are low in the bottom left and high in the top right. The black arrows show direction of movement of air parcels. In both panels a and b, if a parcel is moved to the left, it is inertially stable as it is moving towards an area of reduced absolute momentum. In both panels a and b, if a parcel is moved vertically, it is gravitationally stable as potential temperature is increasing in this direction and so the parcel will return to it's original position. However, in panel a, if an air parcel is moved along arrow X, it is moving towards lower potential temperature and high M, so is symmetrically unstable. In panel b, it will move towards higher θe and low M, and is symmetrically stable. Modified from Morcrette (2004)

these surfaces will release the symmetric instability and the parcel will be accelerated in the direction away from the original position. Figure 2.11 illustrates the M-θe relationship, with a symmetrically unstable atmosphere on the left (a) and a symmetrically stable atmosphere on the right (b). On the right hand side, the absolute momentum surfaces (M surfaces) are steeper than the equivalent potential temperature (θe) surfaces, and so a parcel displaced to point X has a lower equivalent potential temperature and a higher absolute momentum than the environment. From equations 2.14 and 2.11, the parcel will be accelerated back towards its original position. On the left hand side of figure 2.11, the θe surfaces are steeper than the M surfaces, and so a parcel displaced in a slantwise motion will have a higher θe and lower M than the environment. A parcel displaced in this direction will be accelerated in the direction of the displacement, given equations 2.14 and 2.11 until it reaches a point where the parcel temperature and absolute momentum is stable with the environment.

The most unstable mode is composed of parcels ascending and descending isentropic surfaces (Bennetts and Hoskins, 1979), therefore the perturbation potential temperatures and perturbation pressure are zero. Perturbation momentum equations are then:

$$\frac{\partial u'}{\partial t} = fv' \tag{2.15}$$

$$\frac{\partial v'}{\partial t} = -\zeta_\theta u' \tag{2.16}$$

In the meridional direction, where ζ_θ is the projection of the relative vorticity vector onto an isentrope (i.e. proportional to the potential vorticity (PV)).

The kinetic energy of this most unstable mode is:

$$d\left(\frac{\overline{u'^2 + v'^2}}{2}\right)/dt = -\left(\overline{\omega' u'}.\frac{\partial \overline{u}}{\partial p} + \overline{\omega' v'}.\frac{\partial \overline{v}}{\partial p}\right) \tag{2.17}$$

These equations are for an idealised dry, infinite atmosphere, and the instability criterion is a Richardson number <1. The Richardson number (Ri) is the ratio of the squared buoyancy frequency (N^2) and horizontal wind shear ($|\partial U/\partial z|^2$). N^2 is a measure of the static stability of the environment and if positive, the parcel will oscillate about its initial level with frequency N. An unstable case is where N^2 is negative, where potential temperature is decreasing with height. In an environment with a weak N and/or strong vertical shear, the Richardson number is low. In reality, Ri is rarely less than 1 but close to 1 (Czaja and Blunt, 2011). The moisture present in the atmosphere enables this instability to act even when this criterion (Ri<1) is not met. Symmetric instability is by definition two-dimensional, and shear instability is a more general 3D instability. It has been suggested that slantwise convection from the release

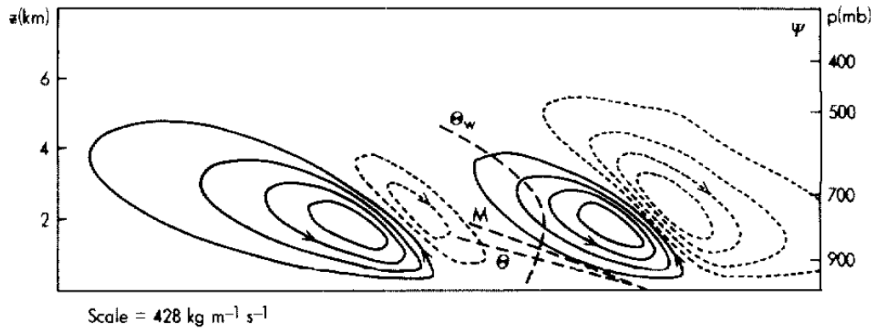


Fig. 2.12 The streamfunctions for the transverse circulation to a front in a simple experiment in an idealised slantwise unstable atmosphere. The initial potential temperature (θ), wet bulb potential temperature (θw) and absolute momentum (M) are also plotted. Source: Bennetts and Hoskins (1979)

of shear instability can explain banded precipitation often seen at cold fronts (Bennetts and Hoskins, 1979; Seltzer et al., 1985), caused by cells of alternating rotation creating updrafts and downdrafts. Shear instability can occur in tropical cyclones (Molinari and Vollaro, 2014) as well as extra-tropical cyclones. This shear production term for kinetic energy (equation 2.17) forms a significant part of the analysis in chapters 4 and 5, in which extra-tropical cyclone activity is investigated.

The slantwise adjustment to slantwise instability is approximately 3 hours (Emanuel, 1983; Reuter and Yau, 1990), compared to less than 0.5 hours expected for upright adjustment. Although upright instability is routinely parametrised in climate models, shear instability is often neglected. Observations have shown that shear instability is apparent in the real atmosphere (Reuter and Yau, 1990) and it has been parametrised with measurable improvement in forecasts (Lindstrom and Nordeng, 1992). This instability can now be resolved in high resolution weather models, but is too small scale a process to be resolved in coarser climate models.

2.9 Conclusion

This chapter has presented the characteristics of tropical and extra-tropical cyclones with details of both oceanic and atmospheric controls on their activity. There are several modes of variability that act on different timescales, from intra-seasonal to decadal, as well as long-term trends due to climate change. It is important to be aware of the limitations of both the observational record and GCMs when analysing both tropical and extra-tropical cyclones.

The following chapter examines the seasonal predictability of tropical cyclones in the west Pacific basin using the historic record and reanalysis data. Extra-tropical cyclone activity in the North Atlantic basin ins explored in chapters 4 and 5, focussing on atmospheric instability which has been introduced in section 2.8.5 and the representation of small scales in GCMs.

Chapter 3

Seasonal predictability of tropical storms in southern and central China

Key findings: A robust relationship between SST ~18 months before the storm season and storm frequency over southern China.

3.1 Introduction

In this chapter, predictability of seasonal storm activity over southern and central China is explored in relation to SST up to ~18 months in advance. Operational seasonal forecasts use empirical relationships, dynamical modelling, or a combination of both, with a lead time of a few months, and largely issue basin-wide forecasts.

3.1.1 Tropical storm forecasting techniques

Rather than forecasting exact cyclone tracks and dates of occurrence, predictions are made for basin-wide activity over a seasonal period. Seasonal predictability of the climate system stems from the slowly evolving lower boundary, e.g. ocean forcing, and the balance between this forcing and the effects of random chaotic weather determine the level of seasonal skill over a region (Rowell, 1998). Seasonal tropical storm predictions are developed using dynamical, statistical, or statistical-dynamical models, with forecasts typically made 3 months ahead, e.g. March for the start of the season in June, with updates in May or June.

Dynamical modelling

For climate model simulations, accurate representation of the ocean is vital, as the ocean represents a dynamic thermal reservoir that exchanges energy with the atmosphere. Fully-coupled atmosphere-ocean models, where heat and transport are fully represented and interactive, provide the best opportunity to capture relationships at a variety of scales. Global models are vital as they can capture teleconnections, however they are run at too coarse a resolution to represent the intensity of tropical cyclones, with model intensity distributions often too narrow and skewed toward the lowest intensities. Even with a high resolution model (16 km), Manganello et al. (2016) found that the intensity distributions are only realistic up to wind speeds corresponding to category 2 storms in the West Pacific with the strongest model tropical cyclone wind speeds equivalent to category 4. If the tropical cyclone intensity is assessed using the lifetime minimum sea level pressure rather than wind speed, there is a much better correspondence to observations, which is likely due to the storms remaining relatively large in size (Roberts et al., 2015). Due to the model bias in intensity, they are often not used directly, and instead are compared to the model climatology, which is then adjusted to cover the full spectrum of intensities. In order to extract the storms, a tracking algorithm needs to be applied to the model output, and the choice of tracking method (e.g. tracking vorticity or minimum pressure) produces different storm activity (Horn et al., 2014).

Seasonal forecasts for western North Pacific (WNP) tropical cyclone activity from dynamical models are produced by the European Centre for Medium-Range Weather Forecasts (ECMWF). They have produced operational seasonal tropical cyclone forecasts for all basins since 2001 with their global coupled model. Predictions include tropical storm frequency, typhoon frequency, track density and accumulated cyclone energy (ACE) (Zhan et al., 2012). The skill of seasonal forecast models is often found to be higher using an ensemble than any single deterministic run (e.g. Vitart, 2006), and ECMWF use this ensemble approach. The Met Office has issued forecasts of tropical storm activity using a fully coupled dynamical model for the North Atlantic basin since 2007, and for the WNP since 2015 (Camp et al., 2015).

Statistical models

It has long been established that large-scale variability affects tropical cyclone activity globally. If a robust relationship between large-scale predictors and this activity can be found, it is possible to make predictions about future activity using statistical analysis. The first region over which a statistical forecast for tropical cyclone activity was produced was the

Australian region, in the late 1970s and 1980s (Nicholls, 1979, 1985), with forecasts for the North Atlantic starting in 1984 (Gray, 1984).

The first operational tropical cyclone forecasts for the WNP were issued by the National Climate Center (NCC) or CMA (China Meteorological Agency) in 1994 but these were only available in China (Zhan et al., 2012). NCC currently issue seasonal forecasts of WNP tropical cyclone activity in March, with updates in June. The predictors used are El Niño Southern Oscillation (ENSO) index, 500 hPa geopotential height over the Pacific and Australian region, convective activity over the WNP, vertical wind shear of zonal wind over the WNP and tropical eastern Pacific prior to the season (Zhan et al., 2012).

In 1997, The City University of Hong Kong (CUHK) started to issue seasonal forecasts to the public. This scheme used SST anomalies as a proxy for ENSO signal, the large-scale circulation over Asia and the western Pacific, and trend or climatology and persistence (Chan et al., 1998). New predictors related to ENSO including changes to the Southern Oscillation, Australian monsoon and subtropical high in the South Pacific have since been identified (CL Chan et al., 2001). Previous work by Lu et al. (2013) examined the seasonal predictability of tropical cyclones affecting Taiwan using an empirical model. They found some skill in predicting accumulated cyclone energy (ACE) during June-September using the SST in three regions and the sea level pressure (SLP) over an area in East Asia as predictors.

A principal limitation of such statistical forecasts is the dependence on historic observed data, which are relatively limited (~50 years) and have associated biases and errors (section 2.6). A statistical model assumes stationarity of relationships and is unable to be used for climate change projections. Alongside statistical and dynamical approaches, hybrid statistical-dynamical approaches have increased in popularity in recent years.

Hybrid dynamical-statistical models

These models are a combination of the dynamical and statistical modelling approaches. A statistical model is developed based on either observations or output from a climate model, and then this is applied to the seasonal prediction using predictors from a dynamical model. Skill of this model depends on robustness of the statistical relationship as well as the skill of the model to predict the predictor. Zhan and Wang (2016) showed that a hybrid dynamical-statistical model showed better skill at longer lead times that the pure statistical model at predicting seasonal accumulated cyclone energy (ACE).

3.2 Research question

Most seasonal projections of tropical cyclone activity are basin-wide, without any indication of landfall area and therefore risk to the population. Here, I explore the predictability of tropical cyclone activity over a specific region, which is more relevant in terms of preparing communities at risk. A study by Lu et al. (2013) showed predictive skill for typhoon activity in a domain around Taiwan, and I am using the same empirical approach to explore the relationship with tropical cyclone activity in a domain encompassing parts of southern and central China. Whereas Lu et al. (2013) used predictors from March-May before the storm season, I aim to identify whether there exist any relationships during the previous year (up to 18 months beforehand). At these long time scales, the ocean can provide a source of predictability, as the time scales of changes in the ocean are much slower than in the atmosphere. Over an annual cycle, signals can be hidden beneath the mixed layer and re-emerge months later (e.g. Alexander et al., 1999). Therefore, focussing on ocean variables as predictors, this study will explore the relationship between the ocean and tropical cyclone activity over this extended time scale.

3.2.1 Aims

- To explore the seasonal predictability of tropical storms in southern and central China
- Examine SST correlations in the year prior to the storm season

3.3 Methods

3.3.1 Tropical storm data

The Joint Typhoon Warning Center (JTWC) Best Track dataset provides the tropical storm data and was obtained from the IBTrACS database (Knapp et al., 2010). Any storms in the west Pacific that have a start time during the months of June to October and have a maximum intensity of at least 17 ms^{-1} (34 knots) are selected. The dataset includes the position, maximum sustained winds and minimum central pressure for every tropical cyclone globally at 6-hr intervals in UTC.

All of the storms that intersect a domain encompassing parts of southern and central China (figure 3.1) from 1958-2014 were chosen for further analysis. This region was motivated by Met Office funding and the relatively high probability of a tropical cyclone passing over this region (from 1945-2012 observations, http://moe.met.fsu.edu/tcprob). This period

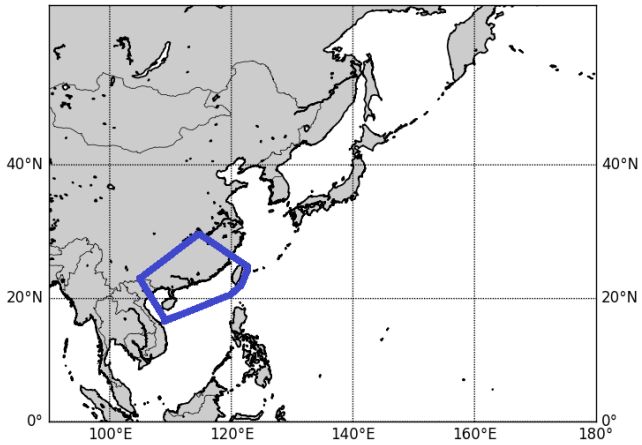


Fig. 3.1 Blue polygon highlights the domain used for this analysis, encompassing parts of southern and central China.

examined in this study includes data from the pre-satellite era, but as only landfalling storms are examined, the likelihood of missing storms in the record is reduced. The storms were separated into three categories based on maximum wind speed whilst within the specified domain using the Saffir-Simpson Hurricane Scale (SSHS) (Simpson and Saffir, 1974). Low intensity storms include tropical depressions and tropical storms (up to 32 ms^{-1}, 63 knots). Medium intensity include category one and two storms (up to 49 ms^{-1}, 95 knots). High intensity storms were any that had a higher wind speed. A time series of seasonal frequency of each intensity storm was created (count-JJASO) spanning 57 years, from 1958-2014.

The standard temporal resolution of storm data is 6-hourly, however, at times there are missing time steps or additional data at a higher frequency. Storm data was interpolated onto a 6-hourly time period for the calculation of accumulated cyclone energy (ACE), which is used as a proxy for damage. ACE is proportional to the kinetic energy of the system and is used to express the activity of individual tropical cyclones by summing the square of the wind speed across every 6-hourly time step:

$$\text{ACE } (10^4 \text{ knots}^2) = 10^{-4} \sum v_{max}^2 \tag{3.1}$$

where v_{max} is estimated wind speed in knots and sum is over all 6-hourly time steps recorded.

The ACE-JJASO is the sum of ACE for each storm over the season (June-October) and takes into account the number, strength, and duration of all the tropical storms occurring. This a time series of one value for each season for 57 years (1958-2014).

$$\text{ACE-JJASO} = \sum ACE \tag{3.2}$$

where sum is all storms in June, July, August, September and October.

Two time series of ACE-JJASO are calculated. One uses only the 6-hourly points within the blue polygon in figure 3.1 to calculate the ACE of each storm ('domain'), and the other uses all 6-hourly time steps for the entire length of the track ('entire'). In summary, three time series of storm data are calculated:

- count-JJASO
- ACE-JJASO ('domain')
- ACE-JJASO ('entire')

Power Dissipation Index (PDI) (10^4 knots^3) is an alternative measure of tropical cyclone destructiveness, and uses the cube of the maximum wind speed rather than the square. PDI is similar to ACE but puts more emphasis on storm intensity. As this metric is just a factor of ACE, they will be highly correlated and so ACE alone will be used.

3.3.2 Large-scale environmental data

The large-scale environmental data is from various reanalysis datasets (table 3.1), with the atmospheric data from JRA-55, produced by the Japanese Meteorological Agency (JMA) (Kobayashi et al., 2015). The SST data from the Extended Reconstructed SST (ERSSTv4) dataset (Huang et al., 2015) covers over 150 years, starting in 1854. With the increased availability of sub-surface ocean observations, there are recent reanalyses that include deeper oceanic data. The NCEPCFSR coupled reanalysis (Saha et al., 2010) provides the tropical cyclone heat potential (TCHP) data, which is the OHC down to the 26°C isotherm, however, data is only available from 1979-2010 and only extends to areas with tropical cyclone activity. An alternative product for data on the deeper ocean is the ORAS4 reanalysis (Balmaseda et al., 2013) produced by ECMWF. Vertically integrated temperature (VIT) from this dataset is analysed at 100 m (shallowest available), 300 m and 700 m. Monthly means of the variables were created along with means of multiple months, e.g. January, February, March (JFM); June, July, August, September, October (JJASO).

3.3.3 Correlation analysis

To produce correlation maps, ACE-JJASO ('domain' and 'entire') and count-JJASO time series are correlated with the time series of any individual variable (table 3.1) at each grid point. ACE-JJASO ('domain') uses only the 6-hourly points within the specified domain to calculate the ACE of each storm, whereas ACE-JJASO ('entire') uses all 6-hourly time steps

Table 3.1 Details of atmospheric and oceanic datasets used

Dataset	Variable	Resolution (grid points)	Years
JRA-55 (Kobayashi et al., 2015)	MSLP, heat flux	1.25° (145 x 288)	1958-2013
ERSSTv4 (Huang et al., 2015)	SST	2° (89 x 180)	1970-2014
ORAS4 (Balmaseda et al., 2013)	VIT	1° in Extra-Tropics, refined in Tropics, with minimum of 0.3^0 at equator (180 x 360 for 1°)	1958-2009

Table 3.2 Interpretation of correlation coefficient (Boddy and Smith, 2009)

Correlation coefficient	Correlation strength
.70 or higher	very strong
.40 to +.69	strong
.30 to +.39	moderate
.20 to +.29	weak

for the entire length of the track. The correlation coefficient (table 3.2) is a measure of the linear dependence between two variables, calculated by dividing the covariance of the two variables by the product of their standard deviations.

3.4 Results

3.4.1 Storm activity

This initial part of the analysis provides a time series of storm activity during JJASO that can be used to examine relationships with various other large-scale variables in the following section. In the low intensity group (tropical storms and depressions), there are 204 storms over the 57 year period (1958-2014). There are 177 in the medium intensity (categories 1, and 2), and 63 in the high intensity (categories 3, 4 and 5) (figure 3.2). There is large interannual variability in each category in terms of ACE-JJASO ('domain' and 'entire') and count-JJASO.

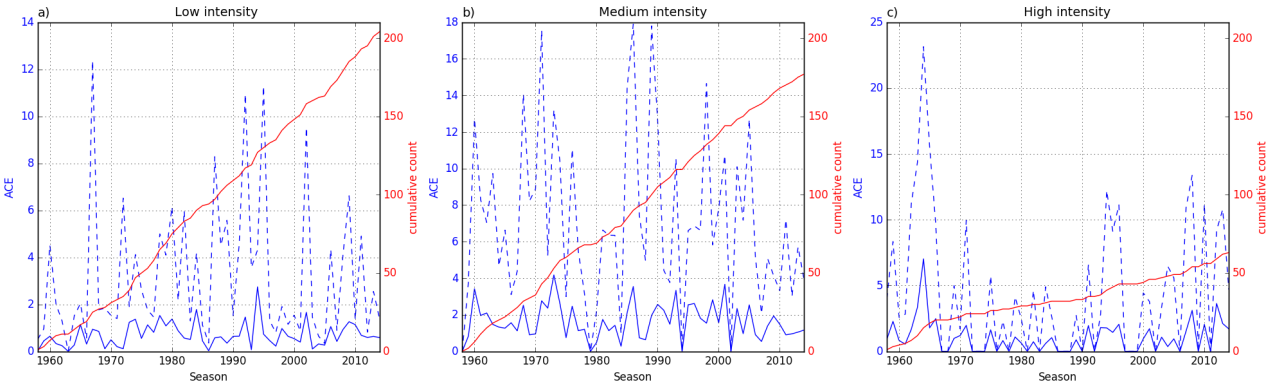


Fig. 3.2 Time series of ACE ('domain') (solid blue line), ACE ('entire') (dashed blue line) and cumulative count (red line) for a) low, b) medium, c) high intensity storms. ACE units 10^4 knots^2. ACE-JJASO ('domain') uses only the 6-hourly points within the specified domain to calculate the ACE of each storm, whereas ACE-JJASO ('entire') uses all 6-hourly time steps for the entire length of the track.

Table 3.3 Cross-correlations of ACE-JJASO ('domain'), ACE-JJASO ('entire') and count over 57 years (1958-2014). Bold indicates significance at p<0.01. ACE-JJASO ('domain') uses only the 6-hourly points within the specified domain to calculate the ACE of each storm, whereas ACE-JJASO ('entire') uses all 6-hourly time steps for the entire length of the track.

	Intensity	ACE (entire)	count
ACE (domain)	Low	**0.43**	**0.79**
	Medium	**0.73**	**0.86**
	High	**0.89**	**0.93**
ACE (entire)	Low	-	**0.52**
	Medium	-	**0.79**
	High	-	**0.96**

The cross-correlations of these three time series are significant at the 99th percentile, and correlation strength increases with storm intensity (table 3.3). ACE-JJASO ('entire') has less relevance for the landfalling impact and is omitted from further analysis, as it uses all 6-hourly time steps for the entire length of the track whereas ACE-JJASO ('domain') uses only the 6-hourly points within the specified domain. The strong positive correlations of these two datasets in table 3.3 suggest that similar relationships would be found when comparing against the large-scale variables. In the following section, ACE-JJASO ('domain') and count-JJASO are correlated against large-scale variables, and ACE-JJASO refers to ACE-JJASO ('domain').

3.4.2 Correlation between storm activity and large-scale variables

The following maps show the correlation between the environmental variable at each grid point and ACE-JJASO and count-JJASO over the available period from 1958. The lengths of the time series are 57 years for SST (to 2014), 56 years for atmospheric variables (to 2013) and 52 years for VIT (to 2009). The stippled areas are significant at the 95th percentile ($p<0.05$). Solid black contour lines are shown at intervals of 0.1 correlation when the coefficient is less than or equal to -0.4 and more than or equal to 0.4.

Sea surface temperature (SST) and vertically integrated temperature (VIT)

The correlation maps for ACE-JJASO and count-JJASO with SST in JJASO show similar patterns (figure 3.3), suggesting that the relationship with SST is dominated by frequency of storms rather than intensity. The plots also show that there are notable differences in the relationship between SST and tropical storm activity for different intensity storms. For the low intensity storms (figure 3.3b), there is an area of significant positive correlation in the Philippine Sea, extending northwards encompassing the East China Sea and eastwards to the east of Japan. When the SST here is anomalously warm, there are an increased number of tropical storms and depressions making landfall over the domain of interest, and vice versa. There is no obvious relationship between the SST distribution and the potential intensification of storms passing above, i.e. anomalously warm water in the immediate vicinity of the landfall domain for the most intense storms is not present. On a seasonal mean time scale, as presented, any local signal will be averaged out and there are numerous other factors that lead to intensification (see section 2.2). It is possible that the strong positive correlation with SST seen upstream of the landfall domain for the weaker storms could encourage cyclone generation or be associated with atmospheric processes that enable cyclogenesis. The potential formation of storms close to the landfall domain without the time to intensify would increase the frequency of low intensity storms. For the medium intensity storms, there is a significant negative correlation in the central equatorial Pacific (figure 3.3d), and for the intense storms (figure 3.3,e,f), a correlation of ~0.5 is apparent in the northern North Pacific. No regions of significant correlation are observed across all of the different categories. Figures 3.3g,h show the relationship with all storms, and the largest area of significant correlation is the equatorial Pacific, with a negative correlation. This negative correlation, dominated by the medium and intense storms is likely to be related to El Niño, which varies on an interannual time scale. In both cases, the correlation is negative, suggesting that during El Niño (Central Pacific case for medium and East Pacific for intense), there are fewer storms making landfall in the selected domain. This is to be expected, as

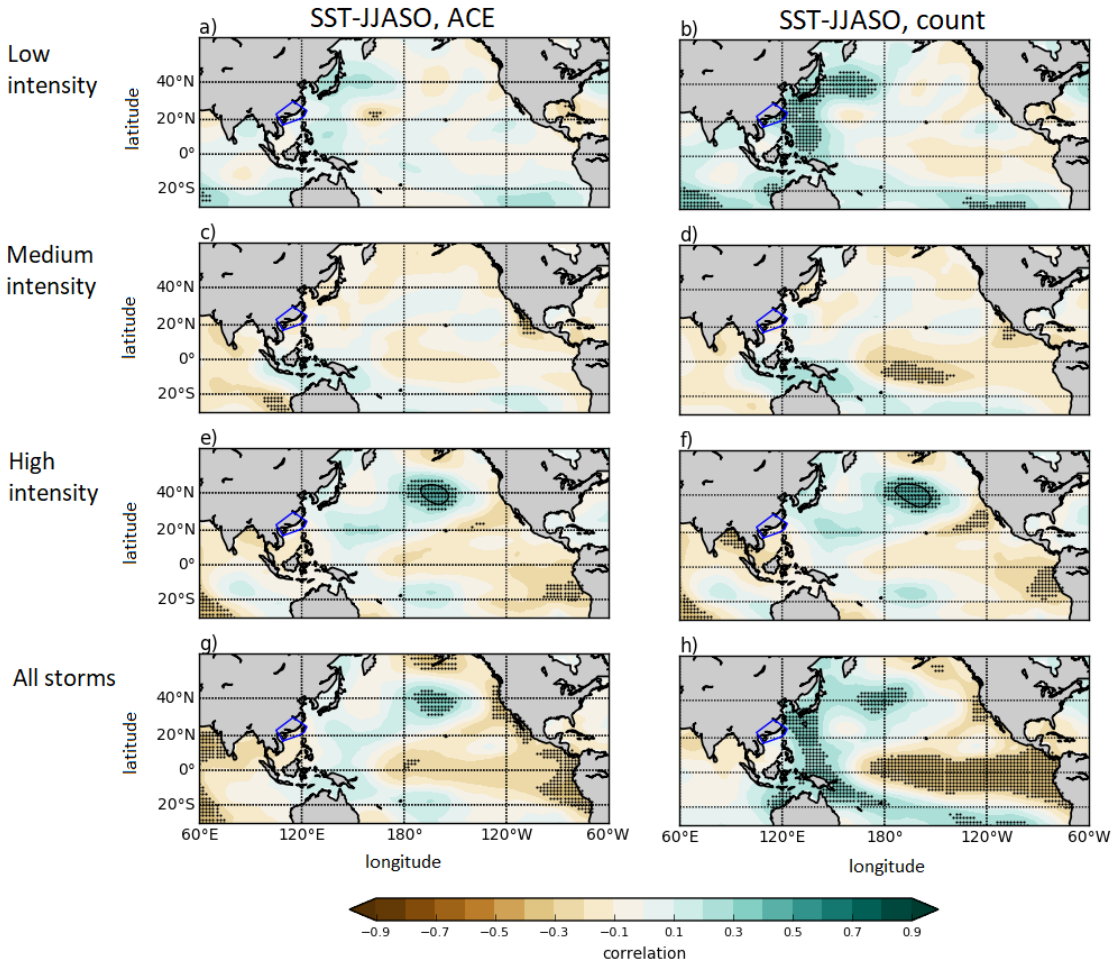


Fig. 3.3 SST-JJASO correlated with ACE (a,c,e,f) and count (b,d,f,h) over the period 1958-2014 for storms separated by intensity and all storms. Low intensity (tropical storms and tropical depressions), medium intensity (categories 1,2), high intensity (categories 3, 4, 5). Stippling indicates grid points with significant correlation at the 95th percentile and solid (dashed) contour lines are shown where correlation values are >=0.4 and <=-0.4. Storm domain shown as blue polygon.

during El Niño more storms are generated further south-east, and they tend to recurve before landfall, with fewer across the Philippines and South China Sea (section 2.3). Although the El Niño signal is strongest in the equatorial Pacific, there is also a signal in the central North Pacific at a higher latitude (figure 3.4). This is the location where the positive correlation is seen in the intense storms (figure 3.3,e,f).

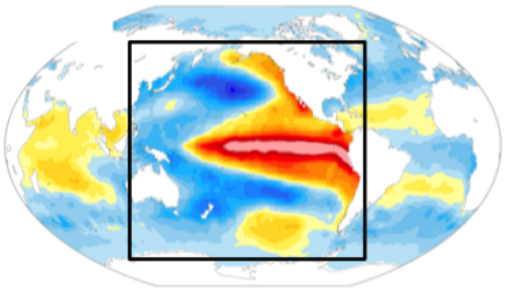


Fig. 3.4 SST anomaly pattern associated with an El Niño event obtained by linearly regressing monthly SST anomalies at each grid box upon the leading Principal Component (PC) time series based on the domains outlined in the black boxes. Source: https://climatedataguide.ucar.edu/climate-data

When correlating ACE-JJASO and count-JJASO with SSTs in the year prior to the storm season, the most consistent and significant signal is seen in JFM ('JFM-1'). The lag between these anomalies and the storm activity is approximately 18 months (figure 3.5).

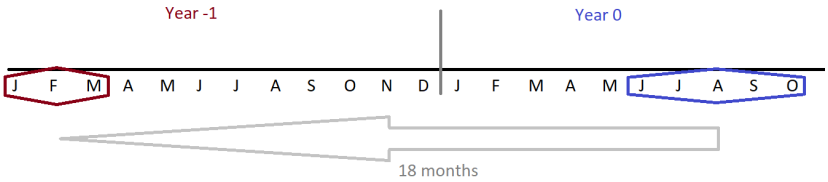


Fig. 3.5 Time line showing lag between JJASO season in which storm count and ACE are calculated and JFM-1 in the previous year. There are 18 months between February and August of these two years.

There is a striking anti-correlation between the relationship for the low intensity storms (figure 3.6a,b) and the high intensity storms (figure 3.6e,f) with SST in the JFM of the previous year ('JFM-1'). These correlations are seen off the east coast of mainland China, in the East China Sea and in the Bay of Bengal (red box), and also in a horse-shoe shape to the east and north (purple box), where correlations are of the opposite sign. For the medium intensity storms, however, there is no significant correlation with SST in these regions. The correlation between the time series of frequency of low intensity storms and high intensity storms is -0.183 (p=0.174), which is an insignificant very weak negative correlation. The

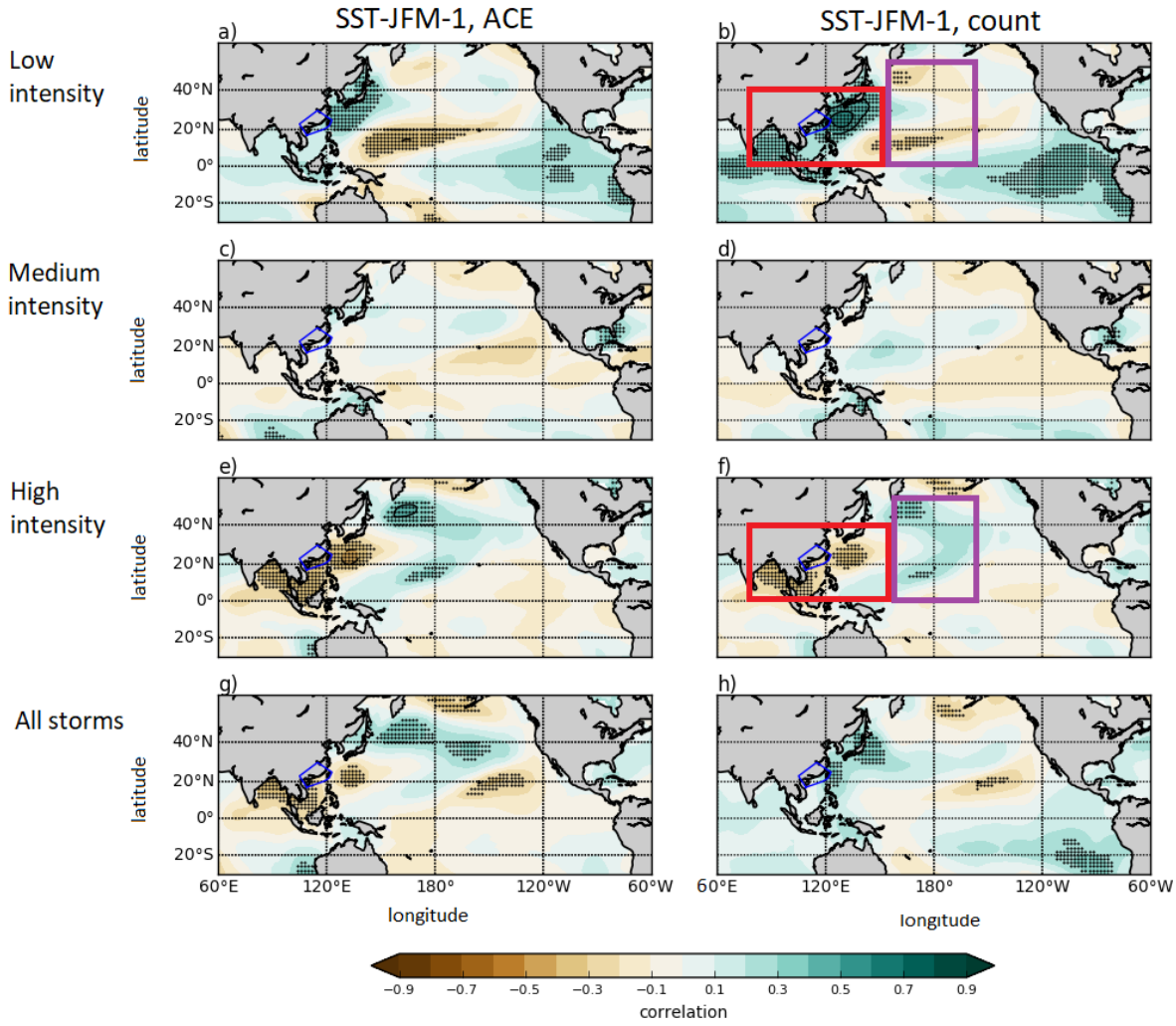


Fig. 3.6 SST JFM-1 correlated with ACE (a,c,e,f) and count (b,d,f,h) over the period 1958-2014 for storms separated by intensity and all storms. Low intensity (tropical storms and tropical depressions), medium intensity (categories 1,2), high intensity (categories 3, 4, 5). Stippling indicates grid points with significant correlation at the 95th percentile and solid (dashed) contour lines are shown where correlation values are >=0.4 and <=-0.4. Storm domain shown as blue polygon. Red and purple boxes highlight areas of strong opposing correlations between low and high intensity storm counts.

opposing signs are therefore not simply a result of anti-correlated counts of these storms. The low intensity storms also have a large region of positive correlation in the eastern equatorial Pacific, suggesting that ~18 months after an El Niño event, there will be increased frequency of weak storms in the landfall domain.

SST in this same season (JFM) has been correlated with count-JJASO and ACE-JJASO, but during the following year, i.e. the same year as the storm season (SST-JFM) (figure 3.7). The correlation pattern for the intense storms resembles that of SST-JJASO (figure 3.3f), with the signals further west (as seen in JFM-1, figure 3.6f) not observed. In the case of the low intensity storms, the same signal in the East China Sea and Philippine Sea is apparent during this season, although over a smaller region. This area of interest to the east of mainland China (red and purple boxes in figure 3.6) will be further examined, focussing on the weak and intense storms only. Future correlation maps will show the relationship with count, as the observations are subject to less error than wind speed, which is used to calculate ACE.

To assess whether the signals seen in figures 3.3 and 3.6 are stable throughout the 57 years, the results have been broken down into three periods that coincide with different Pacific Decadal Oscillation (PDO) phases (cold, warm and mixed) (figure 3.8, table 3.4).

Table 3.4 Years in cold, warm and mixed PDO periods, defined using the Pacific Decadal Oscillation Index time series.

Years	Number of years	PDO state
1958-1975	18	cold
1976-1997	22	warm
1998-2014	17	mixed

The positive correlation between SST-JJASO and count-JJASO seen to the east of Japan for the low intensity storms (figure 3.3b) is strong in the middle (warm period) (figure 3.9b), with no significant correlations in the other periods. The positive correlation in the Philippine Sea and East China Sea is present in less coherent regions and is not as strong. For the high intensity storms, the positive correlation in the northern North Pacific (at approximately 160°W and 40°N) is apparent in all periods, and is strongest during the cool phase when it exhibits a dipole with the Kuroshio current region.

Figure 3.10 shows the correlation maps between count and SST-JFM-1 broken down into the three different PDO periods. The strong correlations off the east coast of China into the Bay of Bengal and the opposing correlations extending to the east of this region (figure 3.6) are dominated by the early period (cold PDO), for both the weak and intense storms (figures 3.10a,d). In the warm PDO phase, the sign remains consistent for the low intensity storms

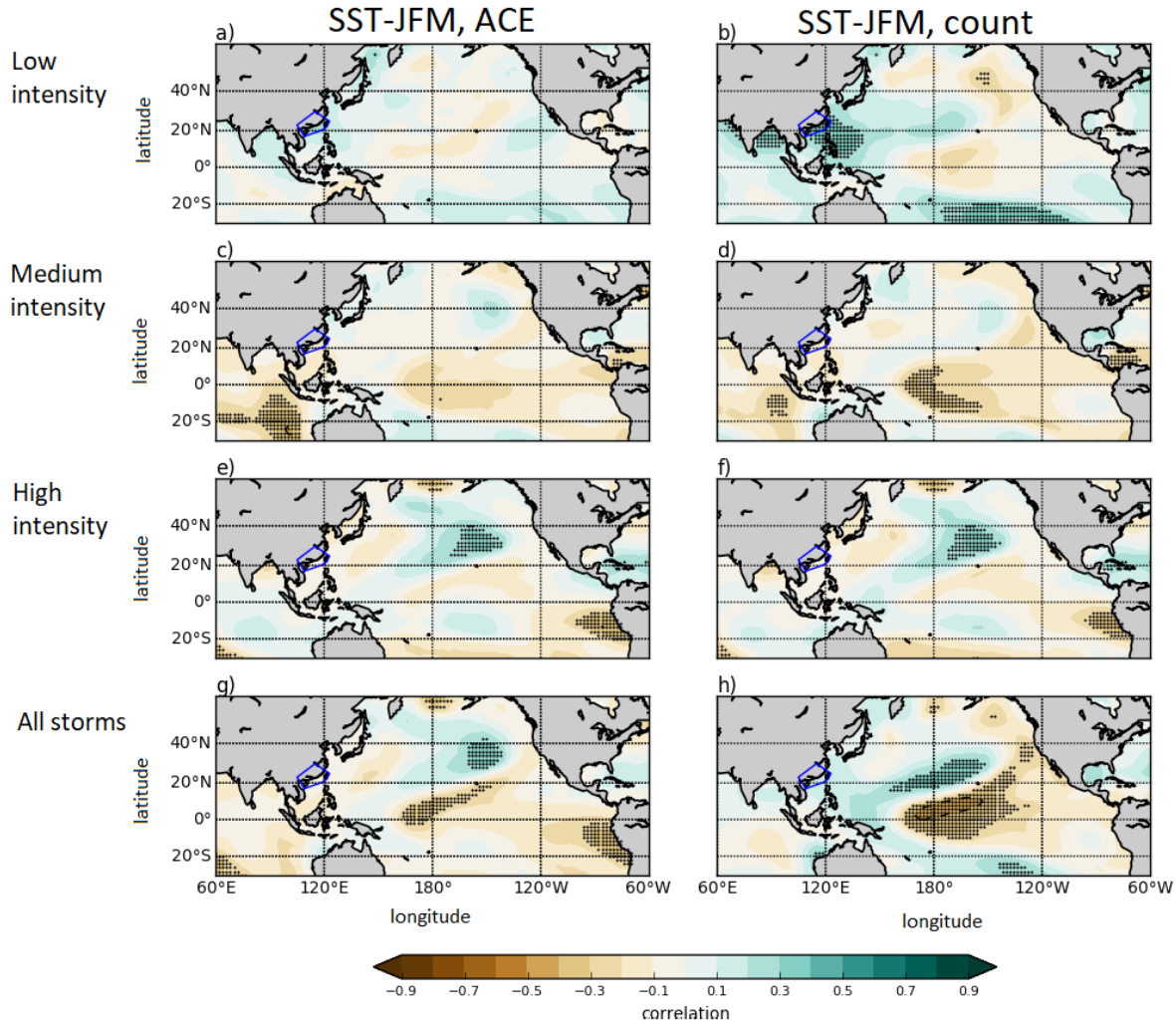


Fig. 3.7 SST JFM correlated with ACE (a,c,e,f) and count (b,d,f,h) over the period 1958-2014 for storms separated by intensity and all storms. Low intensity (tropical storms and tropical depressions), medium intensity (categories 1,2), high intensity (categories 3, 4, 5). Stippling indicates grid points with significant correlation at the 95th percentile and solid (dashed) contour lines are shown where correlation values are >=0.4 and <=-0.4. Storm domain shown as blue polygon.

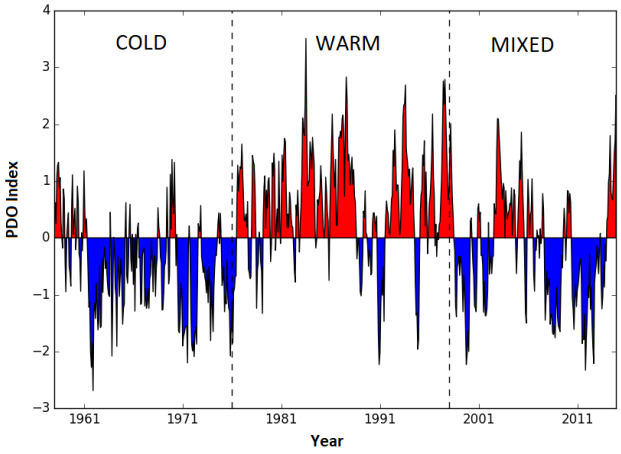


Fig. 3.8 The Pacific Decadal Oscillation Index time series 1958-2014. Cold, warm and mixed phases marked.

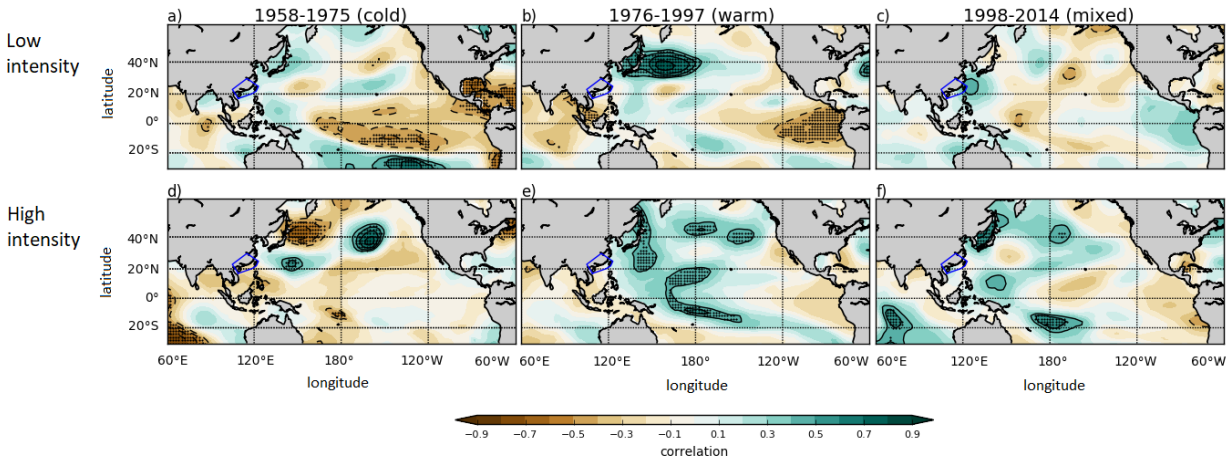


Fig. 3.9 SST-JJASO correlated with count during (a,d) 1958-1975, (b,d) 1976-1997, (c,f) 1998-2014 for low (tropical storms and tropical depressions) and high intensity storms (categories 3, 4, 5). Stippling shows grid points with significant correlation at 95th percentile and solid (dashed) contour lines are shown where correlation values are >=0.4, <=-0.4. Storm domain shown as blue polygon.

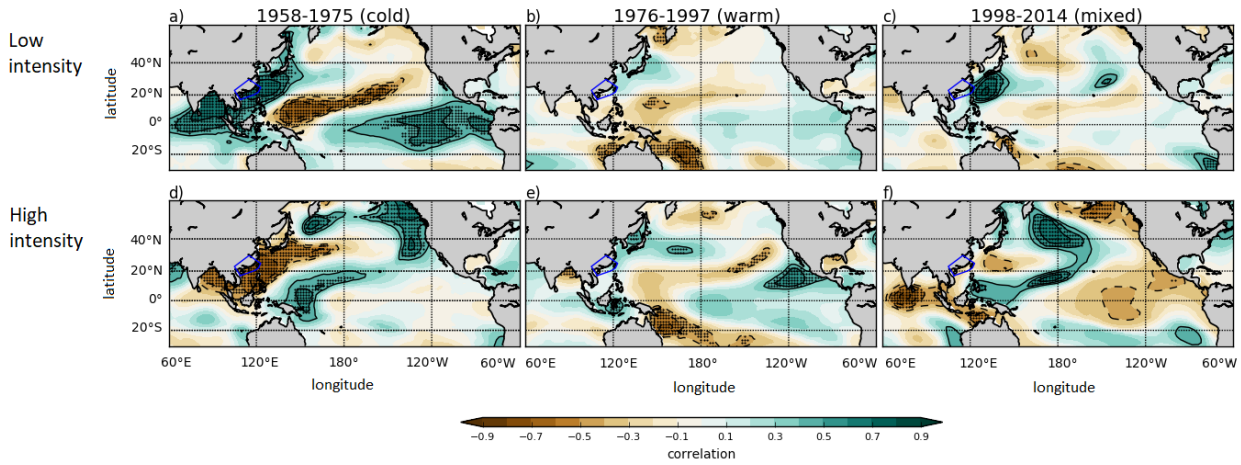


Fig. 3.10 SST JFM-1 correlated with count during (a,d) 1958-1975, (b,d) 1976-1997, (c,f) 1998-2014 for low (tropical storms and tropical depressions) and high intensity storms (categories 3, 4, 5). Stippling shows grid points with significant correlation at 95th percentile and solid (dashed) contour lines are shown where correlation values are >=0.4, <=-0.4. Storm domain shown as blue polygon.

although it appears to reverse for the high intensity storms (admittedly with few points of significance) (figures 3.10b,e). In the mixed period, parts of the pattern seen in figure 3.10a,d are observed, although less coherent and less intense (figures 3.10c,f).

It is not only the sea surface that affects tropical storm activity, but the deeper ocean can have an influence (section 2.2.1), therefore the vertically integrated temperature (VIT) is also investigated. The mean VIT to 100m during the JJASO season (not shown) shows a very similar pattern to SST (figure 3.4), with an area of relatively warm water extending from the tropics to approximately 30°N. Water in the west of the basin is warmer than in the east, where there is upwelling of cooler water. Figure 3.11 shows the correlations between count and VIT-JJASO over 100 m, 300 m and 700 m, which can be compared to the SST correlation maps over the same period (figure 3.3). VIT data is at least twice the resolution of SST (1° to 0.3°, rather than 2°, table 3.1) and so more detail is apparent. For the low intensity storms, the overall pattern is similar, but with different correlation strength. The positive correlations in the Philippines Sea, East China Sea and along the Kuroshio current are not as clear in VIT as in SST, although there are some stippled grid points, especially close to the east coast of the mainland. The positive correlation in the northern North Pacific for the intense storms is present in SST (figures 3.3f) and all VIT levels, although it becomes less coherent with depth (figures 3.11b,d,f). For the low intensity storms, there is a significant negative correlation in the equatorial Pacific, extending throughout all depths shown. This relationship is not apparent in SST and is weakest and smallest in the shallowest VIT (100m). This suggests

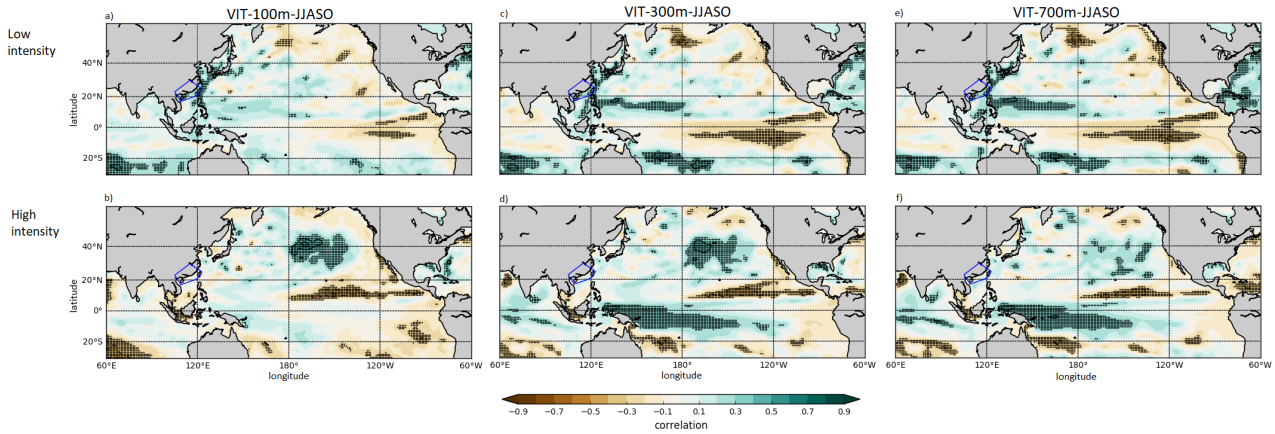


Fig. 3.11 VIT-JJASO correlated with count during 1958-2009 for low intensity storms over a) 100m, c) 300m, and e) 700 m and high intensity storms over b) 100m, d) 300m, and f) 700 m. Stippling shows grid points with significant correlation at 95th percentile and solid (dashed) contour lines are shown where correlation values are >=0.4, <=-0.4. Storm domain shown as blue polygon.

that in an El Niño year, where this water is anomalously warm, there are fewer weak storms making landfall in the domain of interest. There is also a coherent equatorial region of correlation for the high intensity storms that is not apparent in SST alone, but is visible in the 300 m and 700 m VIT. This positive correlation is seen to the west of the basin, extending from Indonesia to ~140°W. The negative correlation in SST in the equatorial Pacific (figures 3.3f) is seen in the upper 100 m in VIT (figures 3.11b), below which it becomes insignificant.

When count-JJASO is correlated with VIT-JFM-1, across all depths shown the pattern remains largely consistent. VIT-JFM-1 over the top 100m (figure 3.12) shows the opposing correlations for weak and intense storms in the East China Sea, although this is less extensive and does not extend into the Bay of Bengal and towards the Aleutian Islands as in SST (figure 3.6). With depth, this region of positive correlation for the low intensity storms remains significant (albeit reduces in size), however it weakens and becomes insignificant for the high intensity storms. As well as these oceanic variables, a number of atmospheric variables were analysed using the JRA-55 reanalysis data.

Atmospheric variables

Figure 3.13 shows the mean sea level pressure (MSLP) during JJASO, and the subtropical high is clearly visible, centred off the west coast of the USA and extending westwards towards Asia. The mean sea level pressure across the mid and high latitudes is more variable

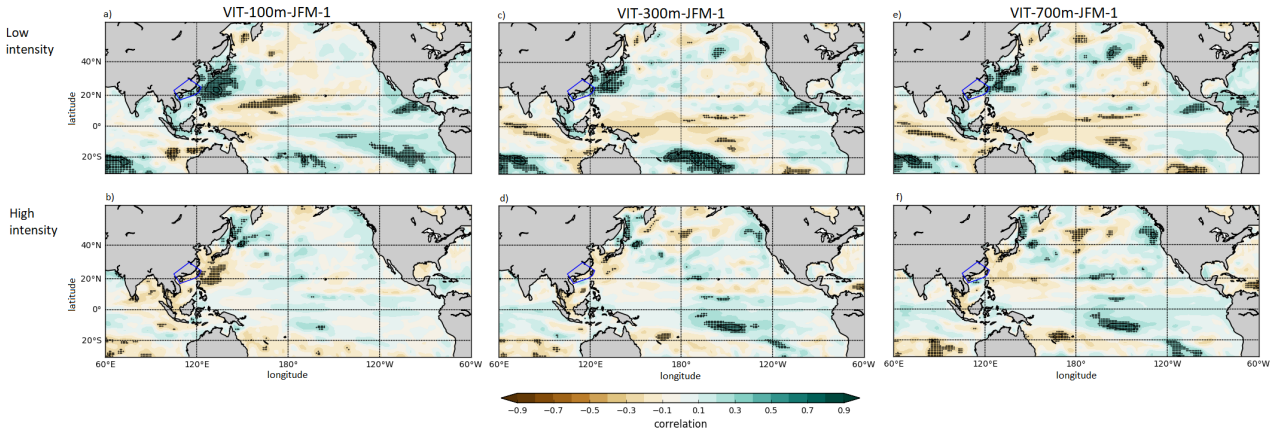


Fig. 3.12 VIT-JFM-1 correlated with count during 1958-2009 for low intensity storms over a) 100m, c) 300m, and e) 700 m and high intensity storms over b) 100m, d) 300m, and f) 700 m. Stippling shows grid points with significant correlation at 95th percentile and solid (dashed) contour lines are shown where correlation values are >=0.4, <=-0.4. Storm domain shown as blue polygon.

year to year than across the Tropics. This can be predicted given geostrophic balance (section 2.8.1), due to the small Coriolis force at low latitudes, increasing towards the poles.

During the storm season, there is an area of significant correlation with mean sea level pressure (MSLP-JJASO) in the East China Sea and South China Sea for the low intensity storms (figure 3.14a), which is at the same location as the significant positive signal seen in SST-JJASO (figure 3.3b). When mean sea level pressure is anomalously high (and SST anomalously low), there is a decrease in the frequency of low intensity storms making landfall in the domain. This signal of low mean sea level pressure may reflect the presence of convective systems, which are a prerequisite for tropical cyclone formation (section 2.1), or may be due to the presence of tropical cyclones in this region, lowering the mean sea level pressure in the reanalysis. For the high intensity storms, there is a region of significant positive correlation with MSLP-JJASO in the northern North Pacific, although this is slightly shifted to the north and is weaker than the signal seen in SST-JJASO (figure 3.3f). This co-location between the positive correlation of high intensity storm count and mean sea level pressure and SST at ~40°N may relate to the Pacific North American pattern (PNA). In the positive phase, there is high pressure over the western USA and low pressure to the east and over the north-east Pacific. This phase of the PNA pattern tends to be associated with El Niño, and the negative phase tends to be associated with La Niña. The positive correlation seen here with the intense storms suggests that when the SST is anomalously high and there is higher MSLP (negative PNA, La Niña), there are more intense storms in the domain. This

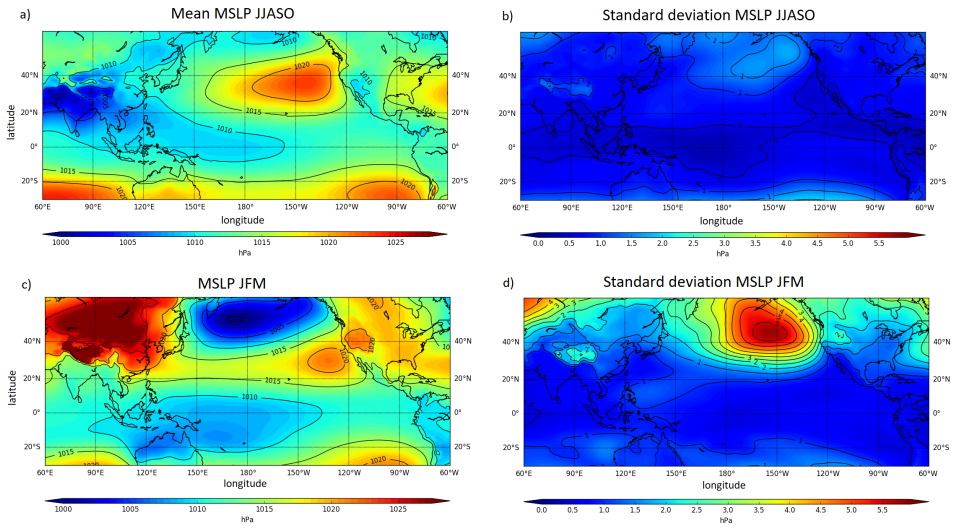


Fig. 3.13 Mean sea level pressure climatology 1958-2014. (a) JJASO mean (b) JJASO standard deviation (c) JFM mean (d) JFM standard deviation.

again reinforces the suggestion that storms form further west in this situation, with increased landfall in southern China.

The regions of strong correlation apparent in SST-JFM-1 (figure 3.6) are not observed when analysing mean sea level pressure in the previous JFM (MSLP-JFM-1). There are large regions of positive correlation over the ocean for the weak storms, notably in the Indian Ocean. In the eastern and central equatorial Pacific, opposing significant correlations are seen between SST and MSLP.

Heat flux

Latent heat flux (Wm^{-2}) is the flux of heat from the Earth's surface to the atmosphere that is associated with evaporation of water at the surface and subsequent condensation of water vapour in the troposphere. Sensible heat flux is related to changes in temperature with no change in phase. The sum of these is the turbulent heat flux and in this study, positive heat flux is from the ocean to the atmosphere. The turbulent heat flux can play a forcing or damping role (Frankignoul et al., 1998), which can be examined using correlations between SST and heat flux (figure 3.16). If the ocean is warmed or cooled by internal processes and leads to changes in heat flux, there will be a positive correlation between the two and the atmosphere damps these changes in SST. However, if there is a negative correlation, the SST will lag the heat flux as it is forced by the atmosphere. During the JJASO season, turbulent heat flux is generally consistent across longitude bands, with lower values towards the poles (figure 3.15). In JFM, the largest heat fluxes are dominated in a small region around the

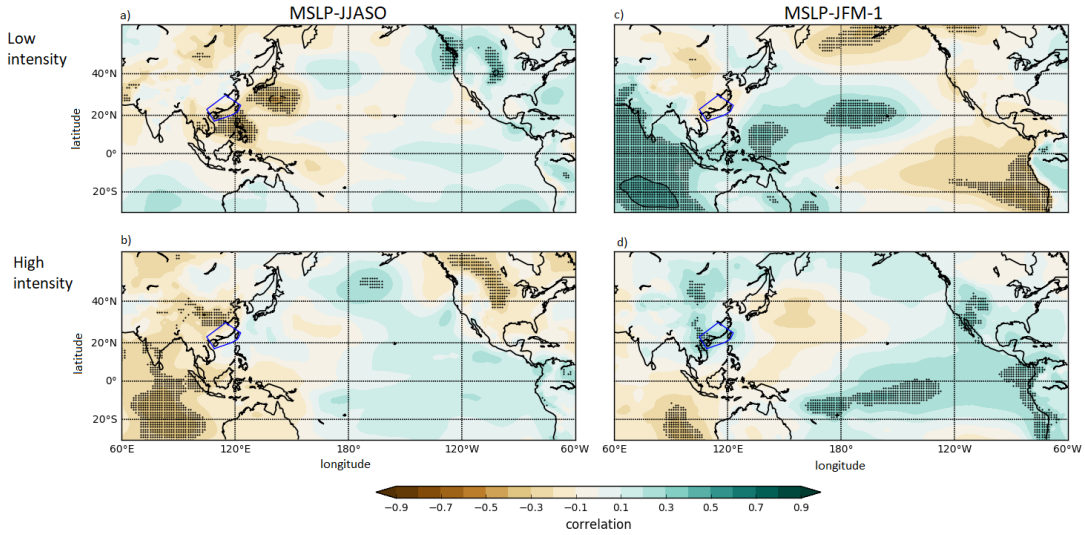


Fig. 3.14 MSLP-JJASO correlated with count during 1958-2013 for (a) low and (b) high intensity storms. MSLP-JFM-1 correlated with count for (c) low and (d) high intensity storms. Stippling shows grid points with significant correlation at 95th percentile and solid (dashed) contour lines are shown where correlation values are >=0.4, <=-0.4. Storm domain shown as blue polygon.

Kuroshio current and Gulf Stream. These warm ocean currents transfer heat upwards into the relatively cool atmosphere.

Correlation of heat flux during JJASO (HF-JJASO) and storm count for the low intensity storms does not reveal a significant relationship around the east coast of China and Japan (figure 3.17a), which was seen with the SST (figure 3.3b). However, for the intense storms, there is a positive correlation observed in the same region in the northern North Pacific (figure 3.17b) as seen in the SST (figure 3.3). As the same sign of correlation is seen, the SST is leading the heat flux and is being damped by the atmosphere. The correlation between storm count and heat flux the previous year (HF-JFM-1), has only a few points in the Bay of Bengal with a significant correlation, compared to SST-JFM-1, where a large area shows a relationship (figure 3.6). Much of the signal in SST-JFM-1 to the east of mainland China is not observed in HF-JFM-1. However, to the east of Japan, off the southern coast of Russia, a cluster of significant points with the opposite sign to SST are observed, reflecting a forcing of the ocean by the atmosphere. Further south, at approximately 160°W, 15°N (part of the horseshoe shape previously described), SST and heat flux are positively correlated for the weak storms (figure 3.17c), suggesting that the ocean is forcing the atmosphere.

Heat flux is correlated with SST over years 1958-2013 and due to the fine spatial variability, especially in heat flux in JFM (figure 3.15), only original data without interpolation onto

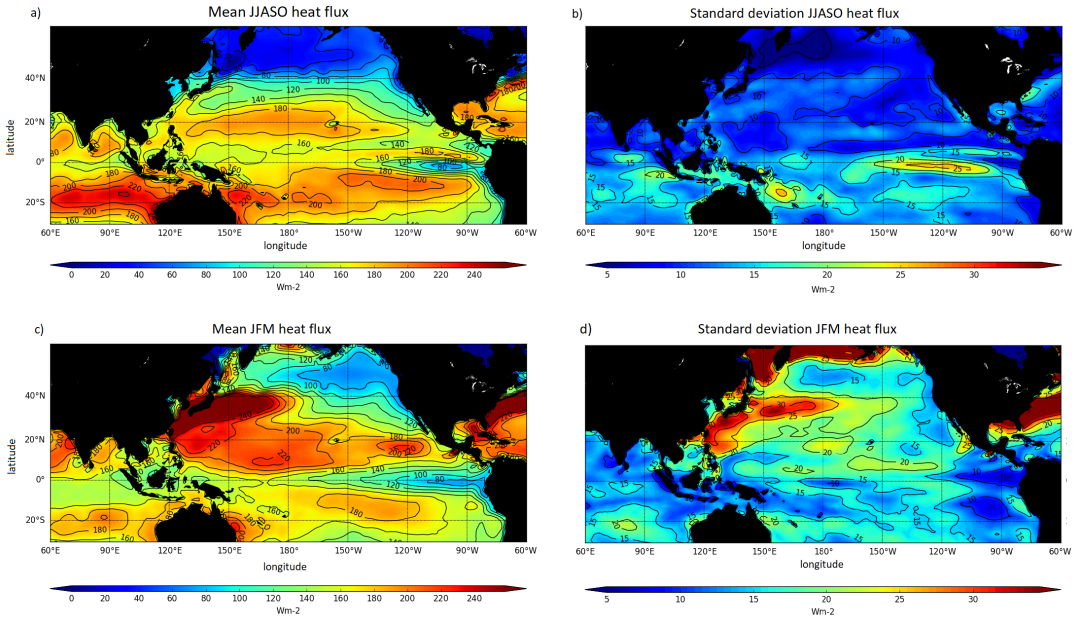


Fig. 3.15 Heat flux climatology 1958-2013. (a) JJASO mean (b) JJASO standard deviation (c) JFM mean (d) JFM standard deviation.

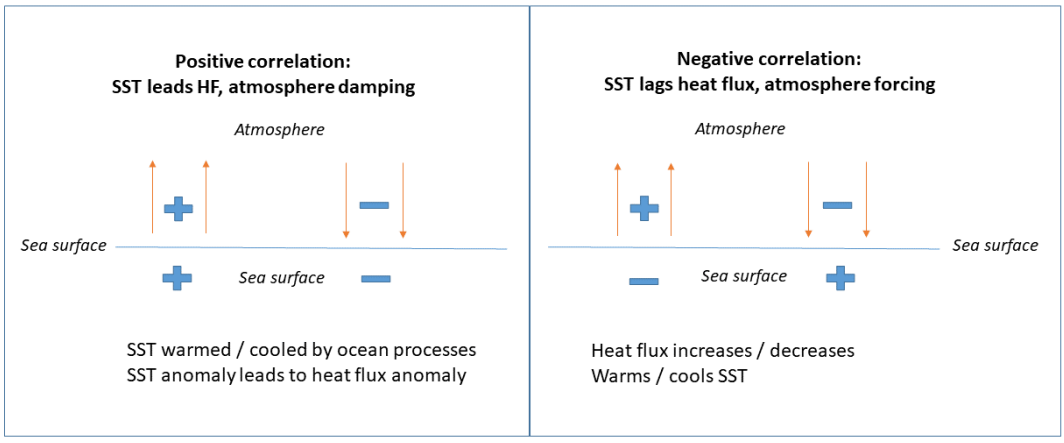


Fig. 3.16 Heat flux and SST correlation schematic. Red arrows represent direction of heat flux into the ocean or atmosphere. Plus and minus signs represent anomaly in heat flux and SST. Positive heat flux is from the ocean to the atmosphere.

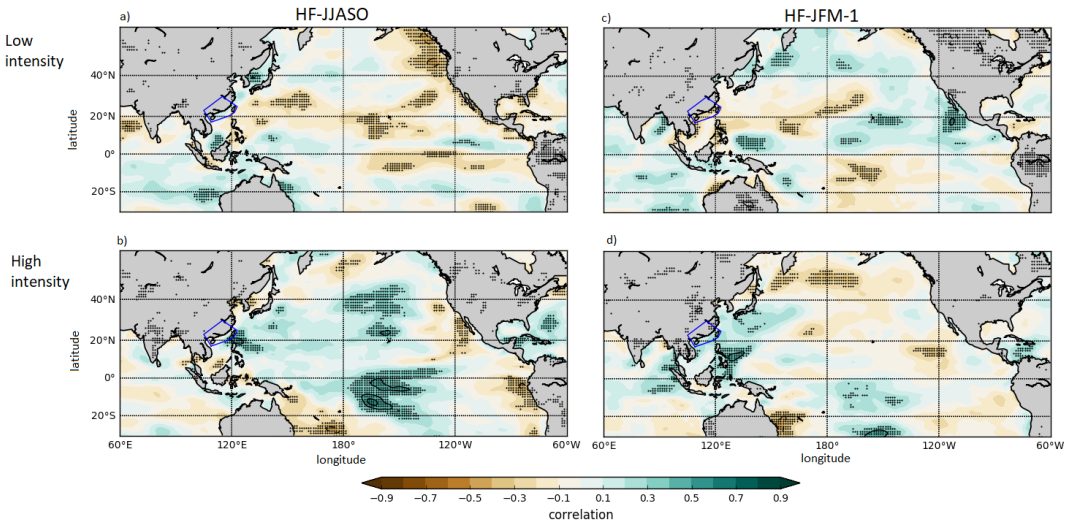


Fig. 3.17 HF-JJASO correlated with count during 1958-2013 for (a) low and (b) high intensity storms. HF-JFM-1 correlated with count for (c) low and (d) high intensity storms. Stippling shows grid points with significant correlation at 95th percentile and solid (dashed) contour lines are shown where correlation values are >=0.4, <=-0.4. Storm domain shown as blue polygon.

a finer grid was used, with matching grids every 10 degrees. Figure 3.18 shows the spatial correlations between February SST and heat flux from December, January, February, March, and April with stippling at significance level $p<0.05$. The contour colours show interpolated fields as values are only available every 10 degrees longitude and latitude. The strong correlation in the equatorial region is apparent in all plots. The correlation of February SST with heat flux in prior months (figures 3.18a,b) shows a significant negative relationship north of 20°N. When compared to the heat flux during February, this relationship weakens and in the following months, becomes positive. The negative relationship reflects the atmosphere forcing the ocean and the positive relationship shows the ocean forcing the atmosphere.

This lagged relationship between SST and heat flux is also shown for August SST (figure 3.19). The same strong positive equatorial relationship is observed in all months and some regions of negative correlation are apparent in the earlier months, however this is less significant and less coherent than in the winter.

3.4.3 Statistical model using SST

A multiple linear regression model is developed to test the predictive skill of SST of the previous JFM (JFM-1) for count-JJASO and ACE-JJASO. The regions highlighted in figure 3.6 (red and purple boxes) are separated into four distinct areas detailed in table 3.5. The

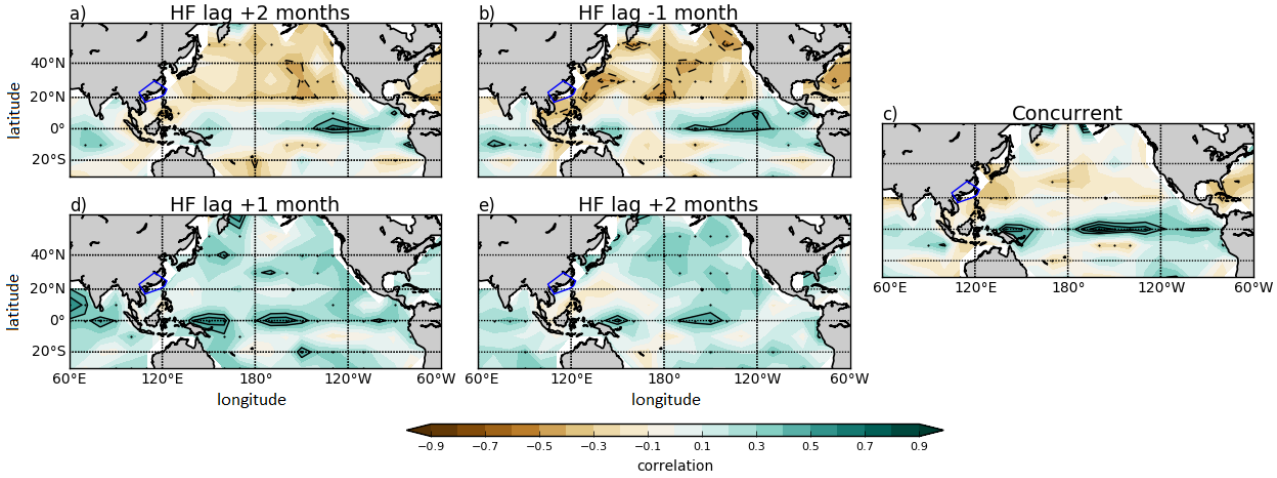


Fig. 3.18 February SST correlated with heat flux in (a) December, (b) January, (c) February, (d) March, (e) April (1958-2012). Stippling shows grid points with significant correlation at 95th percentile and solid (dashed) contour lines are shown where correlation values are >=0.4, <=-0.4. Storm domain shown as blue polygon.

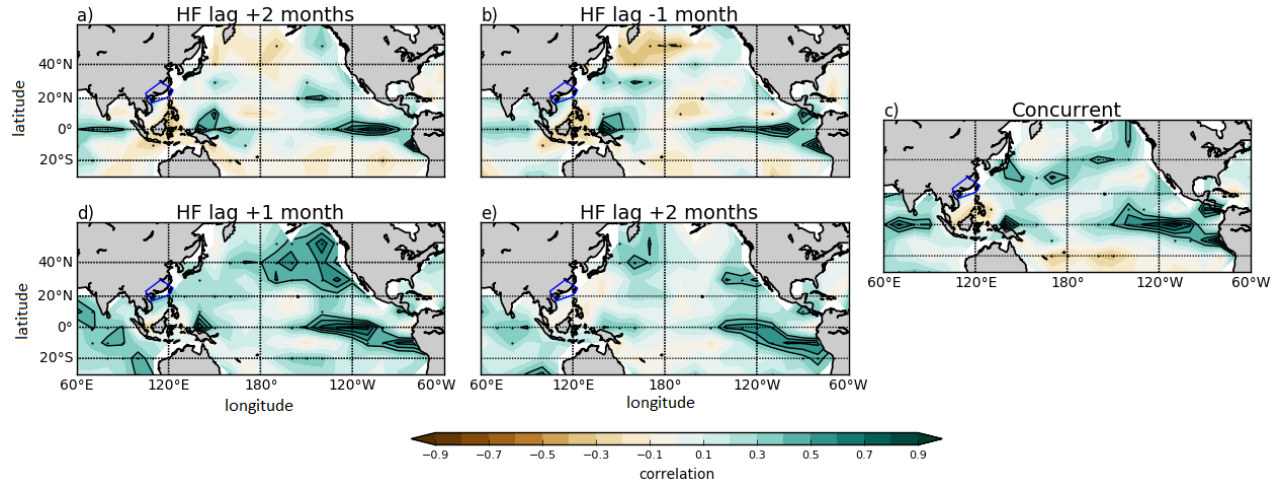


Fig. 3.19 August SST correlated with heat flux in (a) June, (b) July, (c) August, (d) September, (e) October (1958-2012). Stippling shows grid points with significant correlation at 95th percentile and solid (dashed) contour lines are shown where correlation values are >=0.4, <=-0.4. Storm domain shown as blue polygon.

Table 3.5 Regions used for statistical SST model. These are boxes taken from within the red and purple boxes presented in figure 3.6

Region name	Coordinates
Bay of Bengal (BOB)	0-20°N, 80-110°E
East China Sea (ECS)	18-40°N, 120-140°E
Central Equatorial Pacific (CEP)	0-20°N, 150-180°E
Northern North Pacific (NNP)	40-50°N, 150-180°E

mean SST over each of these regions is calculated, producing 4 time series of 57 years in length (1958-2014). The final year is omitted from the model as SST is used to make a prediction about count and ACE the following year. The multiple linear regression model uses all 4 SST datasets (BOB, ECS, CEP, NNP) from 1958-2013 as the independent variables and ACE-JJASO and count-JJASO from 1959-2014 as the dependent variables. The forecast ability of the multivariate regression model is evaluated using the standard leave-one-out cross validation (LOOCV) procedure. A model is developed using the data (length N) of N–1 segments and used to predict the remaining segment. This process is repeated by changing the segment that has been excluded from the model development (Cawley and Talbot, 2010). This is a more reliable method than splitting the data into a training and testing period in case the split is not random.

Figure 3.20 shows the time series for the observed frequency of storms and the frequency predicted by the model. The R^2 values for the low intensity and high intensity storms are 0.076 and -0.042 respectively, showing that there is negligible model skill for storm count. The negative value of the R^2 in this case is possible and means that the model fits the data poorly. The same lack of skill applies for ACE (figure 3.21), with R^2 of 0.006 for both the low and high intensity storms.

Scatter plots of the dependent variable (count or ACE) against the independent variables (SST) (figure 3.22) further illustrate the model deficiencies. In a perfect model, the points would be aligned on the x=y line. For the high intensity storms (red dots), there is a large spread, with large errors where count and ACE observed values are zero. From the 56 years there are 21 years during which there are no storms in this category. In the low intensity group, there is only 1 year during which there is a zero value observed, and although still well spread, these points are less so than those for the high intensity storms. The very limited number of samples in the intense storms limits the ability to create a skilful empirical model.

A linear trend in the time series for both count and ACE is clearly observed for the low intensity storms (figures 3.20a and 3.21a). When both the independent (SST) and dependent

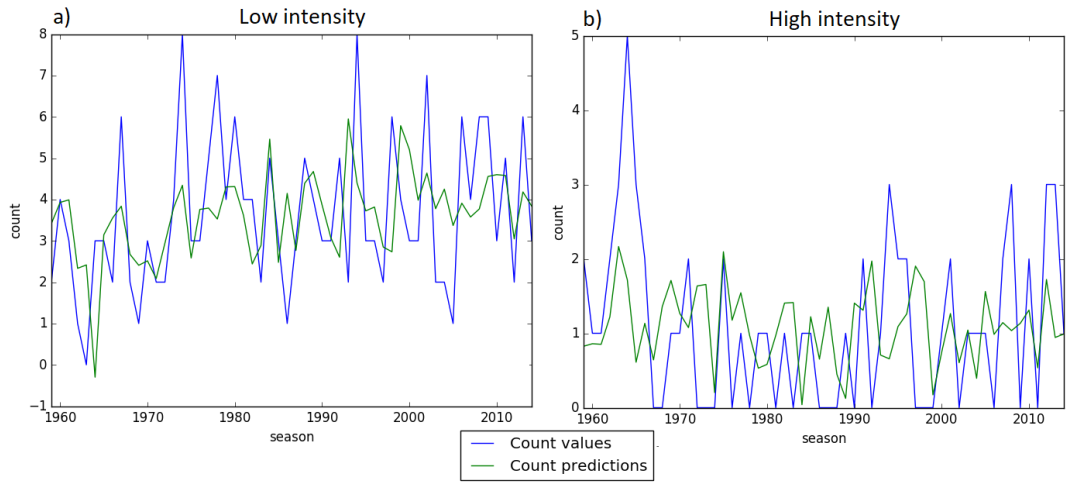


Fig. 3.20 Time series of count-JJASO observed values (blue lines) and those predicted from the model (green lines) for the a) low intensity and b) high intensity storms.

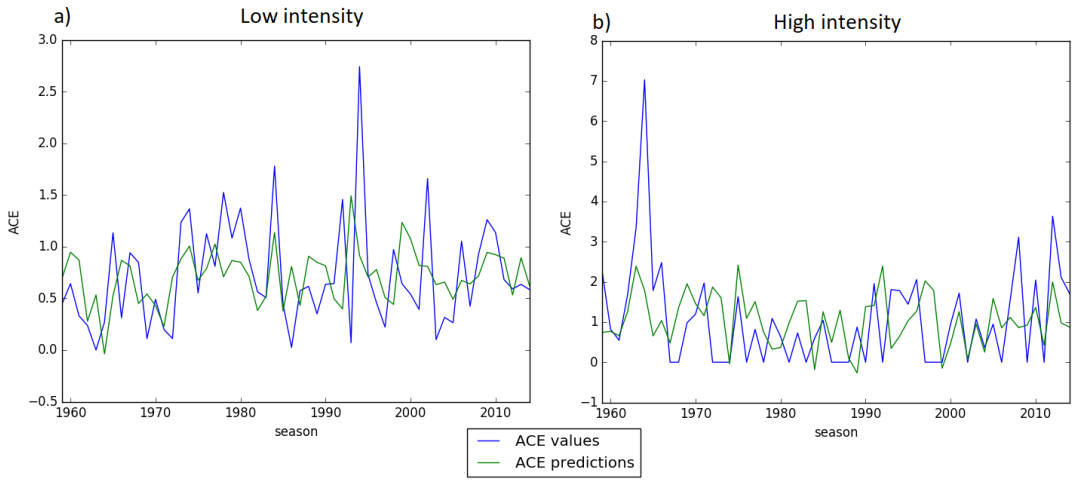


Fig. 3.21 Time series of ACE-JJASO observed values (blue lines) and those predicted from the model (green lines) for the a) low intensity and b) high intensity storms. ACE units 10^4 knots^2

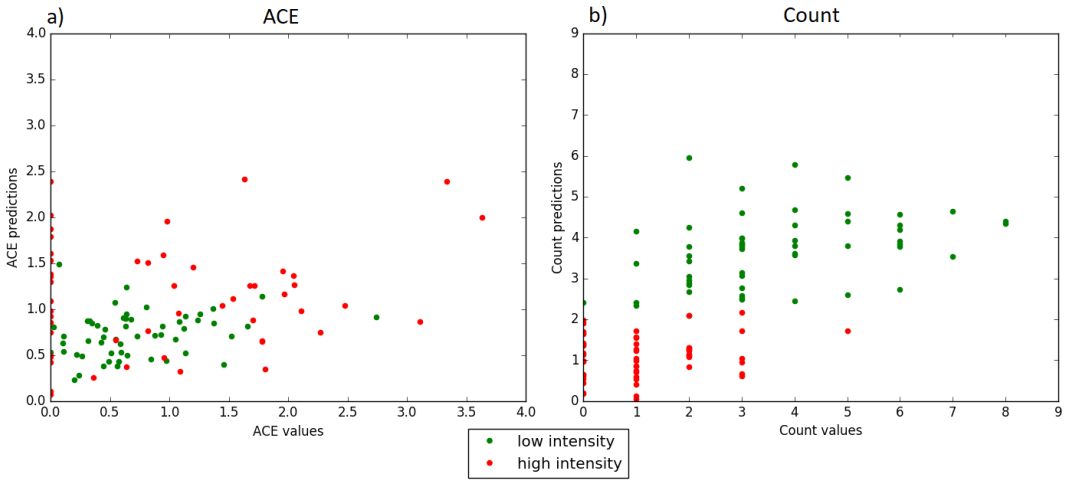


Fig. 3.22 Scatter plots of a) observed and predicted ACE-JJASO values and b) observed and predicted count-JJASO values for the low intensity (green dots) and high intensity (red dots) storms. ACE units 10^4 knots^2

datasets (count-JJASO and ACE-JJASO) are linearly detrended, the model skill is further decreased, so any (negligible) skill is partly due to this trend.

These results illustrate that although the correlation maps show strong significant correlations in this region explored, using just this SST in a simple regression model for predicting storm activity the following season (count-JJASO and ACE-JJASO) does not provide a skilful forecast.

3.5 Discussion

The extent to which this analysis is robust depends on the historic tropical cyclone track accuracy as well as the representation of large-scale variables. The tropical cyclone historic record has been shown to have trends (Vecchi and Knutson, 2011) and is limited by the changing observing system, which was especially limited further back in the historic record (section 2.6). Recent estimates of best track position errors are approximately 35 nm (~40 miles) for tropical storms, 25 nm for category 1 and 2 hurricanes, and 20 nm - 8 nm for major hurricanes (Landsea and Franklin, 2013; Torn and Snyder, 2012). The average uncertainty of intensity is estimated as 8-14 knots, with higher uncertainty with more intense storms (Landsea and Franklin, 2013; Torn and Snyder, 2012). The analysis was focussed on landfalling storms, and so it is hoped that most storms have been captured, as most recording errors occurred over the oceans. The results using ACE over the season was shown to have similar results to frequency and because of larger errors in storm intensity, the rest of the

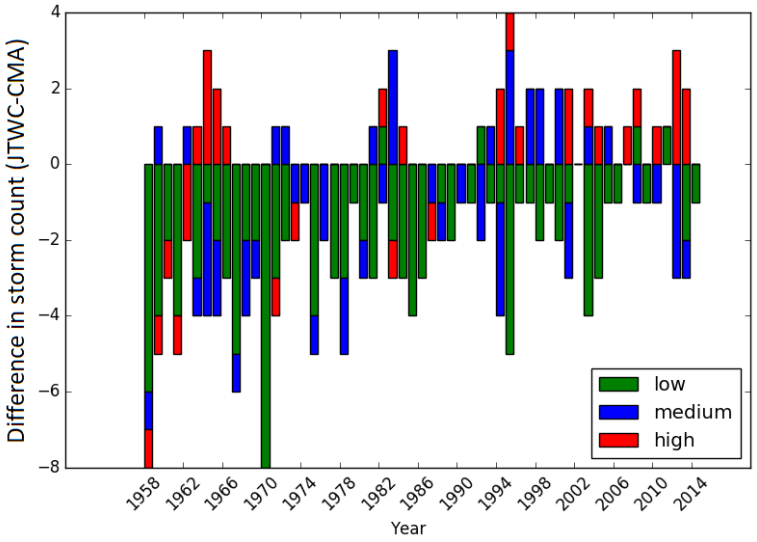


Fig. 3.23 Difference between Joint Typhoon Warning Center (JTWC) and China Meteorological Agency (CMA) of storm counts that intersected the domain during JJASO (1958-2014). Negative values when CMA>JTWC count and positive values when JTWC>CMA count.

analysis focussed on counts alone. However, intensity was used to divide the storms into low, medium and high intensity. Figure 3.23 shows the difference in counts of different category storms that intersected the domain between the JTWC record (used in this study) and the China Meteorological Agency (CMA) record. In the early period, there are generally more storms reported in the CMA data than JTWC. In more recent years, the total counts converge, although there remains a discrepancy with storm intensity classification.

A key difference between this study and relationships examined for statistical seasonal forecasts of tropical cyclone activity is the selection of a finite domain over which to analyse the storms. This approach provides the benefit of a more targeted forecast, however, limits the sample size of storms available. The low intensity storms totalled 204 over 57 years, with one year of zero count. For the medium and high intensity storms, there are 177 and 63, respectively, with 21 years of zero count for the intense storms. Having such a small sample of storms in each category over a 57 year period limits the effectiveness of any correlation and empirical modelling approach. The lack of skill of the model developed in section 3.4.3 using the SST in areas of high correlation, shows that even though robust relationships have been observed, they are not sufficient to create a forecast.

The possibility of decadal signals in this analysis was examined by sub-sampling the correlations into different PDO phases. Results showed that over these different periods of 18, 22 and 17 years (cold, warm, mixed), the signal was not consistent. The strong signal seen in the cold PDO phase is something to examine in future, as it suggests that the PDO

modulates the relationship with SST in the region with high correlation in JFM-1. To further examine these decadal signals requires many more decades, and as we are limited by the short tropical storm record (section 2.6), is best examined using GCMs.

The impact of ENSO on tropical cyclone activity in the west Pacific has been shown in observations and modelling studies (see section 2.3). In an El Niño year, the mean genesis location shifts eastward and the resultant storms are longer lived and can reach higher intensities than during a La Niña year (e.g. Camargo et al., 2007; Chan, 2007; Chan et al., 1998; Lander, 1994; Zhan et al., 2011). During El Niño, more storms recurve before landfall, with fewer across the Philippines and South China Sea (Liu and Chan, 2008; Wang and Chan, 2002), whereas in La Niña years, the storms generate further westwards and are straight moving, with increased landfalls observed in China (Camargo et al., 2007; Wang and Chan, 2002). In terms of total storm count, this signal is observed (figure 3.3h), with a large region of negative correlation in the central and eastern equatorial Pacific during the storm season, showing that when this SST is anomalously low (La Niña), there is greater landfall over the domain.

Empirical models generally include ENSO-related predictors (e.g. Chan et al., 1998; Zhan et al., 2012), highlighting the fact that it is an important mode of variability affecting tropical cyclone activity. Other predictors that are used in statistical forecast models include 500 hPa geopotential height over the Pacific and Australian region, convective activity over the WNP, vertical wind shear of zonal wind over the WNP and tropical eastern Pacific (Zhan et al., 2012), Australian monsoon and subtropical high in the South Pacific (CL Chan et al., 2001). These additional variables are all atmospheric, and have a strong influence on the genesis, track and lifetime of these storms (sections 2.2.2 & 2.3), but can only be used for forecasting at a lead time of a few months.

As well as affecting genesis principally through vertical wind shear and vorticity, the atmosphere controls the track of tropical cyclones (sections 2.2.2 & 2.3). In this study instead of examining basin-wide presence of tropical cyclones, only those intersecting a specified domain were examined, therefore steering is an important factor to consider. Unlike the ocean, which can provide a source of predictability, the atmosphere varies on much shorter time scales. There are various different modes of variability of different spatial and temporal scales that interact and modulate atmospheric steering of tropical cyclones. The PDO, which is a decadal mode of variability affects the subtropical high extension and intensity as well as the zonal winds (Liu and Chan, 2008), which are important to tropical cyclone movement (Chan and Gray, 1982) alongside large-scale steering flows related to the MJO (Kim et al., 2008). The monsoon trough is also an important control of tropical cyclone variability in the west Pacific (section 2.3), and when defined as the contiguous region where long-term (1988-

2010) mean July-November 850 hPa relative vorticity is positive, 73% of all July-November tropical cyclones form within it (Molinari and Vollaro, 2013). The atmosphere is important for tropical cyclone forecasts over a specific domain, but only have short-range predictability.

The main signal investigated in this study is the anti-correlation between the low intensity storms (figure 3.6a,b) and the high intensity storms (figure 3.6e,f) with SST in the JFM of the previous year ('JFM-1') seen off the east coast of mainland China, in the East China Sea and in the Bay of Bengal, and also in a horse-shoe shape to the east and north. The strong signal found with SST in JFM-1 around the coast of China and extending to the east and north (figure 3.6) was not as apparent in the JFM just before the storm season. During the season, the atmosphere also plays an important role in storm genesis, track and intensity (sections 2.2.2, 2.3), and ocean-atmosphere interactions can change the SST and dissipate the signal that was previously observed. The low intensity storms also have a large region of positive correlation in the eastern equatorial Pacific, suggesting that ~18 months after an El Niño event, there will be increased frequency of weak storms in the landfall domain and there is no signal for the other intensities. However, after the mature phase of an El Niño, tropical cyclone activity over the entire ocean basin tends to be below normal, whereas after a La Niña event, the entire basin generally has more tropical cyclones (Chan, 2000).

The maps of variables correlated with storm activity present the local significance, i.e. at each grid point, however, does not represent the significance given the overall spatial structure of the field. Spatial correlation is present in nearly all meteorological fields (Elmore et al., 2006) and 'field' or 'global' significance (Livezey and Chen, 1983) depends on spatial correlation, taking into account how variations at one grid point are reflected at other grid points due to physical processes covering areas larger than the grid spacing. The global null hypothesis is that all of the local null hypotheses are true, so that failure to reject the global null hypothesis implies that significant results have not been detected anywhere in the field of individual local tests (Livezey and Chen, 1983). Assuming statistical independence among the local test results is a best-case situation, as spatial correlation among the local grid point tests implies that even more local test rejections are required in order to achieve field significance. However, exactly how many local test rejections are required depends on the nature of the underlying spatial correlation, and this threshold may be difficult to determine in a particular multiple-testing setting (Wilks, 2016). In terms of confidence level, at the 5% confidence level, 5% of points in the domain showing statistical significance could have occurred by chance (Livezey and Chen, 1983). In figure 3.6, which shows the strong correlations for weak and strong storms with SST in JFM-1, approximately 7% of the SST area is significant for the high intensity storms, and 14% for the weak storms. If this simple threshold of field significance is applied to these maps, it suggests that the field is significant,

however, this has not taken into account the dependence among the grid point correlations, which would reduce the significance of the field.

A study by Lu et al. (2013) showed predictive skill for typhoon activity in a domain around Taiwan, and here the same empirical approach is used, but to explore the relationship with tropical cyclone activity around southern and central China. Whereas Lu et al. (2013) used predictors from March-May before the storm season, the aim of this study was to identify whether there exist any relationships during the previous year (up to 18 months beforehand). Although regions of SST in the previous JFM (JFM-1) were found to be significantly correlated with tropical cyclone activity in the following season (count-JJASO and ACE-JJASO), these signals were not sufficient to use for a statistical forecast. Due to the strong influence of the atmosphere mentioned previously, it is likely that, especially forecasting over a specified domain, the lead time of such a forecast is limited due to the chaotic nature of the atmosphere. It would be interesting to further explore the mechanisms for this strong correlation with SST in JFM-1, and a modelling experiment with a fully dynamical ocean model would be required, with a large sample size to further explore decadal variability.

3.6 Conclusions

This study has revealed a robust empirical signal relating SST ~18 months prior to the typhoon season activity in a domain around southern China. The frequency of low intensity storms within the domain of interest maintains a positive correlation with SST in the East China Sea and off the coast of Japan from JFM the year before the storm season (JFM-1) (figure 3.6), all the way through to the storm season ~18 months later (SST-JJASO) (figure 3.3). Although this signal is also present in the JFM a few months prior to the storm signal, the highest correlations are seen in the JFM of the previous year (JFM-1).

For the high intensity storms, during the storm season there is a significant positive relationship with SST in the northern North Pacific, which is part of the pattern that is related to El Niño. The relationship with El Niño and the spatial distribution of West Pacific tropical cyclones is well established (section 2.3), in that in a positive phase, there is greater landfall around Japan as storms recurve, and in a negative (La Niña), greater landfall in southern China (the domain of interest in this study). The previous JFM (JFM-1), the spatial distribution of significant correlations is similar to that for the low intensity storms, away from the eastern equatorial Pacific. In the Bay of Bengal, East China Sea and across into the mid-Pacific in a horseshoe-shape (red and purple boxes in figure 3.6), the opposite sign of correlation is apparent for the strong and weak storms.

This relationship between SST in JFM-1 and storm count in the domain was shown to have the strongest correlation during the early period examined, which relates to a cold PDO phase (figure 3.10). In this cold PDO phase, the large scale SST anomaly is warm in the central northern North Pacific, with a cold anomaly along the eastern side of the basin. The surface heat flux during this season (JFM-1) has significant correlations with storm activity in some similar locations as the SST, mainly in the horseshoe-shape region. For the low intensity storms, the heat flux leads the SST in this area north of approximately 30°N, but in the lower portion, the SST leads the heat flux. Across this entire region, heat flux leads the SST for the high intensity storms (atmosphere forcing ocean). In the mid-latitudes the atmosphere generally forces the ocean, but further equator-ward, the ocean primarily forces the atmosphere (section 2.2.1). The difference in forcing mechanism may be related to the large-scale SST and El Niño, which also shows a significant correlation with the low intensity storms.

There are many phenomena that influence tropical cyclone activity operating on a number of scales, such as interannual El Niño, decadal PDO, and sub-seasonal MJO. This study has shown that large-scale relationships with landfall over a specific domain can be established in the previous year, however, using these signals alone did not provide a skilful forecast.

Chapter 4

Variability of shear instability in an extra-tropical cyclone

Key findings: Mesoscale kinetic energy produced by shear production found in all model runs of an extra-tropical cyclone over the Gulf Stream, with a large spread between ensemble members.

4.1 Introduction

This chapter examines the shear production term in the mesoscale kinetic energy budget (equations 4.2 and 4.3) associated with an extra-tropical cyclone, and seeks to establish whether a feature proposed by Sheldon et al. (2017) in a single control experiment is apparent in a suite of other model simulations. This feature is related to the Gulf Stream, and Sheldon et al. (2017) suggested the 'warm path' as a mechanism for the interaction between the ocean and the atmosphere.

4.1.1 The Gulf Stream

Global atmospheric circulation is characterised by easterly trade winds in the Tropics and westerlies in the mid-latitudes (section 2.2.2). The atmosphere exerts a force on the ocean below, which is also affected by the rotation of the Earth (Coriolis effect), a factor which increases with proximity to the poles. Surface waters build up on the western side of ocean basins, resulting in the ocean-surface slope being steeper on the western side (versus eastern side), which leads to a faster geostrophic flow on that side; creating among the fastest surface currents in the ocean (Munk, 1950; Stommel, 1948). These currents extend much deeper than most other surface currents, and are deflected by the continental margins, which prevent these

currents from flowing onto the shallow continental shelves. These are known as western boundary currents (WBCs) and have typical widths of less than 100 km and surface speeds can exceed 2 ms^{-1} (Cronin et al., 2010). The Gulf Stream is a WBC in the North Atlantic and can be seen in the SST field, transporting warm water poleward and eastward (figure 4.1).

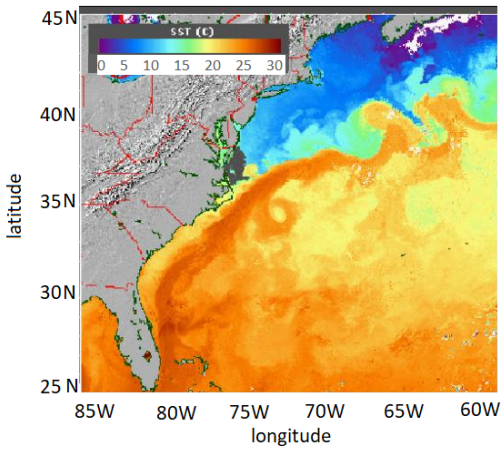


Fig. 4.1 The Gulf Stream, revealed through SST data, made from the AVHRR (Advanced Very High Resolution Radiometer) sensor carried on a NOAA satellite. Source: https://science.nasa.gov/earth-science/oceanography/physical-ocean/currents

On the northern edge, there is a strong SST gradient while to the south, eddies tend to erode this gradient. There is a strong deformation of the sea surface isotherms, bringing poleward and eastward a 'tongue' of warm water. This feature extends down to ~100 m, which is apparent in the vertical section (figure 4.2) as the closed isotherm at approximately 72°W (shown by purple arrow). This specific part of the Gulf Stream shall be referred to as the 'warm tongue' in the remainder of this work.

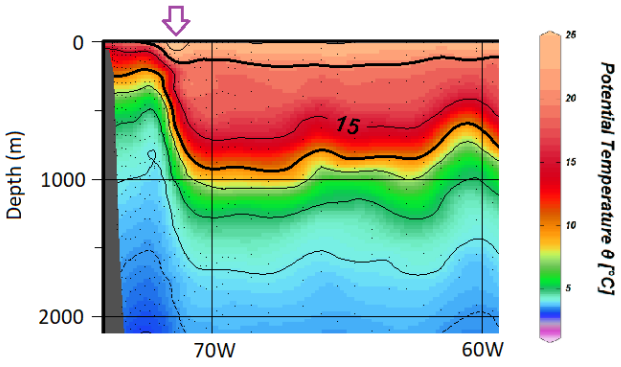


Fig. 4.2 Hydrographic section of potential temperature at 37°N. Purple arrow indicates location of warm tongue. Source: http://www.ewoce.org

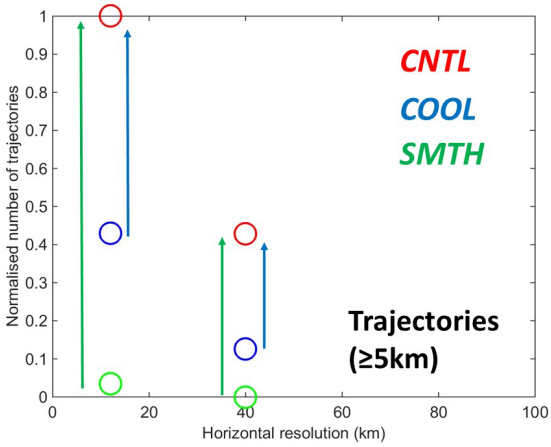


Fig. 4.3 Number of back trajectories (circles) with height 5km at t=24h and reaching low levels over the ocean at t=0h: red for CNTL, blue for COOL and green for SMTH. The arrows indicate a measure of oceanic forcing when comparing CNTL,SMTH or CNTL,COOL. Normalized such that the number for CNTL at 12km resolution is unity. Source: Sheldon et al. (2017)

It has been found that the growth of extra-tropical storms is enhanced in locations such as the Gulf Stream, where there are strong oceanic fronts that help to maintain the strong baroclinicity that is required to maintain them (sections 2.2.1 and 2.4).

4.1.2 The 'warm path'

Previous studies (Sheldon et al., 2017; Vannière et al., 2017a) have suggested a mechanism of oceanic forcing associated with the Gulf Stream warm tongue on the warm sector of cyclones. Here there are weak air-sea heat fluxes, which is in sharp contrast to what occurs in their cold sector. The mechanism consists of an intensification, and possibly a destabilisation, of the frontal circulation embedded in the cyclones.

In Sheldon et al. (2017), the 'warm path' mechanism has been examined using one case study on January 15th 2004, with a Met Office Unified Model (MetUM) simulation integrated for 72 hours. Atmospheric characteristics in an extra-tropical cyclone were analysed using a control SST ('CNTL'), a smoothed SST ('SMTH'), and a cool SST ('COOL'), where the SST everywhere was reduced by 3K. Results showed that the Gulf Stream has a significant impact on the upward motion present in the cyclone. Figure 4.3 shows oceanic forcing measured by the number of trajectories reaching 5 km in the atmosphere from low levels. It shows that at both model resolutions (12 km and 40 km), the control simulation has more than double the number of trajectories reaching 5 km than the perturbed simulations, with the smooth simulation having the fewest. This figure also shows that with higher resolution,

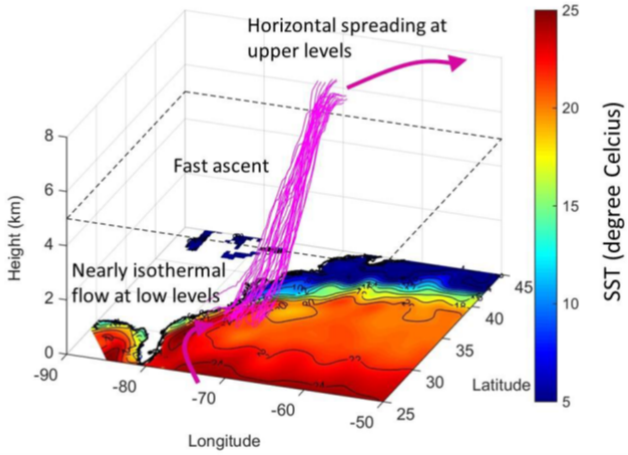


Fig. 4.4 Trajectories reaching upper levels flow along the contours of warm SST. Source: Sheldon et al. (2017)

approximately double the number of trajectories reach 5 km. The number of trajectories relates to the stability of the air mass, with greater instability found at mid-tropospheric levels with the control SST.

Thermodynamic and dynamic pathways have been proposed to explain these results. For the thermodynamic mechanism, trajectories in the CNTL experiment are parallel to the Gulf Stream, with no significant loss of heat and gain of moisture, maintaining high equivalent potential temperature (θe) (section 2.8.3) values (figure 4.4). In the SMTH simulation, air parcels cross SST contours, reducing θe and the likelihood of ascent. The dynamical considerations are that, due to stronger SST gradients in the control experiment, a thermally driven cell enhances the frontal circulation, increasing the feed into the warm conveyor belt (section 2.1). Also, it is possible that the stronger SST gradients destabilise the frontal circulation by enhancing the vertical wind shear (Sheldon et al., 2017).

Within the warm conveyor belt, there is production and destruction of potential vorticity (*PV*) due to latent heat release. The mean *PV* evolution within the warm conveyor belt increases from low levels to almost 1 potential vorticity unit (PVU) at 700 hPa as the heating rate increases, then decreases to less than 0.5 PVU at 300 hPa (Madonna et al., 2014), associated with a decreased heating rate. This therefore creates negative *PV* anomalies in the warm conveyor belt outflow region due to strong cross-isentropic ascent of warm conveyor belts to regions that are climatologically in the lower stratosphere (Madonna et al., 2014). The presence of negative *PV* in the cold sectors of extra-tropical storms due to strong surface heat flux has been demonstrated (e.g. Chagnon et al., 2013; Vannière et al., 2016). The strong updrafts within the cyclone can transport these parcels from the surface to upper

levels, creating a low *PV* anomaly. Finally, as *PV* increases with latitude and is adiabatically conserved, with a long slanted ascent within the cyclone, air from low latitudes can be deposited at upper levels and higher latitudes, thus also creating a low *PV* anomaly. The underlying oceanic features are important as a source of heat and moisture for the deep ascent within the extra-tropical cyclone. The effect of mesoscale SST features is strongest in the atmospheric boundary layer, but there is a deeper reaching response of the atmospheric circulation apparent in free tropospheric clouds (Bryan et al., 2010).

4.2 Research question

The result found by Sheldon et al. (2017) relied on a single simulation with a control SST set up. In this study, I address the question, given realistic SST set up, is this instability found in an ensemble of model runs? This will be investigated in ensemble forecast hindcasts with a resolution of 0.2°, which is comparable to the 12 km run in Sheldon et al. (2017). Sheldon et al. (2017) also found a significant decrease in this instability with decreasing model resolution, and I will also compare results to those from the coarser ERA-Interim reanalysis and an operational forecast (section 4.5.2). Analysis will use a mesoscale kinetic energy diagnostic (sections 2.8.5 & 4.4.1) to explore the activity on small scales. The storm studied by Sheldon et al. (2017) (15th January 2004) has been chosen as it has previously been used to show that the Gulf Stream is important in ascent within an extra-tropical cyclone.

4.2.1 Aims

- Analyse a ten member ensemble plus control using mesoscale diagnostics for an extra-tropical cyclone around 15th January 2004 over the Gulf Stream and compare to the result found by Sheldon et al. (2017)
- Compare results with coarser operational forecast and ERA-Interim reanalysis

4.3 Data

The data analysed has been produced by ECMWF. They include the ERA-Interim reanalysis (Dee et al., 2011), operational forecasts and ensemble forecast hindcasts, all of which are computed using the ECMWF Integrated Forecasting System (IFS).

4.3.1 ECMWF Integrated Forecasting System (IFS)

The ECMWF Integrated Forecasting System (IFS) consists of an atmospheric general circulation model (AGCM), an ocean general circulation model (OGCM), an ocean wave model, a land surface model, along with perturbation models for the data assimilation (EDA) and forecast (ENS) ensembles. It has a hydrostatic dynamical core and applies spectral transforms between grid-point space (where the physical parametrizations and advection are calculated) and spectral space (ECMWF, 2017). In March 2016, ECMWF launched a new model cycle, with a new grid comprising up to 904 million prediction points, three times as many as before (ECMWF, 2016). A new 'cubic-octahedral grid' pattern is now used and the number of waves used to represent the meteorological fields has been kept the same, while increasing the number of grid points used to represent each wavelength (ECMWF, 2016).

Table 4.1 Some available ECMWF products in 2017 configuration

Forecast (number of members)	Type	Days	Atmospheric horizontal resolution	Atmospheric vertical resolution	SST	Run times
High resolution (deterministic)	Operational	0-10	0.1° ~9 km	137 levels	OSTIA Persisted SSTs	0Z, 12Z
Ensemble (51) Ensemble (51)	Operational Operational	0-15 16-46	0.2° ~18 km 0.4° ~32 km	62 levels 91 levels	NEMO 0.25° NEMO 0.25°	0Z, 12Z Mon, Thurs
Ensemble (11) Ensemble (11)	Hindcast Hindcast	0-15 16-46	0.2° ~18 km 0.4° ~32 km	62 levels 62 levels	ERA-Interim ERA-Interim	Mon, Thurs Mon, Thurs
ERA-Interim *ERA5 (2008-present available)	Reanalysis Reanalysis	1979 - present 1950- present	0.75° ~79 km 0.25° ~25 km	60 levels 137 levels	various	ongoing

Table 4.2 Operational forecast resolution. *The operational model in 2004 is used in this analysis.

Date	Grid	Horizontal resolution
*21.11.00	N256	0.4° ~40 km
01.02.06	N400	0.225° ~25 km
26.01.10	N640	0.125° ~16 km
08.03.16	O1280	0.1° ~9 km

4.3.2 Operational forecast

The operational forecast consists of 52 individual members; an ensemble of 50 members plus a control, and a higher resolution deterministic forecast (table 4.1). The model resolution is updated every ~6 years (table 4.2). In March 2016, along with the new cubic-octahedral grid type, the horizontal grid spacing was reduced from 16 km to 9 km, with the ensemble forecasts run at double this resolution. Up until February 2006, the model was run with 60 vertical levels (up to 0.1 hPa) and 40 levels (up to 10 hPa) for the ensemble. From February 2006 until June 2013, the model had 91 levels (up to 0.01 hPa) and 62 (up to 0.1 hPa) in the ensemble. Thereafter, there are 137 and 91 levels (both up to 0.01 hPa) in the deterministic simulation and ensembles, respectively.

Deterministic

A deterministic forecast provides a single realisation of the future state of the atmosphere, i.e. a control forecast, and is currently being run at 0.1° resolution (tables 4.1, 4.2). In June 2018, ECMWF upgraded their forecast system, making the forecasts more seamless, by adding coupling to these high-resolution deterministic forecasts. Previously, SSTs came from Operational Sea Surface Temperature and Sea Ice Analysis (OSTIA), a high resolution analysis of the SST and sea ice concentration for the global ocean with daily, global coverage at 1/20° resolution (~6 km), which is generated in near real time (Donlon et al., 2012). Prior to June 2018, coupling had only been applied in ensemble forecasts, extended-range forecasts and seasonal forecasts.

Ensemble

Poor forecasts result from errors in initial conditions and model formulation, with initial conditions dominating during the first five days or so. In sensitive parts of the atmosphere, such as baroclinic systems, errors amplify most easily and can move downstream and affect the large-scale flow. To characterise the uncertainty in this evolution, small changes to the

4D-Var analysis (data assimilation) are made, creating an ensemble of different, perturbed initial states, which are run at half the deterministic resolution (table 4.1). A small spread in the ensemble represents a predictable state, whereas large divergence suggests an uncertain forecast. These ensembles are particularly important for extreme events, where probabilities of breaching thresholds is important. With respect to synoptic patterns, the control ensemble forecast gives a similar performance to the deterministic forecast (Persson, 2015), which is at twice the resolution. However, the deterministic forecast is better at forecasting small-scale extreme events, for example strong winds and heavy rain, when resolution is more important.

4.3.3 Ensemble hindcast

A hindcast, or reforecast is a model forecast run initialised with conditions in the past. The hindcast run commences every Monday and Thursday, for that day for the past 20 years (to 1996). Over a year, with a model run on every Monday and Thursday, an entire 20 year period with 10 ensembles members plus the control will have been created. The resolution of all of the members decreases at day 16, and the initial few days of the hindcast are analysed in this study, with a resolution of 0.2° (table 4.1). The ensemble members have five different ocean temperature analyses, with members 1 and 6, 2 and 7, 3 and 8, 4 and 9, 5 and 10 sharing the same initial state. These perturbed states are produced by adding randomly chosen wind perturbations to the ocean data assimilation, driven by five slightly different meteorological fields based on the control analysis. The SSTs in these hindcasts are partially coupled, using tendency from OSTIA. The forecast is taken from a run on 12th January 2017 using the 2004 initialisation (figure 4.5). The model initialisation is 2 days earlier than the Met Office experiment (Sheldon et al., 2017), but the same storm on 15th January is analysed.

4.3.4 Reanalyses

Reanalyses are often used as observations as they give global coverage and consistent spatial and temporal resolution, using a stable model and assimilating observations. ERA-Interim is a global atmospheric reanalysis with data starting in 1979, continuously updated in real time. The spatial resolution of the dataset is approximately 0.75°, 79 km (T255 spectral) on 60 vertical levels from the surface up to 0.1 hPa (Dee et al., 2011) and at 6-hourly temporal resolution (table 4.1). ERA5 is a new reanalysis produced by ECMWF, with finer spatial and temporal resolution, but data prior to 2008 has not yet been released and so the 2004 storm will not be examined using this dataset. These are both atmosphere-only reanalyses, with details of the SST products used in ERA-Interim presented in table 5.3.

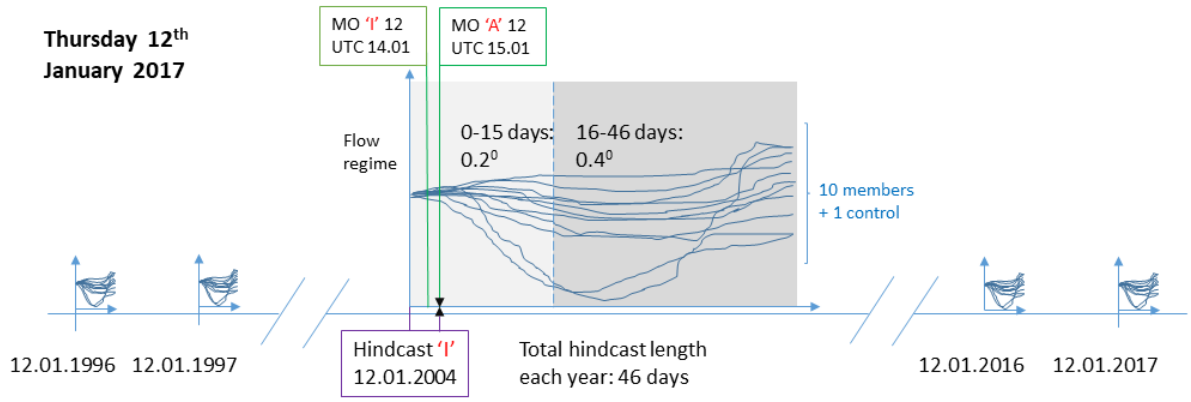


Fig. 4.5 The ECMWF hindcast schedule on 12th January 2017. 20 hindcast years (back to 1996) is run. Each ensemble is made up of 10 members plus 1 control, which reduce in resolution at day 15 and run for a total of 46 days. 'MO' is the Met Office experiment, 'I' is initialisation and 'A' is analysis.

4.4 Method

We examine characteristics within the storm rather than on the synoptic scale, analysing mesoscale instability using the diagnostics presented in the following section.

4.4.1 Mesoscale diagnostics

Turbulent eddies cascade energy toward the smallest scales, where it is dissipated by viscous diffusion, and so for turbulent kinetic energy (TKE) to remain constant, there must be continuing production of turbulence (Holton, 2004). In an environment where the lapse rate is unstable, the turbulence is convectively driven, whereas if it is stable, instability associated with wind shear generates the turbulence. Turbulence generated mechanically by dynamical instability due to wind shear can occur in both statically stable and unstable boundary layers (Holton, 2004). This shear production represents conversion of energy between mean flow and turbulent fluctuations and is proportional to the shear in the mean flow. This term is positive when the momentum flux is down the gradient of the mean momentum. This mechanical (shear) production can only occur if it can overcome the damping effect of stability and viscous dissipation, if in a statically stable environment.

To analyse spatial scales of a 100 km or less, which we broadly refer to in the following as 'mesoscale', we focus on the high-pass filtered horizontal kinetic energy, hereafter referred to as mesoscale kinetic energy or MKE, defined as:

$$MKE = \frac{\overline{u'^2 + v'^2}}{2} \tag{4.1}$$

In this equation, the overline indicates a (coarse) spatial average and the primes departures from it, while (u, v) are the horizontal component of the velocity vector. MKE obeys an equation of the form Gaspar et al. (1990):

$$\frac{\partial}{\partial t} MKE = \text{Shear production} + \text{Buoyancy production} + ... \tag{4.2}$$

where, in pressure coordinates,

$$\text{Shear production} = -\left(\overline{\omega' u'} . \frac{\partial \overline{u}}{\partial p} + \overline{\omega' v'} . \frac{\partial \overline{v}}{\partial p} \right) \tag{4.3}$$

and

$$\text{Buoyancy production} = -\overline{\omega' \alpha'} \tag{4.4}$$

The variables u, v and ω are zonal, meridional and vertical winds, α is specific volume and p is pressure. The additional terms in equation 4.2 include redistribution by transport and frictional dissipation.

A spatial low pass and high pass filter was applied to the original data to obtain the small scale 'prime' (ω', u', v') and mean 'bar' ($\overline{\omega}$, $\overline{u}$, $\overline{v}$) values. The high pass, to capture the high frequency variability, was calculated by subtracting the low pass from the original field. This is to separate the low frequency background from the high frequency perturbations and to examine small scale has an effect on the large scale. For shear production, the covariance of small-scale vertical motions (ω') and horizontal motions (u' or v') is calculated and then the product with the vertical shear of low pass winds ($\overline{u}$ or $\overline{v}$) is created and the instability in the x (u) and y (v) directions are combined. The buoyancy production term is calculated using specific volume (α), defined using density from temperature. The spatial filter was applied over ~2.8° (~300 km) (table 4.3), and the production terms are analysed at 500 hPa, which are comparable to the ~240 km filter and 4.5 km level used in the Met Office analysis (Sheldon et al., 2017).

To provide an idea of magnitude, we ask, for a perturbation to grow from 0 to 10 ms^{-1} in one day by shear production, what is the magnitude required?

$$MKE = \frac{\overline{10^2 + 10^2}}{2} = 100 Jkg^{-1} \tag{4.5}$$

$$\text{Shear production} = \frac{100 Jkg^{-1}}{10^5 seconds} = 1 mW kg^{-1} \tag{4.6}$$

Therefore, according to this simplified theoretical argument, 1 mWkg^{-1} of shear production is required to increase MKE from 0 to 10 ms^{-1} in one day. The rate of increase of wind speed generally occurs at faster speeds, for example 0 to 10 ms^{-1} in 6 hours, but this also involves baroclinic instability, deriving energy from the temperature gradient, and not the shear alone.

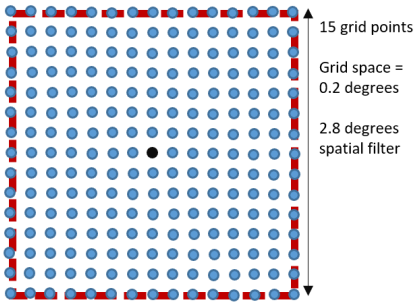


Fig. 4.6 Domain used to create the low pass for the hindcast data. The hindcast data is at 0.2° resolution and so 15 grid points were used, to give a 2.8° spatial filter. At each grid point, all values within this domain are averaged to create the low pass at that point.

Table 4.3 Low pass filter dimensions for ensemble hindcast, ERA-Interim and operational forecast

Product	Horizontal resolution	Number of grid points	Low pass scale
Ensemble hindcast	0.2°	15	2.8°
ERA-Interim	0.75°	5	3°
Operational forecast (2004)	0.4°	7	2.4°

ERA-Interim data (0.75°) was downloaded on 12 levels (200, 300, 400, 500, 600, 700, 800, 850, 875, 900, 925, 950 hPa), with 6 hourly time steps. In 2004, the operational deterministic forecast was run at 0.4° with 6 hourly time steps, and only 7 levels are available (200, 300, 400, 500, 700, 850, 925 hPa). These same 7 levels were used for the ensemble forecast hindcast, and in both of these datasets, the missing 5 levels were interpolated. An ensemble forecast hindcast dataset that was initialised on 12th January 2017 and set up with 12th January 2004 conditions was used. The operational forecast was also initialised at 00UTC 12th January. The vertical velocity data (ω, Pas^{-1}) is only complete at 12 hourly time steps for the hindcast and so the shear production term could only be computed at 00 and 12 UTC. The variables are instantaneous, defined as from the last model time step, which is between 15 and 30 minutes depending on the model run (P. Dando, personal communication).

The operational ensemble was not used, as this was at (0.8°) and the previous study (Sheldon et al., 2017) suggested this may be too coarse to resolve the instability. Other variables including precipitation and mean sea level pressure were also examined.

4.5 Results

Results are first presented for the hindcast control and 10 ensemble members (section 4.5.1), and comparison with the deterministic forecast and ERA-Interim is in the following section (4.5.2).

The shear production at 4.5 km and SST from the Met Office experiments at 12UTC 15th January are presented in figure 4.7. Both simulations are run at 12 km resolution and the spatial filter used 10 points in each direction (i.e. 21 points total), creating average over 240 km. There is a region of shear production in the SMTH run in the same location as seen in the CNTL run, although this is approximately five times weaker.

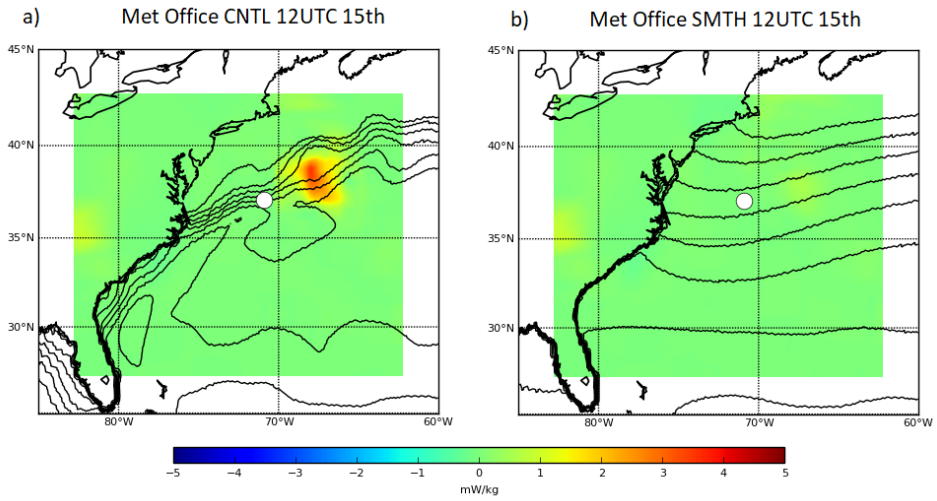


Fig. 4.7 Shear production at 4.5 km (coloured contours) and SST (black contour lines) every 2°C at 12UTC 15th January 2004 in the Met Office a) CNTL and b) SMTH experiments. White dot is location of low pressure centre.

4.5.1 Ensemble hindcast

The shear production and SST for the hindcast control and 10 ensemble members at 12UTC 15th January are shown in figure 4.8, with pairs starting with the same initial SST shown in matching coloured labels.

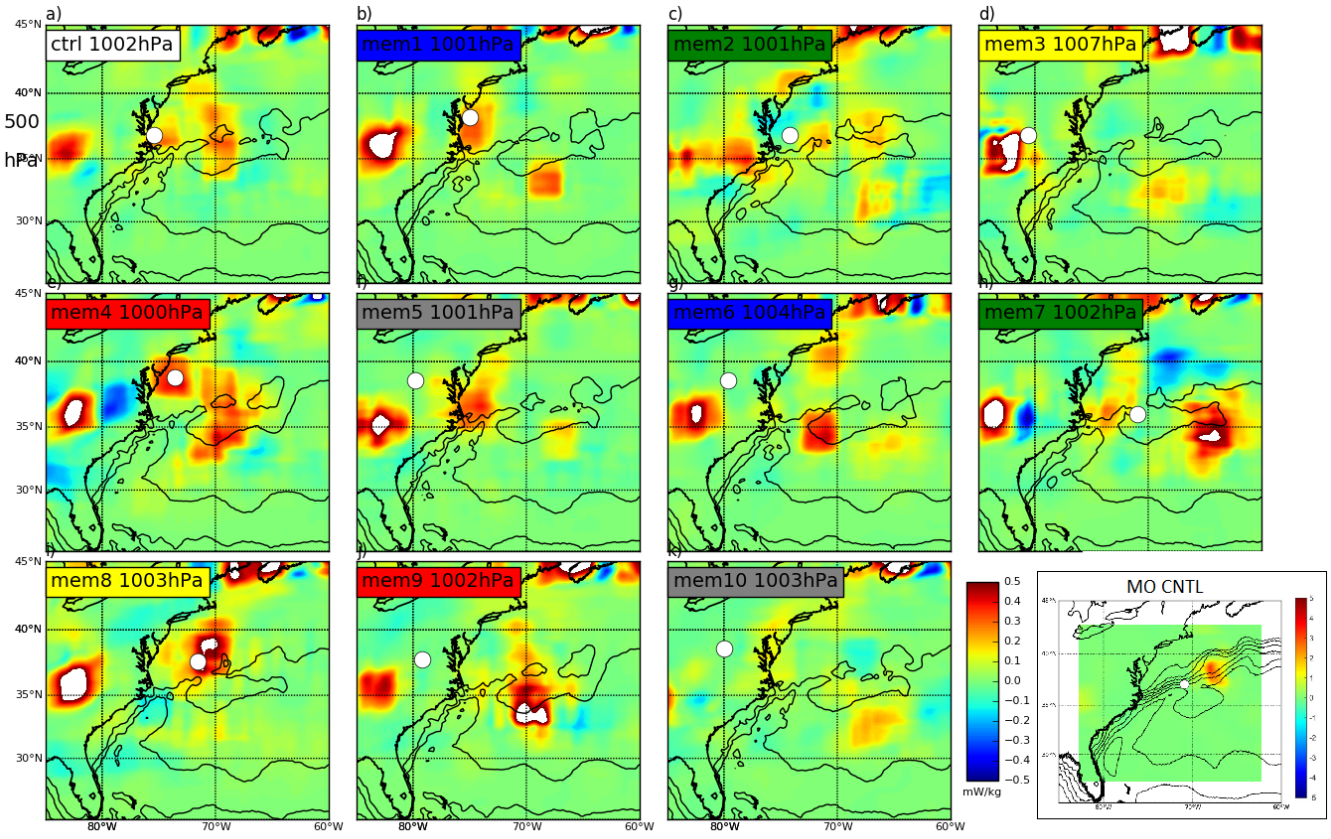


Fig. 4.8 Shear production at 500 hPa (coloured contours) and SST (black contour lines) every 2°C between 20°C and 30°C in the hindcast control and 10 ensemble members at 12UTC 15th January. The member name and minimum sea level pressure are given for each plot. Members that were initialised with the same SST share the same colour label. Low pressure centre marked by white dot. The result for the Met Office control run (MO CNTL) at 12UTC 15th January is repeated for comparison (units mW/kg).

At this time, the Met Office run is +24 hours after initialisation, whilst the hindcast is +84 hours. The SSTs between the pairs have started to diverge, however, all members have a similar warm tongue, with the 22°C isotherm reaching 35°N, comparable to the Met Office CNTL. The location of the low pressure centre varies between the members by up to ~10° and have values of between 1001 and 1007 hPa. All of the runs have regions of shear production, but with differences in location and intensity. Member 9 has a maximum shear production of ~0.6 mWkg^{-1}, whereas member 10 reaches only ~0.2 mWkg^{-1}. The intensity in all of the members is close to or less than that in the SMTH experiment (figure 4.7) by up to ~70%, but ~10 times less than in the CNTL experiment.

In the north of the domain, shear production associated with a preceding storm can be seen. Excluding this region, the distribution of shear production in these 10 ensemble

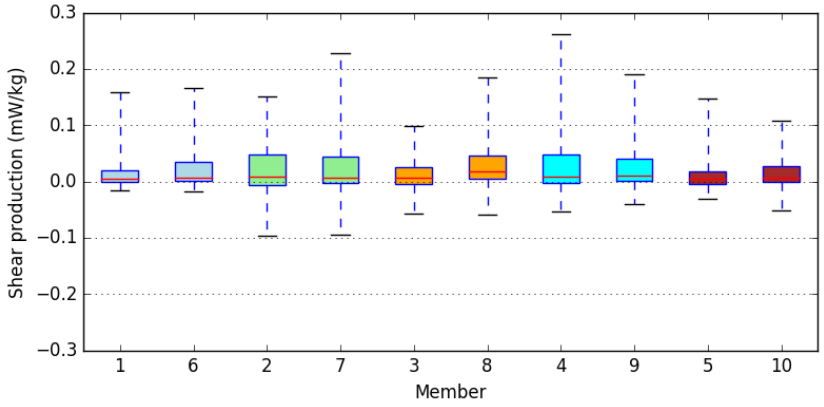


Fig. 4.9 Distribution of shear production over the ocean (land masked) at 500 hPa at 12UTC 15th between 25-42°N, 85-60°W. The box extends from the lower to upper quartile values of the data, with a red horizontal line at the median. The whiskers reach from 5th to 95th percentile. Outlier points are not shown.

members at 12UTC 15th January in the domain 25-42°N, 85-60°W is compared (figure 4.9). In all members, the median (red lines) are positive, with little or none of the inter-quartile range (box) in the negative range. The whiskers extend from the 5th to 95th percentile and the latter has a range of values from 0.097 in member 3, to 0.26 for member 4. This figure does not show a clear relationship between initial SST and shear production within the domain.

Comparison of the location of minimum sea level pressure (white dots) in figure 4.8 with those in figure 4.7 shows that most of the storms in the hindcast runs have not progressed as far east as in the Met Office simulations. Results at the following time step (+12 hours) are shown in figure 4.10 and the storms have deepened and moved east in all members and the control. The regions of shear production have also moved and intensified, with values more similar to the SMTH Met Office run in all members.

The spread between ensemble members at both of these time steps is further examined in figure 4.11. The 95th percentile of shear production within the domain 25-42°N, 85-60°W is plotted for each member of the hindcast ensemble, along with that of the smooth and control Met Office runs. The difference between the 95th percentile in the Met Office 'CNTL' and 'SMTH' runs is a factor of ~3.6 and although the absolute difference between the ensemble members is much smaller, the relative difference between the largest and smallest is a factor ~2.6, increasing to ~4.4, 12 hours later. At both time steps, the ensemble members are relatively evenly spread, with the control approximately centred within the ensemble.

Figure 4.12 shows the shear production and mean sea level pressure contours at 00 UTC on 17th January (+120 hours) in the hindcast control and 10 ensemble members. At this stage the members have diverged further, with large differences in shear production, storm

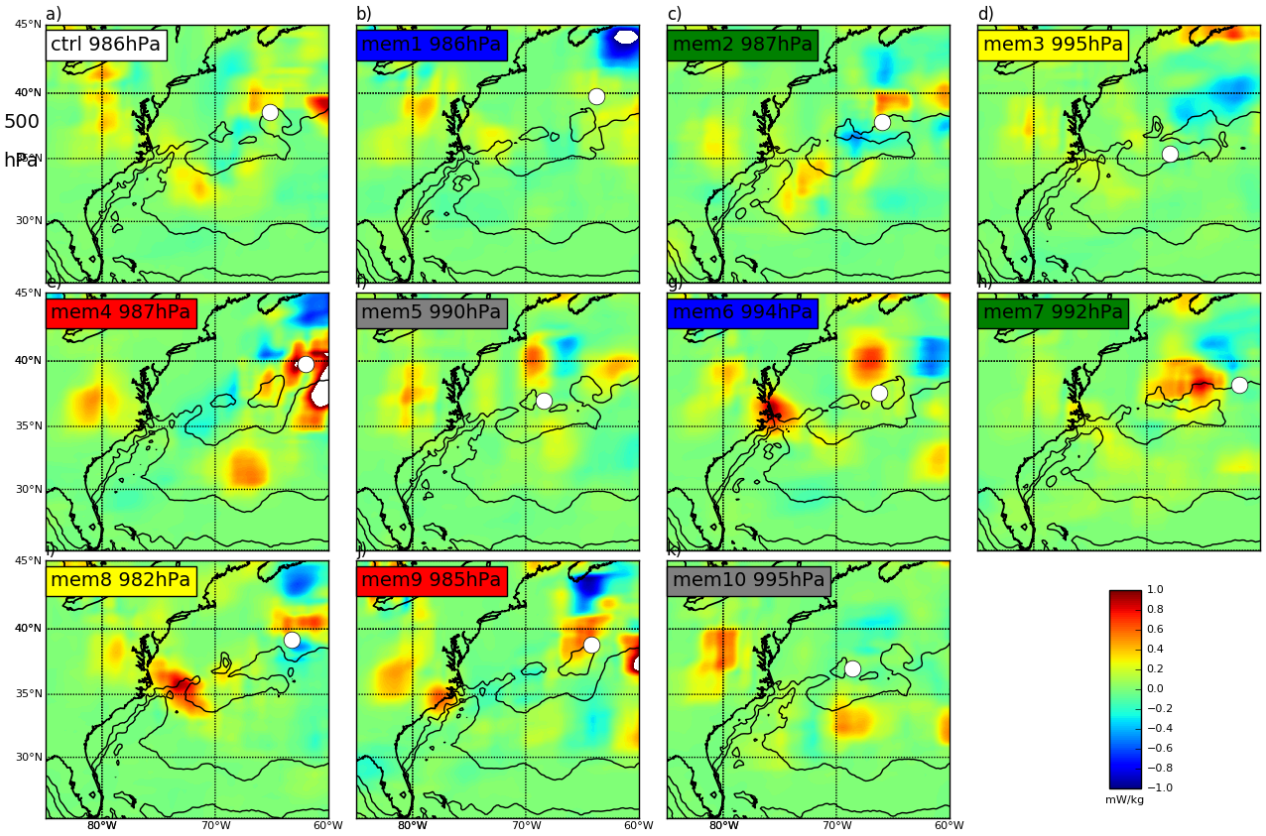


Fig. 4.10 Shear production at 500 hPa (coloured contours) and SST (black contour lines) every 2°C between 20°C and 30°C in the hindcast control and 10 ensemble members at 00UTC 16th January. The member name and minimum sea level pressure are given for each plot. Members that were initialised with the same SST share the same colour label. Low pressure centre marked by white dot.

position and intensity. The minimum mean sea level pressure values range from 975 hPa in member 10 to 937 hPa in member 5, which started with the same initial SST field.

The following section focusses on ensemble member 9, as this run exhibits relatively strong shear production, which is aligned in such a way that makes it a good candidate for cross-section analysis. Figure 4.13 shows the evolution of ensemble member 9 from 00UTC 16th January, with 12-hourly time steps. From the first time step to the second, the storm deepens and the shear production approximately doubles in intensity, and 12 hours later, the regions of shear production form more coherent strands. The shear production follows regions of strong gradient in potential temperature, marking cold and warm fronts (figure 4.13d,e,f). Moist air is present in the warm sector and the cold air advected in behind the cold front is relatively dry. The precipitation is intense in the low pressure centre and along

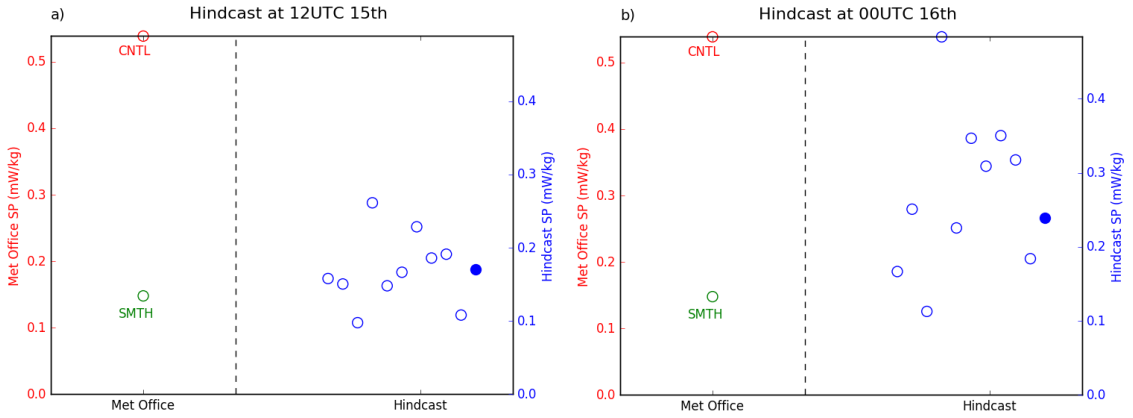


Fig. 4.11 Shear production 95th percentile for the Met Office CNTL and SMTH experiments at 12UTC 15th and the hindcast control and members at a) 12UTC 15th and b) 00 UTC 16th. Filled blue dot is the hindcast ensemble control.

the front, especially the trailing cold front, where sinking cold air is forcing the moist, warm air to ascend (figure 4.13g,h,i).

Figure 4.14 shows vertical cross sections across the cold and warm fronts at 00UTC on the 17th January. The wind bars are calculated by taking the horizontal wind speed (ms^{-1}) at this single time step and integrating this for an hour, showing where the original air parcel would be after an hour of moving at constant velocity. Both cross sections are taken across the front, and so meridional winds are plotted on a latitudinal plane. The coloured contours show relative humidity and white contour lines show potential temperature. Original data are on levels 200, 300, 400, 500, 700, 850, 925 hPa, with contour lines and filled contours interpolated by the plotting code. The top line plot shows shear production at 500 hPa and 12 hourly precipitation centred on the time step. The right hand line plot shows the vertical distribution of shear production averaged across the domain (solid red line) and the absolute shear production (dashed red line). A section at 58°W (figure 4.14a) intersects the cold front at approximately 38°N at 500 hPa (marked by grey circle). The isentropes (white contour lines) show cold air intruding from high latitudes to low latitudes with relative humidity of approximately 60%. The peak in precipitation as well as shear production at 500 hPa are associated with the frontal region. The vertical distribution of shear production peaks around the mid-troposphere. The transect taken at 45°W bisects the warm front at 58°N at 500 hPa (figure 4.14b). The warm front can be seen by the dip in the isentropes and high relative humidity. The wind bars show vertical motion throughout the depth of the troposphere associated with a region of high relative humidity. To the right of this plot is the storm centre, a large region of saturated air rising in the low pressure centre, with deep ascent up to at least

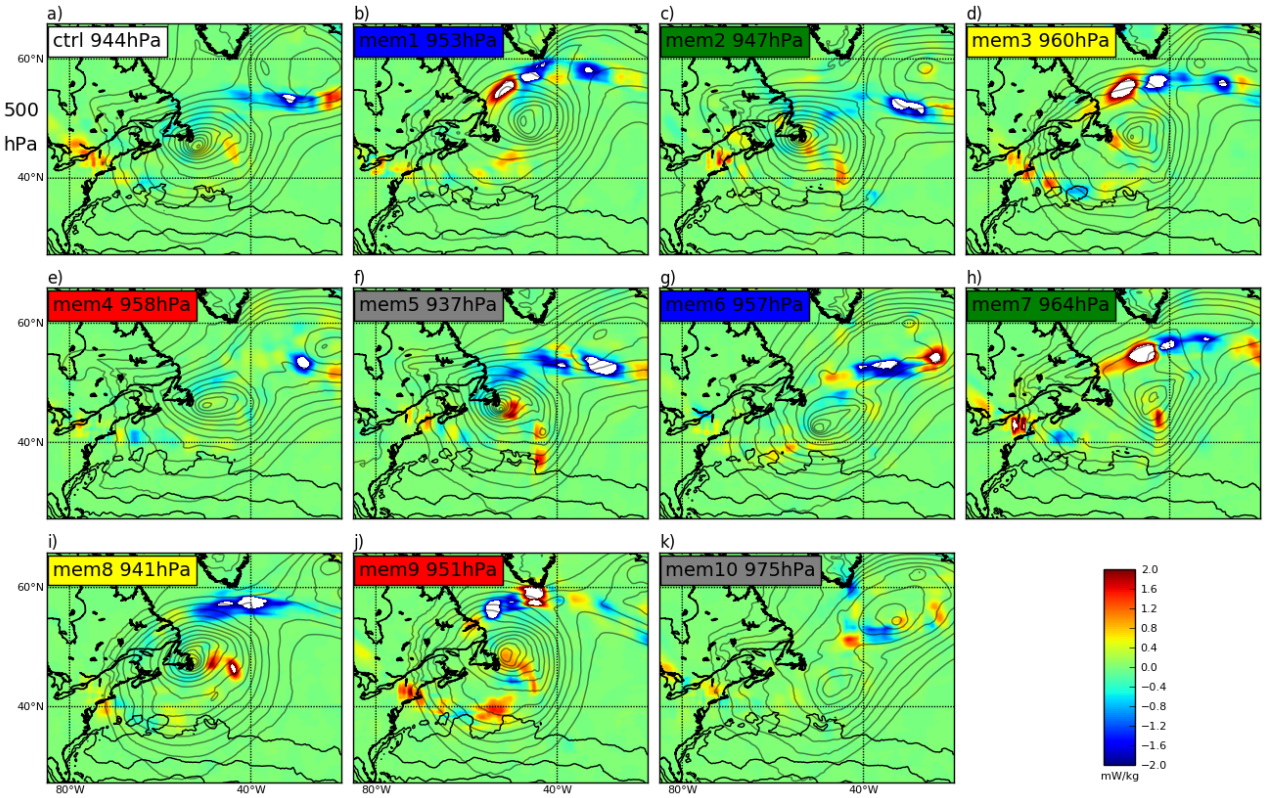


Fig. 4.12 Shear production at 500 hPa (coloured contours), SST (black contour lines) every 2°C between 20°C and 30°C and mean sea level pressure every 5 hPa from 900 to 1020 hPa in the hindcast control and 10 ensemble members at 00UTC 17th January. The member name and minimum sea level pressure are given for each plot. Members that were initialised with the same SST share the same colour label.

300 hPa. However, there is no shear production associated with this region, as it is confined to the frontal area. Comparison of the cold and warm front show steeper isentropes at the cold front, which is expected in the canonical extra-tropical cyclone structure (section 2.1). This figure also suggests that shear production is stronger along the warm front, which is also shown by all ensemble members at 00UTC 17th January (figure 4.12).

4.5.2 Operational forecast and ERA-Interim

Shear production in the coarser operational deterministic forecast and ERA-Interim is calculated at 6-hourly time steps and is shown in figure 4.15. The ‘bar’ term in equation 4.3 was set to cover the same area as in the hindcasts, using 5 and 7 grid points, but because of the coarser resolution in ERA-Interim and the forecast, the ‘prime’ term now represents at most scales of 0.75° and 0.4°, respectively.

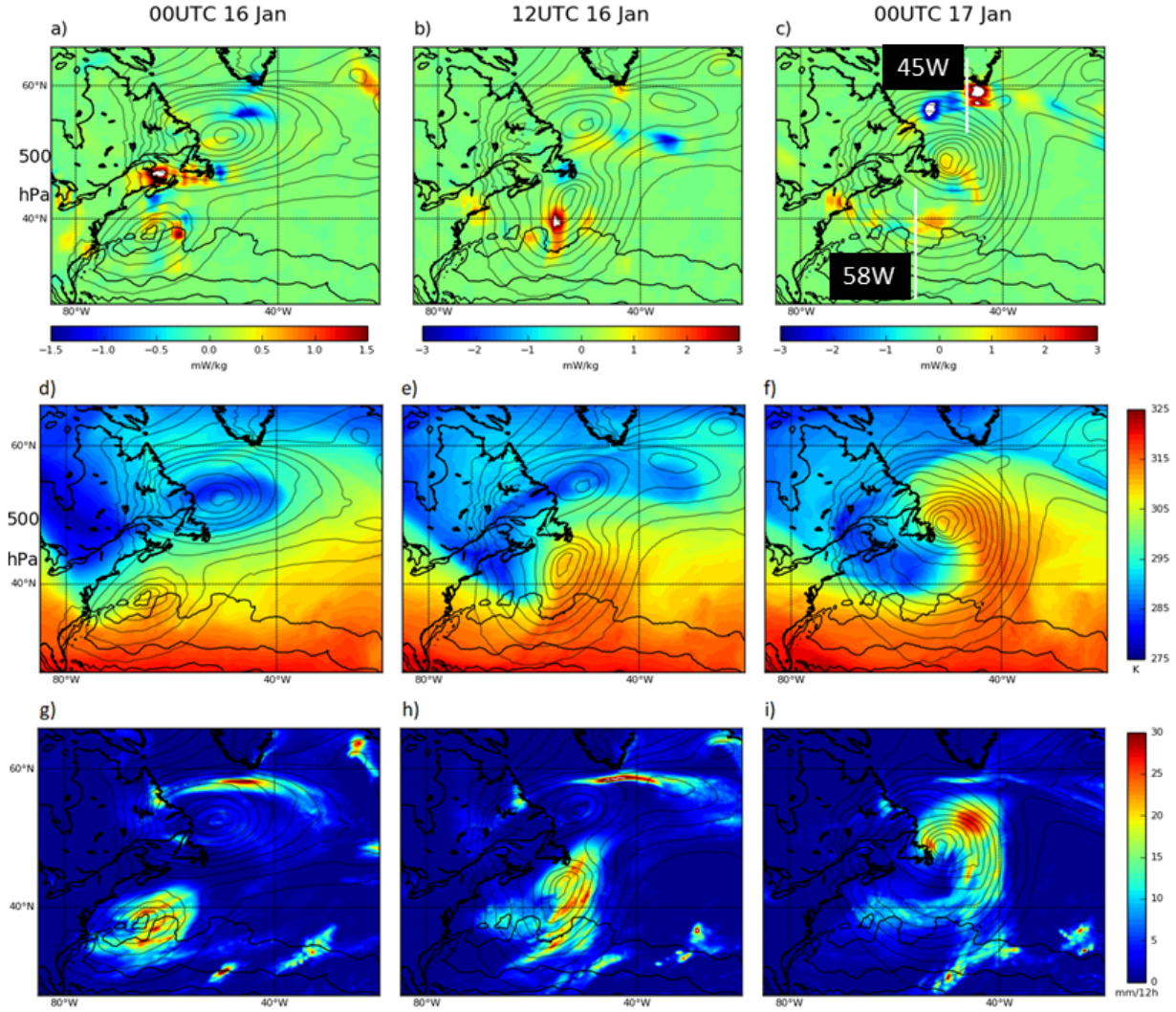


Fig. 4.13 Ensemble member 9 at a,d,e) 00UTC 16th, b,e,h) 12UTC 16th, c,f,i) 00UTC 17th. Top panel shows shear production at 500 hPa (coloured contours). Middle panel shows potential temperature at 500 hPa (coloured contours). Bottom panel shows 12 hour precipitation accumulation, centred on time step. All panels show SST (black contour lines) and mean sea level pressure (grey contour lines).

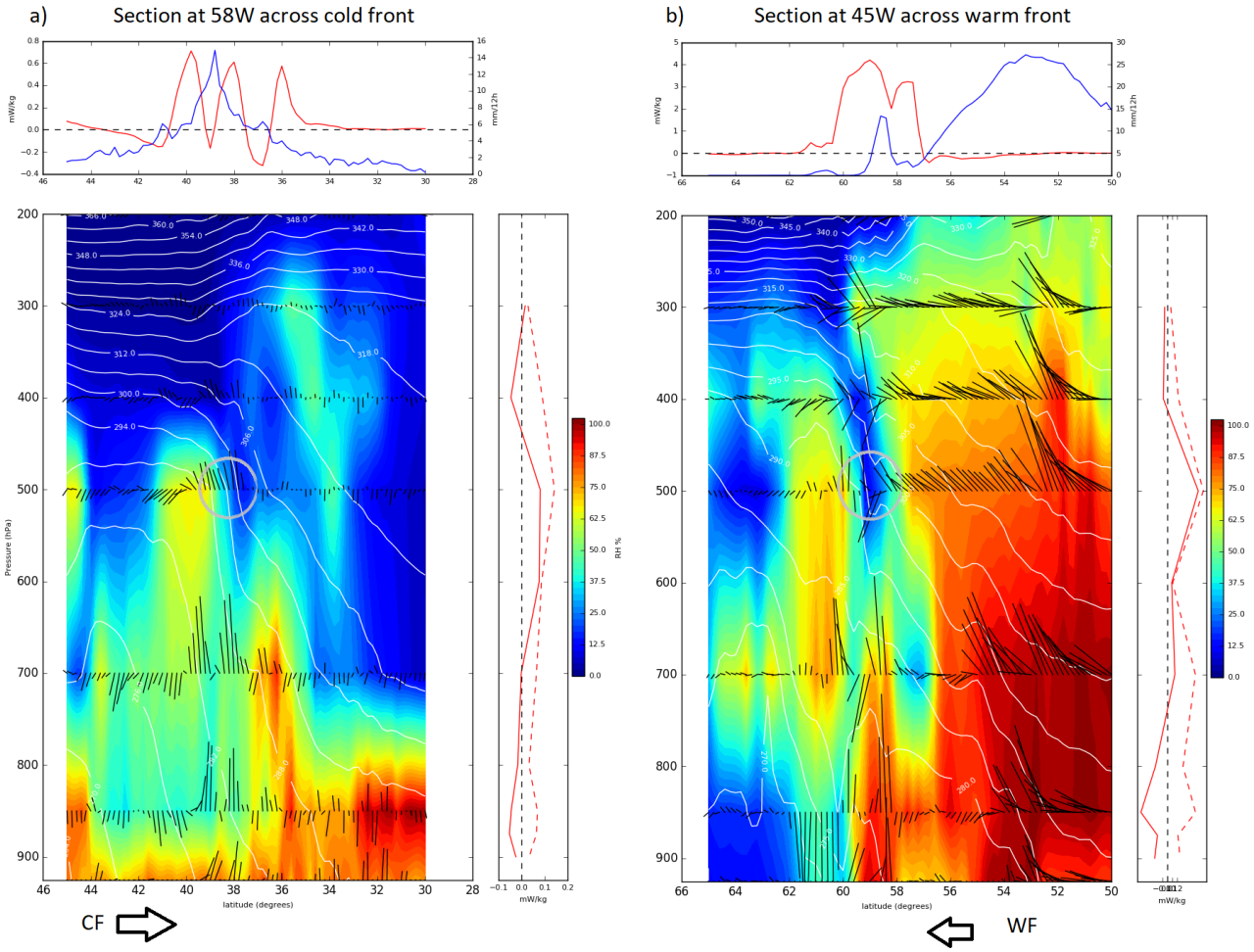


Fig. 4.14 Ensemble member 9 vertical cross-sections at 00 UTC 17th at a) 58°W and b) 45°W. Relative humidity is shown in filled contours and isentropes are shown in white contour lines. Wind bars are calculated using meridional (v) and vertical (ω) winds. The grey circles mark the fronts at 500 hPa. 'CF' and 'WF' mark the cold and warm fronts and the arrows, their direction of movement. The horizontal line plots show the shear diagnostic at 500 hPa in red and 12-hourly precipitation (mm) in blue. The vertical line plots show the mean shear production (solid red) and mean absolute shear production (dashed red).

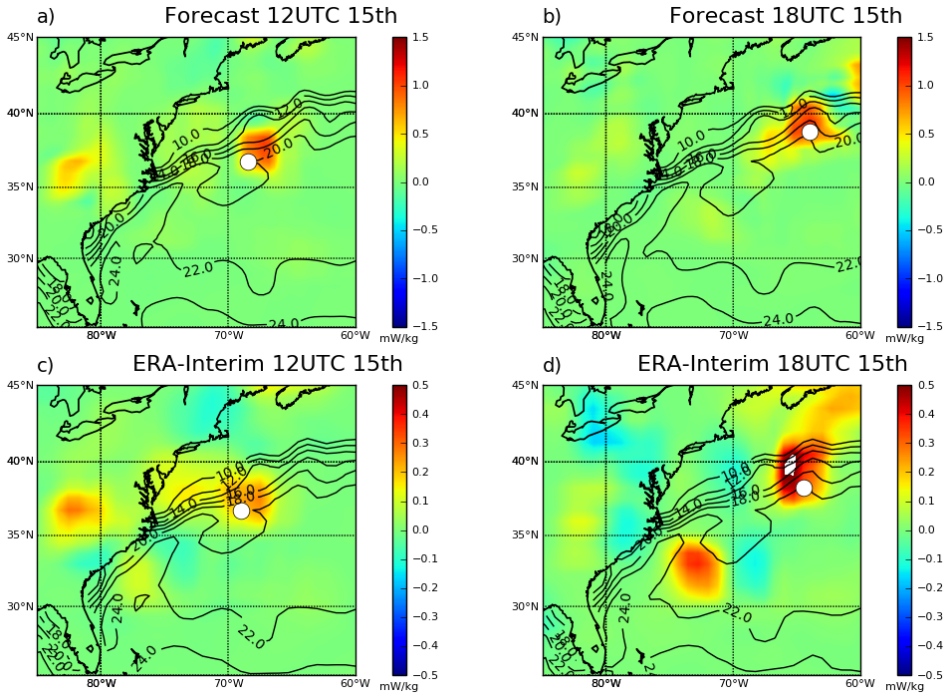


Fig. 4.15 Shear production at 500 hPa (coloured contours) and SST (black contour lines) every 2°C between 20°C and 30°C for a,b) forecast (0.4°) and c,d) ERA-Interim (0.75°) at a,c) 12UTC and b,d) 18UTC 15th January 2004. Low pressure centre marked by white dot.

In the deterministic forecast (figure 4.15a,b), the magnitude of shear production is ~2-3 times larger than that found in the hindcasts, despite a coarser resolution (note different scales used). The shear production seen in ERA-Interim (figure 4.15c,d) is on the same scale as the hindcast ensemble (figure 4.8), with the first time step comparable to the weakest members and the second more in line with the strongest members. The cyclones in both of these datasets show the same evolution as the hindcast runs, moving north-eastwards as they deepen, with shear production aligned along the warm and cold fronts. The SST fields in both of these models comes from the NCEP analysis.

4.5.3 Summary comparison of all datasets

The shear production (95th percentile and median) within the domain 25-42°N and 85-60°W in all model runs is plotted against the mesoscale kinetic energy (MKE) (95th percentile and median), for which it is a production term (equation 4.2, figure 4.16). In both plots, two time steps are shown for the ensemble hindcast (12UTC 15th, 00UTC 16th), 3 times are shown for ERA-Interim and the forecast (FC) (12UTC 15th, 18UTC 15th, 00UTC 16th), and the only available time step is shown for the Met Office simulations (CNTL and SMTH) (12UTC 15th). These additional time steps are shown as the storm timing in the datasets from this analysis does not exactly match that from the Met Office runs.

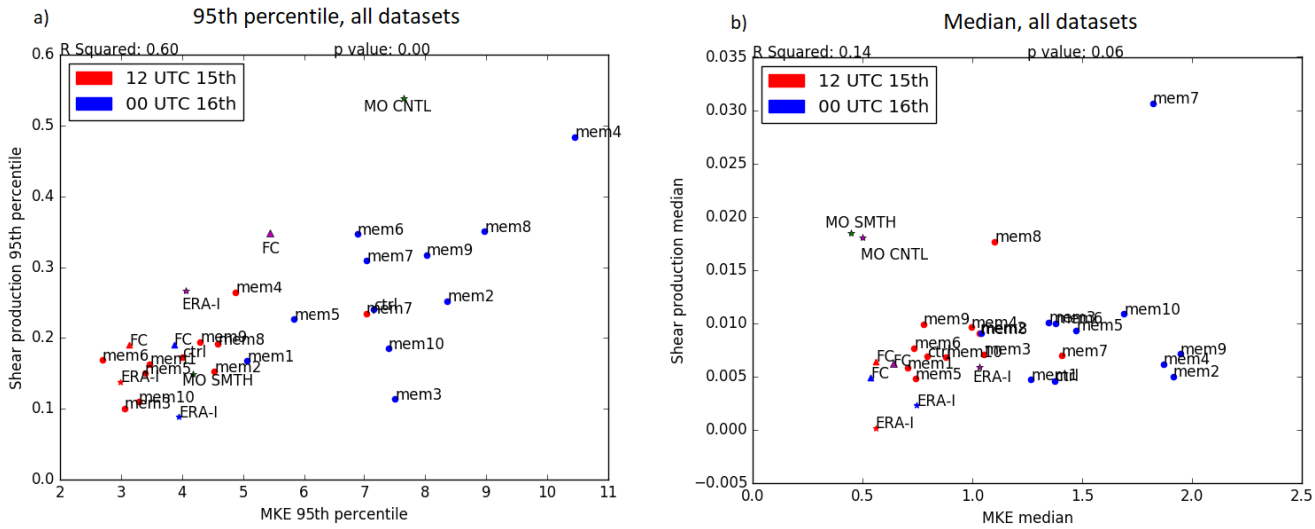


Fig. 4.16 Shear production against mesoscale kinetic energy (MKE) a) 95th percentile and b) median in domain 25-42°N, 85-60°W at 12UTC 15th (blue) and 00UTC 16th (red). 18UTC 15th also shown for forecast (FC) and ERA-Interim (ERA-I) (purple). Met Office control 'MO CNTL' and smooth 'MO SMTH' at 12UTC 15th shown. R squared results just apply to hindcast ensemble (10 members plus 1 control).

Figure 4.16a shows a positive correlation between shear production (95th percentile) and mesoscale kinetic energy (MKE) (95th percentile) (R^2 of 0.6 for hindcast ensemble members). The Met Office CNTL is an outlier, with the 95th percentile of shear production higher than all other runs considered, although the 95th percentile of MKE is within the spread of the ensemble members at the later time step. The difference between the CNTL and SMTH is larger than the spread of the ensemble hindcasts at 12UTC, but similar when compared to the members at 00UTC 16th. The shear production (95th percentile) ensemble hindcast members become more spread with time (also shown in figure 4.11), and as the storm develops, this along with MKE (95th percentile) increase in almost all members. The ERA-Interim, forecast and Met Office SMTH points at 12 UTC 15th are all within the spread of the ensemble despite the coarser resolution or smoothed SST. At 18UTC on the 15th the ERA-Interim and forecast values (purple) increase along both axes, and at the following time step lower values are found. This is because the storm has moved further outside of the selected domain, which is also the case with some of the ensemble members at the later time. The median shear production and median MKE do not have a positive correlation (figure 4.16b). Most of the values have a shear production median of less than ~0.010, with two members and the Met Office CNTL and SMTH as outliers. At the second time step, MKE median increases for all members, but there is little change in shear production median for all except member 7. Although the Met Office CNTL and SMTH have close to double the magnitude of shear production median than the rest of the runs, the MKE median is the weakest. Unlike analysis of the 95th percentile (figure 4.16a), the median shear production against MKE for the CNTL and SMTH Met Office runs are close together, with the spread of the ensemble members much larger than their difference at both time steps. This measure is very sensitive to the domain size, with many grid points outside of the region of shear production obscuring the differences.

4.6 Discussion

Although in the mid-latitudes, the atmosphere generally forces the ocean (Frankignoul and Hasselmann, 1977), oceanic processes can be important to atmospheric variability in the vicinity of the western boundary currents (WBCs) and their associated SST fronts (Lee et al., 2018; Nakamura et al., 2004; Sheldon et al., 2017; Small et al., 2008; Smirnov et al., 2015; Vannière et al., 2017a). This study complements the Sheldon et al. (2017) paper, in which the effect of the SST (absolute and gradient) on instability within an extra-tropical cyclone was investigated. They showed that the SST affected the trajectory of air parcel ascent, proposing both thermodynamical (absolute temperature of the warm tongue) and dynamical (strength

of the SST gradient) effects. This study has examined the same single storm analysed by Sheldon et al. (2017), diagnosing a purely dynamical (mechanical) mechanism in a suite of model runs, to investigate if the large difference in shear production observed in the Met Office simulations (Sheldon et al., 2017) was due to SST, as suggested in the study.

The ensemble forecast hindcast is at a resolution comparable to the Met Office runs, and the shear production found is approximately 5-10 times smaller than in the Met Office CNTL simulation. There are differences in the model and data assimilation as well as the lead time from initialisation, which could have all contributed to this large difference. The spread between the ensemble members was compared to the spread between the Met Office CNTL and SMTH model runs, and revealed that they are similar in terms of percentage, rather than absolute shear production value. Pairs of ensemble members with the same initial SST did not have consistent shear production values or spatial distribution. These results suggest that perhaps the SST did not have primary control on this instability. It is possible that the result from the single Met Office experiment was not robust, or perhaps the spread within the ensemble hindcast analysed in this study is too large. Instead of the warm tongue determining the shear instability in the atmosphere, it is possible that it allows the atmosphere to generate this instability, but the atmosphere has the dominant control on its presence.

In many GCMs, key characteristics of extra-tropical cyclones are sensitive to model resolution (Jung et al., 2006), with intensity too weak, although this generally improves with increasing resolution (Rohrer et al., 2018; Zappa et al., 2013a). It was shown in Sheldon et al. (2017) that the strength of oceanic forcing of an extra-tropical cyclone is reduced with increasing model grid size (figure 4.3), and suggested that upper level oceanic forcing associated with a smoothing of the SST gradient would be almost absent for grid sizes on the order of a few 100 km. In this study, I compared the shear production in ensemble hindcasts (0.2°), a forecast (0.4°), and ERA-Interim (0.75°). Interestingly, the forecast run (0.4°) produced the most intense shear instability. Unlike the comparison of shear production magnitude in the ensemble hindcast with the Met Office CNTL run, which use different models and initialisation times, these datasets are more consistent. However, still this large difference in shear production has been observed. Although (Sheldon et al., 2017) suggested that at a resolution of 100 km, this oceanic forcing would not be observed, ERA-Interim was shown to have shear production in the same location as the other runs (in this study and the Met Office study), just downstream of the warm tongue. Perhaps the threshold of 100 km proposed by Sheldon et al. (2017) is too low, but in order to test this, further analysis is required with a larger sample size.

The single snapshot of data of the Met Office runs and 6- and 12-hourly temporal resolution of the ECMWF data are limiting factors, as the storm characteristics can change

significantly within this time scale. By analysing two (ensemble hindcast) or three (forecast and ERA-Interim) time steps in my analysis, I have increased the sample size and hope to capture storms at locations similar to the Met Office runs. The hindcast analysis was at 12-hourly time steps, taking instantaneously wind fields, and so variability in shorter time scales is not captured. The cyclones develop at different rates in the members and it was not possible to compare storms in exactly the same position in relation to the warm tongue. Using just a single storm and with relatively coarse temporal resolution (6 or 12 hours), it is difficult to assign any differences to resolution alone, and there are also many other model differences, including vertical resolution and data assimilation. To test the importance of resolution for this instability, many more time steps and multiple storms should be examined. For example, storms that cross the warm tongue at different locations and those that are completely isolated, as the presence of a preceding storm to the north of the domain may have affected the evolution of the storm of interest in this study.

This analysis has focussed on the 500 hPa level for both shear production and MKE. This level has been shown in Sheldon et al. (2017) as important for comparing ascent and in the vertical cross sections (figure 4.14), the strongest values of the shear production term are at 500 hPa. However, analysing different levels would be interesting, especially when comparing the different resolution data. Here, the resolution has only been considered in terms of spatial resolution, but in examining ascent, the vertical resolution of these models is also an important factor and could be investigated in further work. Analysis of the vertical sections also suggested that shear production is strongest along the warm front, and determining whether this is the case in a large sample of storms would be useful.

The storm that has been analysed occurred in 2004, when the operational deterministic forecast resolution was 0.4° and the operational ensemble resolution was 0.8°. Since March 2016, the resolution of these models has been 0.1° and 0.2°, and analysing a more recent storm as this high resolution, including in the 51 member operational ensemble would provide more insight into model spread and uncertainty. The temporal resolution of this data is 6-hourly, which is higher than the 12-hourly hindcast ensemble.

The spatial filtering used in the analysis was not exactly the same across all datasets, however, I suggest that the small differences in this filtering would not significantly change the results. The Met Office analysis was originally conducted with a low pass of 240 km, but was also tested with 280 km to match the ensemble hindcast low pass of 2.8° ~280 km, and there was negligible difference (not shown).

This study has tested ideas proposed by Sheldon et al. (2017) with a limited sample, by using a suite of model simulations of different resolution and an ensemble dataset. Shear production of mesoscale kinetic energy has been investigated, and this is a useful

tool that diagnoses a purely dynamical mechanism. With the increasing availability of higher resolution oceanic and atmospheric datasets, such mesoscale instabilities can now be examined. Although upright instability is routinely parametrised in climate models, shear instability is often neglected. Shear instability is apparent in the real atmosphere (Reuter and Yau, 1990) and has been parametrised with measurable improvement in forecasts (Lindstrom and Nordeng, 1992). The oceanic forcing from ocean fronts is not limited to the boundary layer, but is also apparent in model simulations of the free troposphere (Small et al., 2014), with increasing horizontal resolution shown to lead to a fundamentally different in response at upper levels (Smirnov et al., 2015). As well as atmospheric resolution, oceanic resolution is important, as the characteristics of frontal scale ocean–atmosphere interaction, such as the positive correlation between SST and surface wind stress, are only captured when the ocean component is eddy resolving (1/10°) (Bryan et al., 2010). The effect of resolution on ocean-atmosphere interactions over the Gulf Stream is further explored in chapter 5.

4.7 Conclusions

The aim of this study was to address the question, given realistic SST set up, does the instability found in Sheldon et al. (2017) occur in an ensemble of model runs? Results have shown that given a realistic SST pattern, shear production is found in all datasets examined. The 'warm path' mechanism (section 4.1.2) proposed that the SST warm tongue exerts control on atmospheric instability. However, even with a very similar warm tongue set up in all ensemble members, the magnitude of shear production at 500 hPa was variable by more than 60%, which is comparable to the difference between the CNTL and SMTH. This instability is associated with the warm and cold fronts in the extra-tropical cyclone and peaks at around 500 hPa, which is consistent with Sheldon et al. (2017).

A secondary aim was to examine the role of resolution, and results showed that in this single case study and examining just a couple of snap shots in time, the magnitude of shear production could not be directly related to resolution. The ensemble hindcasts were the highest resolution examined in this study, however, the forecast run with half the resolution produced more intense shear instability. The ensemble hindcasts are a similar atmospheric resolution to the CNTL Met Office experiment, but the magnitude was much weaker, closer to that observed in the SMTH experiment. These results appear contrary to those found by (Sheldon et al., 2017), in which dependence on resolution was found.

In the next chapter I will continue to examine the importance of the Gulf Stream warm tongue on shear instability, analysing mean winter activity in relation to phase of the North Atlantic Oscillation (NAO).

Chapter 5

Mesoscale signatures of the North Atlantic Oscillation and interaction with the ocean

This chapter is based on the paper "Mesoscale signature of the North Atlantic Oscillation and its interaction with the ocean" (Cobb and Czaja), submitted to Geophysical Research Letters in September 2018.

Key findings: Presence of mesoscale signatures in the NAO, with the atmospheric feature anchored downstream of that in the ocean.

5.1 Introduction

The leading mode of winter-to-winter climate variability in the North Atlantic basin consists of a meridional shift of the storm-track and associated wind, temperature and precipitation patterns called the North Atlantic Oscillation (NAO) (section 2.4), which is related to sea surface temperature (SST) and storm track activity (Vallis and Gerber, 2008). For example, cyclone tracking indicates a poleward shift of cyclones in positive compared to negative NAO conditions for both ‘extreme’ and ‘non-extreme’ cyclones (Pinto et al., 2009). It has been well established that the NAO exists independently of the presence of the underlying ocean (Thompson et al., 2003), although the changes associated with NAO in air-sea heat fluxes and Ekman advection drive, on monthly timescales, a large scale tripolar sea surface temperature (SST) anomaly pattern (section 2.4).

Recent numerical experiments with high horizontal resolution (grid spacing of 25 km or less) have suggested that the impact of the Gulf Stream on the storm track is mediated by the

frontal circulation embedded in extra-tropical cyclones (chapter 4). In a series of controlled experiments with the UK Met Office Model, results showed that the frontal circulation was destabilized by the Gulf Stream, with associated injection of low potential vorticity air at upper levels and a potential impact on blocking events further downstream. Atmospheric blocking is the presence of large-amplitude synoptic-scale quasi-stationary anticyclones in the extra-tropics (section 2.4), and a comprehensive theory of the blocking life cycle is still missing (Woollings et al., 2018). Rossby wave breaking has strong links to the initiation of blocking in the mid-latitudes. This process disconnects an air mass of subtropical origin further poleward, and this low *PV* air mass develops anomalous anticyclonic circulation. Many studies (e.g. Pfahl et al., 2015) have related blocking events associated with the negative NAO phase to upper level negative *PV* and this can arise from ascent within an extra-tropical cyclone (section 4.1.2).

It is well established that many forecast busts over Europe are due to poor representation of atmospheric blocking (Rodwell et al., 2013). Models often underestimate blocking in the Atlantic, with a strong westerly wind bias. Increasing resolution often reduces blocking errors, but model bias is also an important factor (Scaife et al., 2010), with SST errors in the Atlantic shown to generate much of the westerly bias and the blocking deficit (Scaife et al., 2011). Recent studies with higher resolution forecasting systems have emphasised that the wintertime NAO has useful predictability and possibly more so in nature than in models that have an unrealistically small signal-noise ratio (see chapter 1).

5.2 Research question

Much of the current research on the NAO has been conducted using relatively coarse atmospheric models (several degrees, hundreds of kilometres). The recent release of the ERA5 dataset (https://www.ecmwf.int/en/forecasts/datasets/archive-datasets/reanalysis-datasets/era5), as well as the improvement in resolution in SST data makes it possible to start investigating whether smaller spatial scale signals, typically 100 km or less, are also part of the NAO and its interaction with the ocean. This is the focus of this study, with an emphasis on the wintertime period, which is when the NAO and North Atlantic air-sea interactions are strongest. This is investigated by analysing variables smaller than 100 km, reflecting processes that are occurring within the synoptic scale extra-tropical cyclones.

5.2.1 Aims

- Analyse ERA5 and ERA-Interim in boreal winter and diagnose mesoscale kinetic energy (buoyancy production and shear production) (sections 4.4.1, 5.4)
- Explore the relationship between shear production and the North Atlantic Oscillation (NAO)

5.3 Data

Atmospheric reanalyses are a valuable tool for weather and climate analysis and are often treated as the best-guess 'truth'. New improved reanalyses are generally at increased resolution along with other improvements, such as to the data assimilation scheme and parametrisations.

Table 5.1 Table of differences between ERA-Interim and ERA5

	ERA-Interim	ERA5
Period	1979–present	1950–present *2008–present available
Assimilation system	IFS Cycle 31r2 4D-Var	IFS Cycle 41r2 4D-Var
Spatial resolution	79 km globally (0.75°), 60 levels to 0.1 hPa	31 km globally (0.25°), 62km for the Ensemble of Data Assimilations (EDA), 137 levels to 0.01 hPa
Output frequency (temporal resolution)	6-hourly analysis field. Forecast fields on surface and pressure levels 3-hourly up to 24 hours, with reduced frequency up to 10 days	Hourly analysis fields. Hourly forecast fields, 3-hourly for the Ensemble of Data Assimilations (EDA).
Uncertainty estimates	None	10-member Ensemble of Data Assimilations (EDA)
Model input	As in operations (inconsistent SST)	Appropriate for climate (e.g. CMIP5 greenhouse gases, volcanic eruptions, SST and sea-ice cover)

Two reanalysis datasets produced by the European Centre for Medium-Range Weather Forecasts (ECMWF) are analysed. ERA-Interim spans 1979-present and has a spatial resolution of 0.75° (Dee et al., 2011). The new ERA5 reanalysis is the 5th major global reanalysis produced by ECMWF and has a finer resolution of 0.25° alongside other model

improvements, including increased temporal resolution (table 5.1). The single member deterministic output from ERA5 is used from 2008-present as previous years have not yet been released.

The period analysed is December, January and February (hereafter DJF), for 5 positive NAO and 2 negative NAO years (table 5.2). The selection of positive and negative NAO years was made using NAO Index Data provided by the Climate Analysis Section, NCAR, Boulder, USA, Hurrell (2003). From 2008 to 2017, a season was selected when both the station and principal component time series data of sea level pressure agree on sign of NAO index.

Table 5.2 NAO positive and negative winters (DJF)

Positive	2011–2012	2013–2014	2014–2015	2015–2016	2016–2017
Negative	2009–2010	2010–2011			

It is clear from table 5.2 that there is some persistence of NAO, as several consecutive years tend to remain in the same phase. There are a number of mechanisms that influence the NAO (see section 2.4), for example solar variability (Scaife et al., 2013).

5.4 Method

The diagnostics are production terms for mesoscale kinetic energy (MKE) and are consistent with those used in chapter 4. We continue to use a spatial filter of approximately 3°, with ERA-Interim using 5 grid points, and ERA5 using 15 (table 4.3). Equations for MKE, shear production and buoyancy production are detailed below, with full details in section 4.4.1. The variables u, v and ω are zonal, meridional and vertical winds, α is specific humidity and p is pressure.

$$MKE = \frac{\overline{u'^2 + v'^2}}{2} \tag{5.1}$$

$$\frac{\partial}{\partial t} MKE = \text{Shear production + Buoyancy production} + ... \tag{5.2}$$

where

$$\text{Shear production (mWkg}^{-1}) = -\left(\overline{\omega' u'} . \frac{\partial \overline{u}}{\partial p} + \overline{\omega' v'} . \frac{\partial \overline{v}}{\partial p} \right) \tag{5.3}$$

and

$$\text{Buoyancy production (mWkg}^{-1}) = -\overline{\omega' \alpha'} \tag{5.4}$$

The variables are instantaneous, defined as from the last model time step, which is 30 minutes in ERA-Interim and 15 minutes in ERA5. Twelve pressure levels were used for this analysis (200, 300, 400, 500, 600, 700, 800, 850, 875, 900, 925, 950 hPa), with the lowest and highest omitted from the shear diagnostic calculation as they require another level from which to calculate the shear term. Values are then interpolated to every 25 hPa, giving 31 levels in total, and 26 for shear production. In this analysis, integration across levels 300-600 hPa and 625-925 hPa are classified as upper and lower levels, respectively. When integrated across levels both production terms have the units Wm^{-2}. An average over each winter season is calculated, and then averaged again over multiple seasons to give NAO+ (5 season mean) and NAO- (2 season mean).

The SSTs used in both ERA5 and ERA-Interim for the period 2008-present are from the Operational Sea Surface Temperature and Sea Ice Analysis (OSTIA), which has a resolution of 0.05° (Donlon et al., 2012). The atmospheric model used in ERA-Interim (1979-present) is consistent throughout the time period, but the SST and sea ice concentration (SIC) products have changed (table 5.3). OSCAR (Ocean Surface Current Analysis Real-time) (Bonjean and Lagerloef, 2002) contains near-surface ocean current estimates, on a 0.33° grid. Horizontal velocity is estimated from sea surface height, surface vector wind and SST from satellites and in situ instruments in a model combining geostrophic, Ekman and Stommel shear dynamics, and a complementary term from the surface buoyancy gradient. The temporal resolution of variables used from ERA5, ERA-Interim and OSCAR are 1-hourly, 6-hourly and 5-day, respectively. The Argo project collects high-quality temperature and salinity profiles from the upper 2000 m of the ice-free global ocean and currents from intermediate depths using battery-powered autonomous floats, and in this study we examine the interpolated gridded dataset from Roemmich and Gilson (2009).

Table 5.3 SST and SIC products used in ERA-Interim

Period	**Dataset**	**Resolution**
1979–Nov 1981	HadISST Rayner et al. (2003)	1°
Dec 1981 – June 2001	NCEP 2DVAR	1°
July 2001 – Dec 2001	NCEP OISSTv2 (OI – Optimal Interpolation) Reynolds et al. (2002)	1°
Jan 2002 – Jan 2009	NCEP RTG (Real Time Global) Thiébaux et al. (2003)	0.5°
Feb 2009 – present	OSTIA Donlon et al. (2012)	0.05°

Results for positive (NAO+) and negative (NAO-) NAO years are shown, as well as their difference. The significance of this difference is calculated using the t-test of all hourly data points over the 5 (NAO+) and 2 (NAO-) winters. Due to the decorrelation time scale of NAO, the number of degrees of freedom is reduced from the large number of hourly values. An NAO cycle is approximately 10 days (Feldstein, 2000) and so within the 90 days winter season, there is a maximum of 9 independent cycles. To be conservative, this value has been halved (to 4), therefore, 5 NAO+ winters and 2 NAO- winters give 20 and 8 independent NAO, yielding 28 degrees of freedom.

5.5 Results

Ocean analysis is presented first, followed by atmospheric analysis focussing on results from ERA5. In section 5.5.4, these results are compared to those found using ERA-Interim. NAO+ and NAO- refer to the mean over 5 positive, and 2 negative winter seasons, respectively.

5.5.1 Mesoscale signature in the ocean

Comparison of NAO+ and NAO- SSTs in ERA5 reveals the classic large-scale SST tripole, and embedded therein is a mesoscale structure, with a maximum warming of 3°C in NAO+ to the east of Cape Hatteras (figure 5.1a). The warm tongue of the Gulf Stream is narrower, warmer and more extended towards the north-east in NAO+, as seen by comparison of the absolute SSTs in figure 1c,d, with the 21 °C isotherm (bold line) approximately collocated with the 20 °C isotherm in NAO- (figure 5.1). Examination of surface currents shows that there is an acceleration along the axis of the warm core of the Gulf Stream and a northward shift in NAO+ compared to NAO- (figure 1b). The mean surface current speed over 8 boreal winters (5 NAO+, 2 NAO-, 1 neutral) (contour line in figure 5.1c), is $0.5 \mathrm{ms}^{-1}$ which is comparable to the magnitude of the anomalies. This suggests a very significant change of the current. Analysis of meridional hydrographic sections from regridded Argo data (Roemmich and Gilson, 2009) in the western North Atlantic in figure 5.1e (colour) shows a shallow signature of warmer water reflecting the warm part of the SST tripole, but also a warm anomaly extending deeper to approximately 1000 m around 37°N. The co-location of this anomaly with the time mean temperature front (contours in figure 5.1e) suggests that a poleward shift of the latter is responsible for the anomaly. In the following figures the location of the 21°C isotherm at the sea surface will be used to track the extension of the separated Gulf Stream.

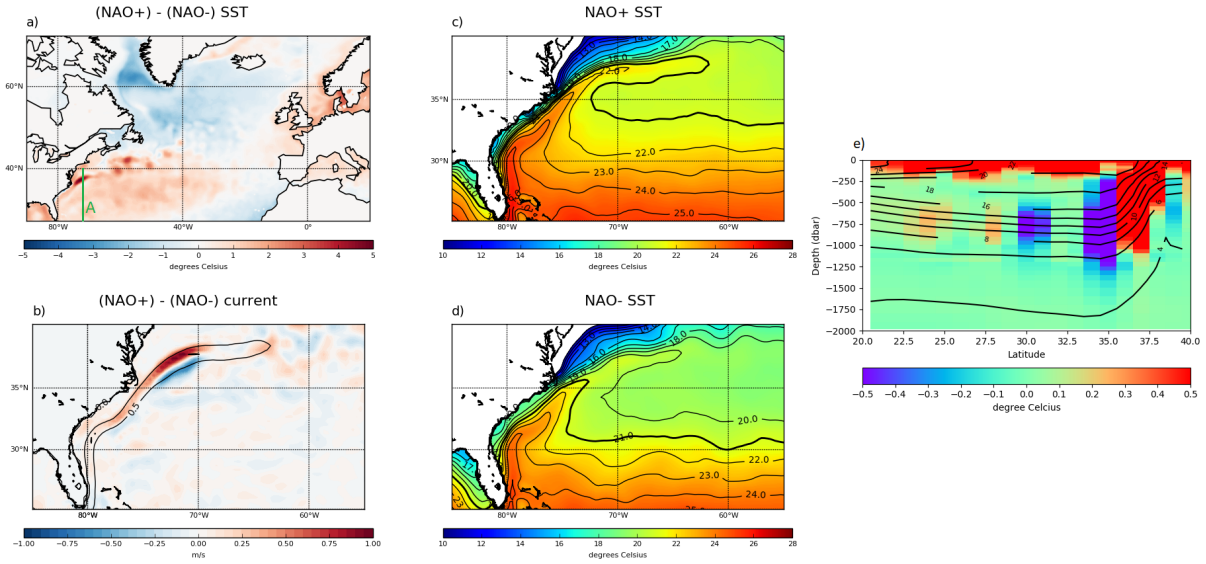


Fig. 5.1 a) Difference in SST between positive and negative NAO years. Green line marked 'A' shows the position of the vertical section shown in panel e. SST in c) NAO+ and d) NAO- (21°C isotherm in bold). b) Same as (a) but for surface currents (colour). The contour line indicates where the time mean current equals 0.5 m/s. e) Same as (a) but for potential temperature at 72.5°W (colour). Black contours indicate the mean potential temperature (ci = 2K) from Roemmich and Gilson (2009). For (a-d) the NAO years are 2009-10, 2010-11 for NAO- and 2011-12, 2013-14, 2014-15, 2015-16 and 2016-17 for NAO+. For (e) the NAO years are 2009-10, 2010-11 for NAO- and 2011-12, 2013-14 and 2014-15 for NAO+. All data averaged over DJF.

5.5.2 Mesoscale signature in the atmosphere

Following results shown are positive production terms (equations 5.3, 5.4) calculated from hourly ERA5 reanalysis data. The 21°C isotherm is shown in following figures.

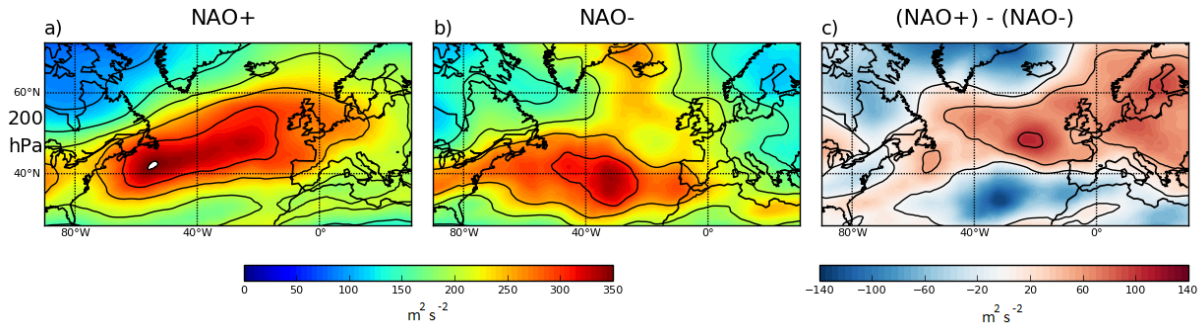


Fig. 5.2 Large scale time mean EKE at 200 hPa for a) positive and b) negative NAO years and c) the difference between positive and negative NAO winters. Calculated from hourly ERA5 data.

We recover the standard north-south dipole in classic variables such as time mean eddy kinetic energy (EKE) at 200 hPa (figure 5.2), showing the poleward and zonal extension with NAO phase. EKE has been calculated using equation 5.1, but using the time mean (DJF) value as the 'bar' term and the departure from this as the 'prime'.

The distribution of MKE at upper and lower levels for positive and negative NAO winters, as well as their difference, is displayed in figure 5.3. At upper levels (top panels) there is an enhancement of MKE activity centred at 60°N in NAO+ (figure 5.3a), while it is more restricted to 45°N in NAO- (figure 5.3c). This reflects the expected poleward displacement of the synoptic systems with NAO (e.g. Pinto et al., 2009) and is clearly visible in the meridional dipole structure centred at 50°N in figure 5.3e. A similar large-scale feature is also seen at lower levels (bottom panels), but with the addition of a smaller scale, south-west to north-east oriented dipole near the Gulf Stream (figure 5.3f). To investigate the cause of this feature we display the production of MKE by buoyancy (figure 5.4) and shear (figure 5.6) effects.

Mesoscale buoyancy production

The spatial distribution of buoyancy production shows differences with NAO phase, with an increase at higher latitudes and decrease in lower latitudes in NAO+, related to the expected shift of synoptic activity.

In NAO+, the magnitude of buoyancy production is approximately 20% higher in the lower atmosphere (600-925 hPa) than the upper atmosphere (300-600 hPa), whereas in NAO- the magnitude is more consistent (figure 5.4). At low levels in NAO+, there is a displacement

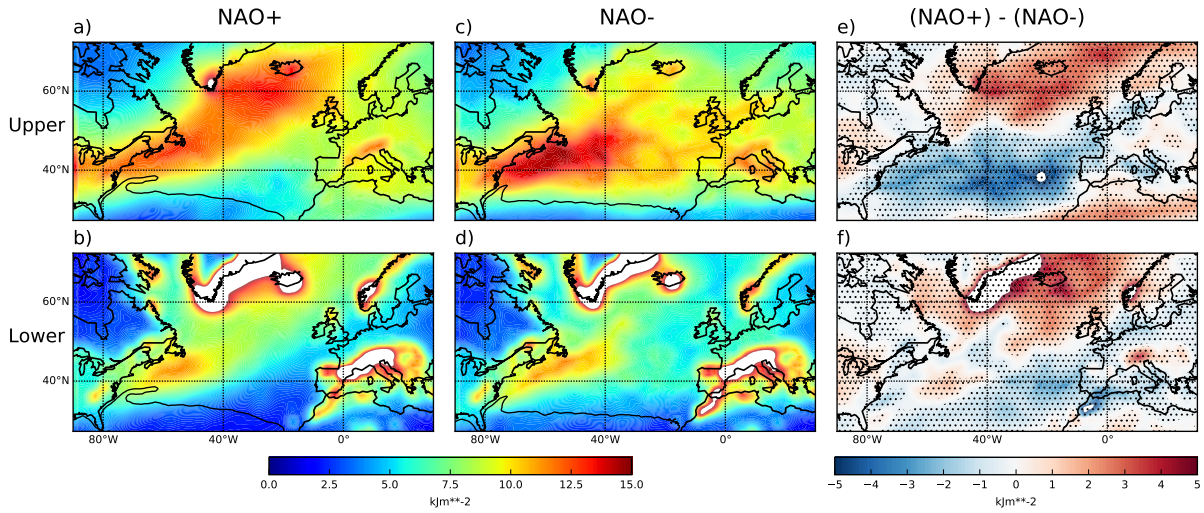


Fig. 5.3 Distribution of mesoscale kinetic energy, eq. (4.1), integrated over the upper atmosphere (300-600 hPa) in (a) positive (c) and negative NAO phases and the lower atmosphere (625-925 hPa) in (b) positive (d) and negative NAO phases. The difference between positive and negative NAO winters is displayed in (e) upper atmosphere and (f) lower atmosphere. Stippling indicating statistical significance at the 95% level. The 21 °C SST isotherm is shown in black contours in panels a,b,c,d. At positive saturation, white is shown. The units in all panels are kJm^{-2}.

of buoyancy north-eastwards along the warm tongue, which was also observed in MKE (figure 5.3f).

Surface latent heat flux ($SLHF$) and surface sensible heat flux ($SSHF$) are negative in an upward direction and have a similar spatial distribution, but the former has approximately double the magnitude (figure 5.5). Across much of the North Atlantic region, heat flux is greater in NAO-, with larger heat loss in the Labrador Sea in the NAO+. In the Gulf Stream warm tongue region, an intensification of this difference with NAO phase is apparent for both $SLHF$ and $SSHF$ (figures 5.5e,f), aligned with the local signature observed in buoyancy and MKE (figures 5.4, 5.3).

Mesoscale shear production

For the shear production term, a zonal extension is observed in NAO-, especially in the upper atmosphere (figure 5.6), consistent with the pattern of buoyancy and other variables so far presented, in relation to the shift in synoptic activity. Over the Gulf Stream warm tongue region, shear production is displaced further north-east in NAO+, along the axes of the extended warm tongue; a pattern which has been seen in MKE, heat flux and buoyancy (figures 5.3, 5.4, 5.5), but this southwest-northeast dipole is particularly pronounced in the

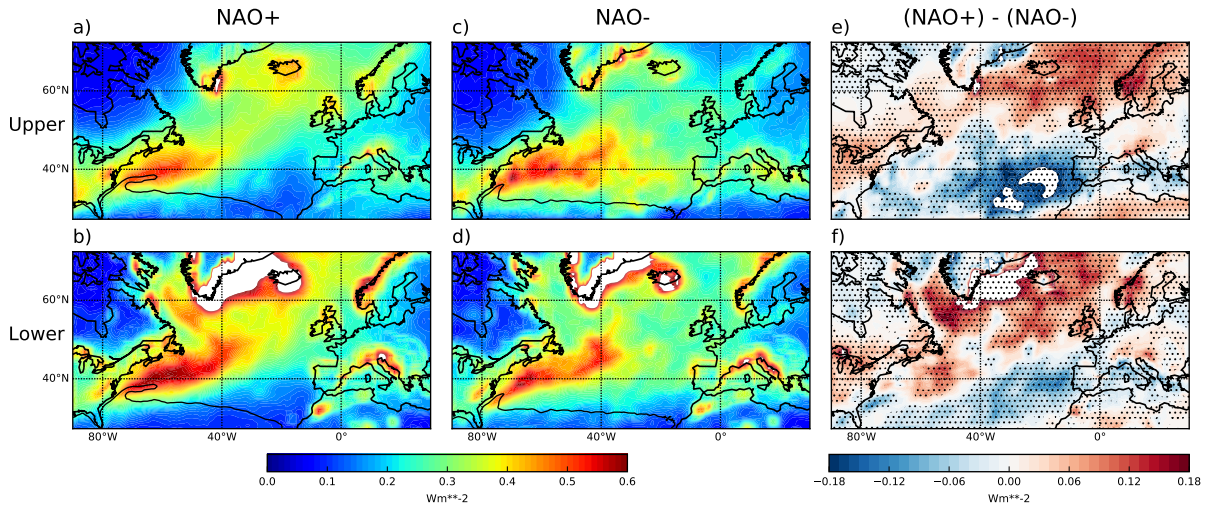


Fig. 5.4 Distribution of positive buoyancy integrated over the upper atmosphere (300-600 hPa) in (a) positive (c) and negative NAO phases and the lower atmosphere (625-925 hPa) in (b) positive (d) and negative NAO phases. The difference between positive and negative NAO winters is displayed in (e) upper atmosphere and (f) lower atmosphere. Stippling indicating statistical significance at the 95% level. The 21 °C SST isotherm is shown in black contours in panels a,b,c,d. At positive saturation, white is shown. The units in all panels are Wm^{-2}.

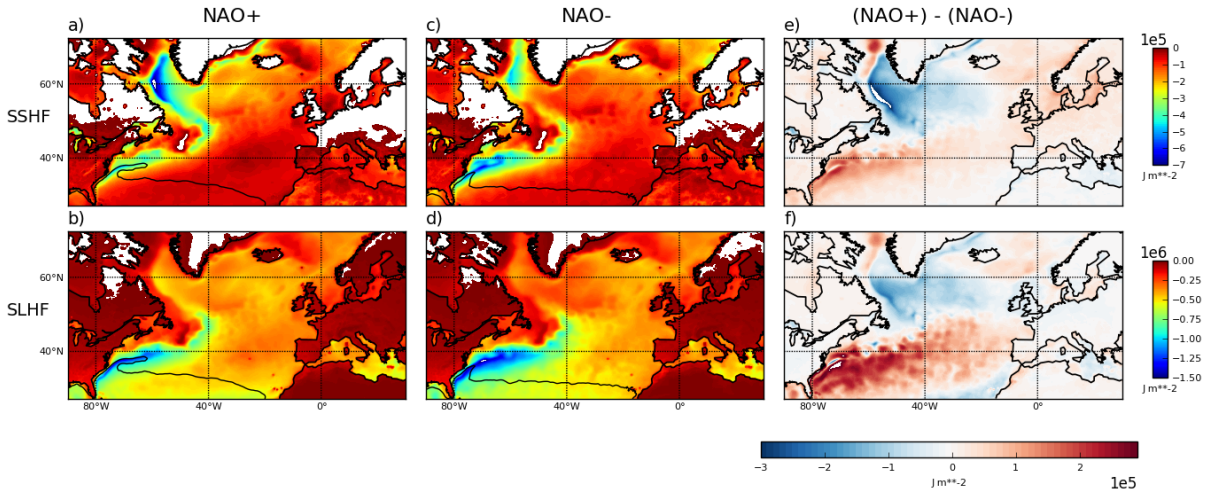


Fig. 5.5 Distribution of surface heat flux: sensible (*SSHF*) in (a) positive and (c) negative NAO phases, and latent (*SLHF*) in (b) positive and (d) and negative NAO phases. Fluxes are negative in the upward direction. Difference in NAO positive-NAO negative for (e) sensible heat flux and (f) latent heat flux. The 21 °C SST isotherm is shown in black contours. At positive saturation, white is shown.

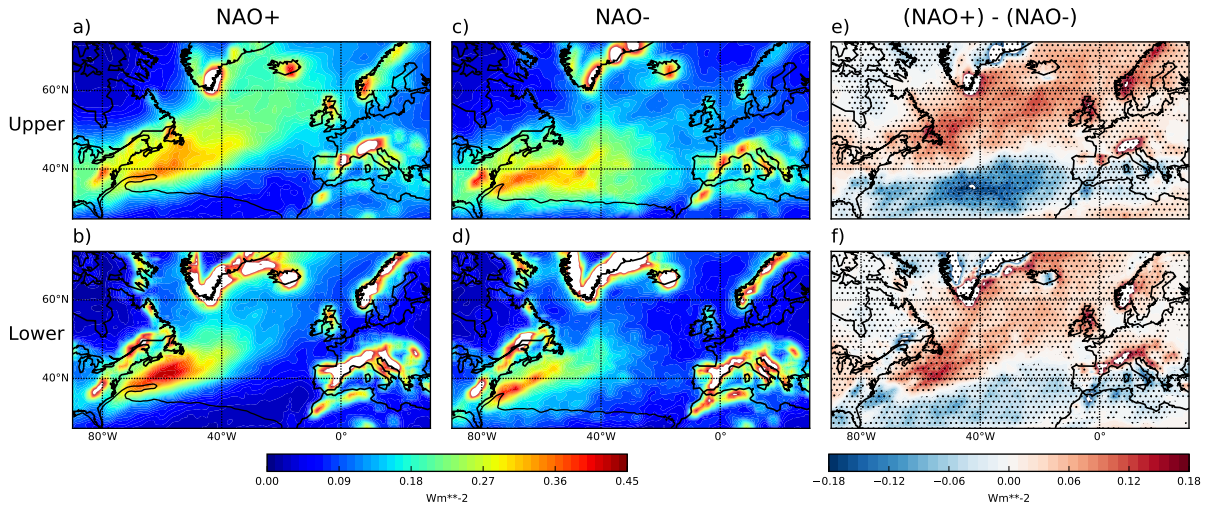


Fig. 5.6 Distribution of positive shear production integrated over the upper atmosphere (300-600 hPa) in (a) positive (c) and negative NAO phases and the lower atmosphere (625-925 hPa) in (b) positive (d) and negative NAO phases. The difference between positive and negative NAO winters is displayed in (e) upper atmosphere and (f) lower atmosphere. Stippling indicating statistical significance at the 95% level. The 21 °C SST isotherm is shown in black contours in panels a,b,c,d. At positive saturation, white is shown. The units in all panels are Wm^{-2}.

shear production composite (figure 5.6f). This suggests that, as the synoptic systems shift poleward in NAO+, so does the mesoscale activity embedded in them. When the Gulf Stream warm tongue is more extended, the mesoscale activity is shifted to the north-east, while it is more limited to the south-west part of the basin when the warm tongue is itself less extensive. This suggests an anchoring of the production of MKE by the Gulf Stream warm tongue, a distinct feature from the large scale poleward shift dominating the upper level composites. This is a new 'mesoscale' structure of air-sea interactions embedded within the large scale meridional shift described so far in the literature on NAO.

The largest values of shear production are over high orography, particularly Greenland, where white is colour bar saturation. Away from these regions, the most intense values are downstream of the warm tongue, where there is also the maximum difference between NAO+ and NAO-.

The vertical distribution of buoyancy and shear production is relatively homogeneous throughout the troposphere, with peaks around 500 hPa (as seen in Chapter 4 for one individual storm).

5.5.3 Potential vorticity (*PV*)

The anchoring of mesoscale activity by the Gulf Stream is further supported by inspection of the Ertel potential vorticity (*PV*) field. Figure 5.7 shows the frequency (as percentage of DJF) of occurrence of negative *PV* averaged over upper and lower levels and isentropic *PV* at 315 θ.

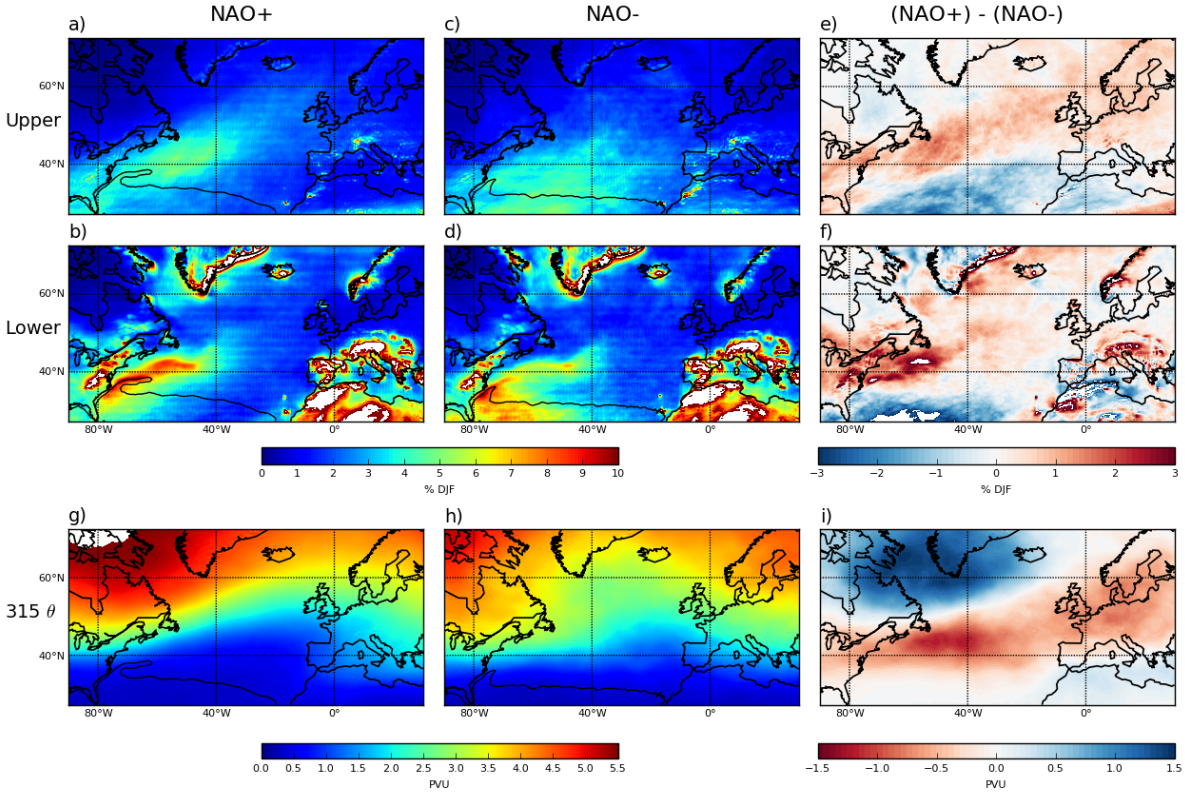


Fig. 5.7 Frequency (percentage of DJF) of negative *PV* averaged over the upper atmosphere (300-600 hPa) in (a) positive (c) and negative NAO phases and averaged over the lower atmosphere (625-925 hPa) in (b) positive (d) and negative NAO phases. Difference in frequency of negative *PV* NAO positive-NAO negative in the (e) upper atmosphere and (f) lower atmosphere. Isentropic *PV* at 315 θ for (g) NAO positive, (h) NAO negative, (i) NAO positive-NAO negative. The 21 °C SST isotherm is shown in black contours. At positive saturation, white is shown.

In a 2D flow in thermal wind balance this is known as a signature of instability (e.g. Bennetts and Hoskins, 1979) and so provides an alternative view to the shear production term in figure 5.6. ERA5 outputs *PV* on pressure levels, from which negative values are counted and then averaged over the upper and lower levels, so 10% of negative frequency means that 10% of hourly data within the level bounds has $PV < 0$.The frequency of occurrence of these events is larger at lower levels and is about 5 to 10 % of the time. The spatial

distribution confirms the pattern from figures 5.3-5.6, that upper levels are dominated by the classic north-south shift of the storm track but that there is an additional local signal over the warm tongue. There is a more pronounced northward extension of occurrence of $PV < 0$ events when the Gulf Stream warm tongue is more extended in NAO+ (figure 5.7b), and a limited occurrence of these events north of 40°N in NAO- when the warm water core of is more confined to the American coast (figure 5.7d). There is also a relatively frequent occurrence of negative PV at low latitudes, across much of the western part of the Atlantic basin in NAO- (figure 5.7c,d). The presence of negative PV in the upper atmosphere over land is absent, whereas there was strong positive shear production. This suggests that the shear production was mountain wave drag over regions of high orography. The mean total (positive and negative) PV values at 300 hPa (figure 5.7g,h) highlights the strong PV gradient in NAO+ and lower values of PV in the north-west and south-east of the domain in NAO-.

Finer analysis of the vertical dependence of the signals in figure 5.7 indicates that the high frequency of negative PV in the lower levels is dominated by that at 925 hPa (figure 5.8). This is consistent with Vannière et al. (2016), who showed that south-eastward advection of continental air over the ocean by a cyclone in a cold air outbreak produces $PV < 0$ near the sea surface with a frequency comparable to that of cold fronts (5-10%). The lower level mean frequency of $PV < 0$ (figures 5.7b,d) show a frequency of occurrence comparable to that of cold fronts (5-10%) proposed in Vannière et al. (2016), but figure 5.8a shows much larger frequency, suggesting that not all storms generate a front large enough to be counted by such frontal detection studies. Throughout the rest of the troposphere, the frequency of events with $PV < 0$ is consistently lower, but with a relative increase at the 300 hPa. This is expected if strong updrafts carry the $PV < 0$ airmass from the boundary layer to these levels and then subsequently spread that airmass nearly horizontally. Both positive and negative changes in PV are expected from latent heat release during ascent but the net effect of these is smaller ($\approx$ +0.1 PVU, see Madonna et al. (2014)) than the initial negative PV near the surface ($\approx$ -1 PVU, see Vannière et al. (2016)). Strong ascent required to bring the PV all the way to 300 hPa are much less frequent than the cold air outbreak, and so the frequency of such $PV < 0$ is much reduced. The middle layers hardly keep track of this because of fast ascent, while the spreading at upper levels allows it to be seen there. The mean value of negative PV at each layer shows the opposite pattern, with largest magnitude in the mid layers.

A more detailed examination of negative PV at levels 300, 500 and 925 hPa (figure 5.9) in the domain 80-40°W 30-60°N for NAO+, highlights the large differences in frequency of small negative PV values. These small values (< 1 PVU) occur 5 times more frequently at 925 hPa than 300 hPa and 5-10 times more at 300 than 500 hPa. These small values dominate

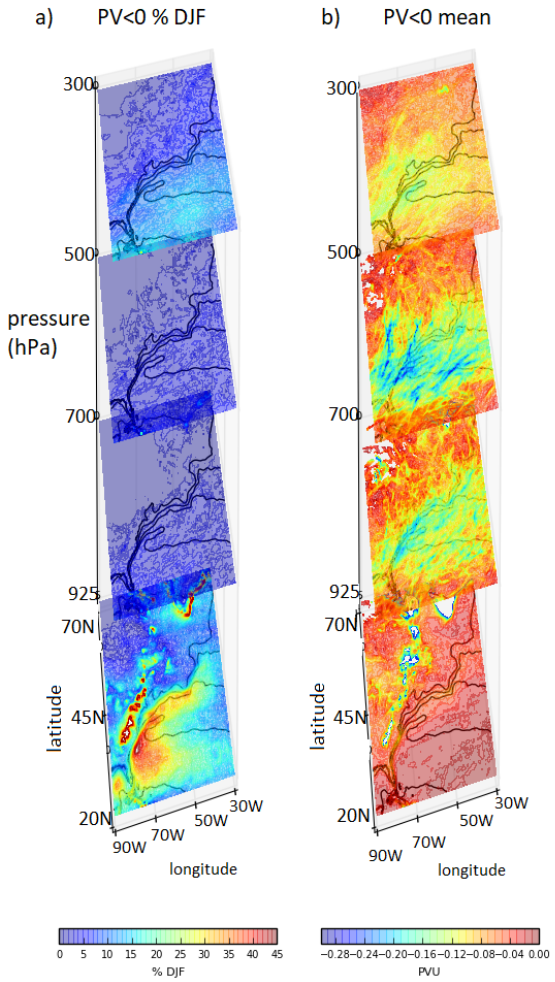


Fig. 5.8 Stacked contour plot of a) negative *PV* frequency as %DJF and b) mean negative *PV* at 925, 700, 500, 300 hPa. SST isotherms shown in black contour lines. Results shown for NAO+ but similar distribution for NAO- (not shown).

the values in figure 5.8a. Large negative values (< -5 PVU) are only observed at 925 hPa and occur due to these cold air outbreaks in the cold sector of cyclones. The mean at each of these levels within the specified domain are -0.101, -0.136, -0.081 for 300, 500 and 925 hPa respectively, which is reflected in figure 5.8b. Figures 5.8 and 5.9 show results for the NAO+ years, but we observe a similar vertical distribution in NAO-.

5.5.4 Comparison with ERA-Interim

The same analysis conducted with ERA-Interim 6-hourly data revealed the same spatial pattern in buoyancy and positive shear production with NAO phase, but with differences in magnitude. In ERA-Interim, the values as well as differences of shear and buoyancy

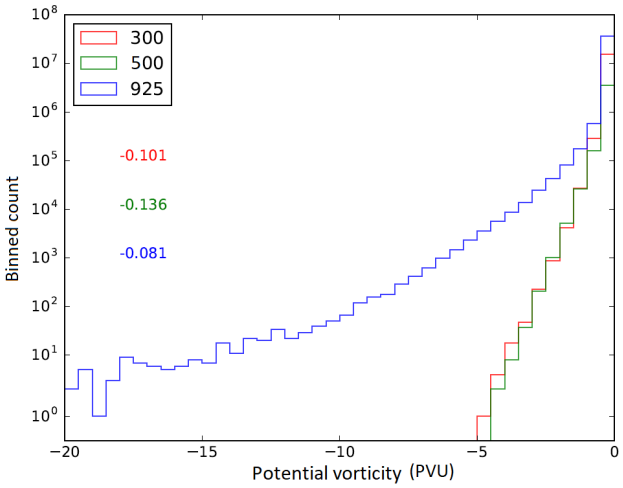


Fig. 5.9 Histogram of negative *PV* in domain 80-40°W 30-60°N for NAO+. Bin size 0.5, range -20 PVU to 0 PVU. Results shown for NAO+ but similar distribution for NAO- (not shown). Mean negative *PV* values at each level given in same colour as line.

Table 5.4 ERA-Interim NAO+ and NAO- winters. *Post-2002. ** Weak signal (both indices <=0.4). Counts of seasons in brackets are those once the seasons with weak signals have been removed.

Positive (12 pre-2002, 8 post-2002)	1980–1981 1982–1983 1983–1984 1988–1989 1989–1990 1990–1991 1991–1992 1992-1993 1993-1994 1994-1995 1998–1999 1999–2000 2004–2005* 2006–2007* 2007–2008* 2011–2012* 2013–2014* 2014–2015* 2015–2016* 2016–2017*
Negative (8 (6) pre-2002, 5 (3) post-2002	1981–1982 1984–1985 1985–1986 1986–1987 1987–1988** 1995–1996 1997–1998** 2000–2001 2002–2003*** 2003–2004* 2005–2006*** 2009–2010* 2010–2011*

production approximately halved. The low pass spatial filter (equations 5.3, 5.4) remains consistent, with 3° (compared to 2.8° for ERA5), but because of the coarser resolution, in ERA-Interim the 'prime' term now represents at most scales of 0.75° as opposed to 0.25° in ERA5.

The ERA-Interim dataset starts in 1979 and so provides an opportunity to conduct this same analysis over a longer period, with an increased sample size of NAO+ and NAO- years. Analysis over the full time period includes 20 NAO+ winters and 13 NAO- (table 5.4). However, four of the NAO- have weak signals (both indices <=0.4) and so are excluded from the analysis. At the beginning of 2002, the SST and sea ice concentration(SIC) resolution increased from 1° to 0.5° (table 5.3), and so two separate time periods are examined (pre- and post-2002). Using 20 NAO+ and 9 NAO-, we have compared the shear production term

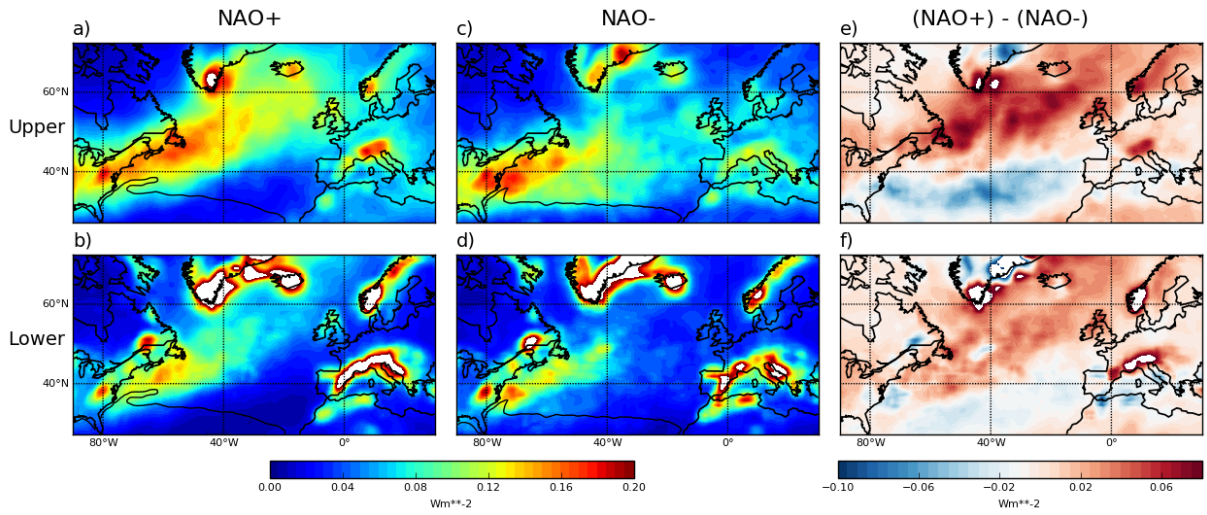


Fig. 5.10 ERA-Interim: Distribution of positive shear production integrated over the upper atmosphere (300-600 hPa) in (a) positive (c) and negative NAO phases and the lower atmosphere (625-925 hPa) in (b) positive (d) and negative NAO phases. The difference between positive and negative NAO winters is displayed in (e) upper atmosphere and (f) lower atmosphere. The 21 °C SST isotherm is shown in black contours in panels a,b,c,d. At positive saturation, white is shown. The units in all panels are Wm^{-2}.

pre-2002 (12 NAO+, 6 NAO-) and post-2002 (8 NAO+, 3 NAO-) (figure 5.11). The change in SST resolution is clearly seen between the two periods with the 21°C contour. In the early period, the warm tongue is weak and no clear difference is seen in SST contour between NAO+ and NAO-. However, in the later period, there is a more defined warm tongue and a clear extension and intensification is visible in NAO+ compared to NAO-. In this period, the mesoscale signal over the Gulf Stream warm tongue is seen in shear production (figure 5.11f), and this is not apparent in the early period without the warm tongue (figure 5.11e). In the absence of this warm tongue, the mesoscale production terms are still observed, with a magnitude similar to that when the warm tongue is present.

As well as the difference in atmospheric resolution, the temporal resolution is different in ERA-Interim, with 6-hourly data, compared to hourly ERA5 data. To investigate whether this had an effect on the result, the ERA5 data was sub-sampled to 6-hourly time steps and the same analysis was conducted. No difference in the result obtained using hourly data is seen (not shown). This result suggests that the dynamics is not too fast and a resolution of 6 hours is sufficient for the purpose of examining this instability.

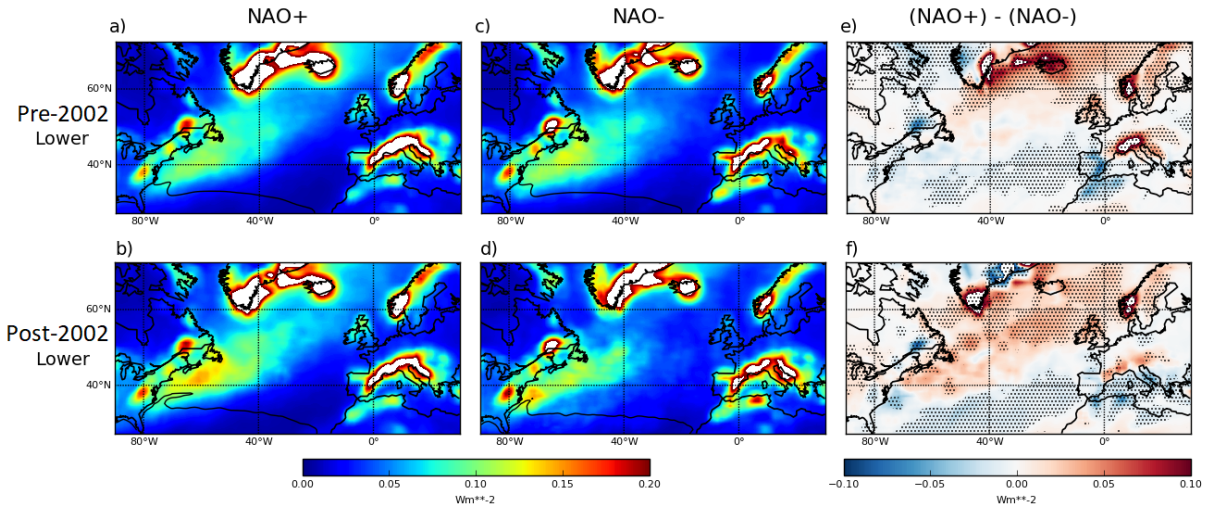


Fig. 5.11 ERA-Interim: Distribution of positive shear production integrated over the lower atmosphere (625-925 hPa) for years pre-2002 (1° ocean resolution) in (a) positive (c) and negative NAO phases and (e) difference; and years post-2002 (0.5-0.05° ocean resolution) in (b) positive (d) and negative NAO phases and (f) difference. Stippling indicating statistical significance at the 95% level. The 21 °C SST isotherm is shown in black contours. At positive saturation, white is shown.

5.6 Discussion

The results from ERA5 are admittedly based on a limited sample size due to the current availability of the dataset. The degrees of freedom for the significance testing of the ERA5 relationships was tested and even smaller number of degrees of freedom (less than 10) still support statistical significance. To further test the robustness, the analysis was repeated with ERA-Interim 6-hourly data (1979-present) (Dee et al., 2011), providing 20 NAO+ and 9 NAO- winters. To be consistent, the 'bar' term in equations 5.1, 5.3, 5.4 was set to cover the same area as in ERA5, but because of the coarser resolution in ERA-Interim the 'prime' term now represents at most scales of 0.75° as opposed to 0.25° in ERA5. Results over the 1979-2017 period reveal the same large-scale poleward signal associated with storm track in NAO+ compared to NAO-, as well as the more localised signal over the Gulf Stream region (figure 5.10). As in ERA5 the latter is clearly seen at lower levels although with half the magnitude. Thus suggesting that this localised feature is robust. Interestingly, comparison of this feature only showed up clearly after 2002 (figure 5.11), which is when the resolution of the SST data used in ERA-Interim was improved (first in January 2002 from 1° (Reynolds et al., 2002) to 0.5° (Thiébaux et al., 2003) and then again in February 2009 to 0.05° (Donlon et al., 2012).

The difference in magnitude of shear production between these two datasets with different resolutions shows the importance of resolution when examining processes on the mesoscale. This dependence on resolution was reported in Sheldon et al. (2017) but was not apparent in the previous chapter (4) when a single storm was examined. This study has used a much larger sample size than that used in chapter 4, so supports the idea that there is a dependence on spatial resolution. The difference in temporal resolution between these two datasets was explored by sub-sampling the ERA5 data, and no difference in the result was found. When the full ERA5 dataset (1950-present) is released (in 2019), it would be interesting to repeat this analysis with a much larger NAO sample size and also examine the effects of the changing SST and SIC input data. For the production of ERA5, HadISST2 (0.25°) SST and SIC will be used until 2007, and thereafter OSTIA (0.05°) is used (Hirahara et al., 2016).

The southwest-northeast dipole over the Gulf Stream warm tongue highlighted in this study is most readily seen at lower levels in figures 3,4,5 but a finer analysis of pressure levels indicates that it is also present at upper levels (see the discussion of *PV* maps in section 5.5.3). Indeed, it is a distinct feature from the surface storm-track related to the Gulf Stream and discussed in Booth et al. (2010) with a much coarser dataset (1.125° for 10 m winds and 2.5° for 850 hPa winds). The study by Sheldon et al. (2017) (see chapter 4, figure 4.3), as well as the difference in ERA-Interim composites with SST resolution noted above, give support for the view that this relationship is causal.

This study analyses atmospheric and oceanic variables during the NAO winter (DJF). However, in order to test whether there is a forcing of the atmosphere by the ocean, it is necessary to examine data in the months preceding winter. Figure 5.12 shows the difference in SST and surface currents between NAO+ and NAO- in the months leading up to and during winter. The results show that this mesoscale signature observed in SST and originally presented in section 5.5.1 is only apparent in the winter season, although there is a weak signal in November. The surface current anomalies in this region off the coast of Cape Hatteras and extending north-eastwards are present in June-September as well as during the winter season, with a similar intensity (+/- 0.5 m/s contour lines). The surface current signal is not apparent in November, but develops quickly in December, where there is the most coherent dipole structure between NAO+ and NAO-. With the strong change in surface currents and SST in December, and the beginning of a mesoscale change in SST in November, it is possible that the atmosphere is forced by underlying oceanic processes, which continue through the winter season as seen in January and December (figure 5.12). More modelling work is clearly needed to test this hypothesis fully.

In agreement with a previous experimental study Sheldon et al. (2017), this mesoscale SST signature gives rise to an increase in shear production downstream, with the associated

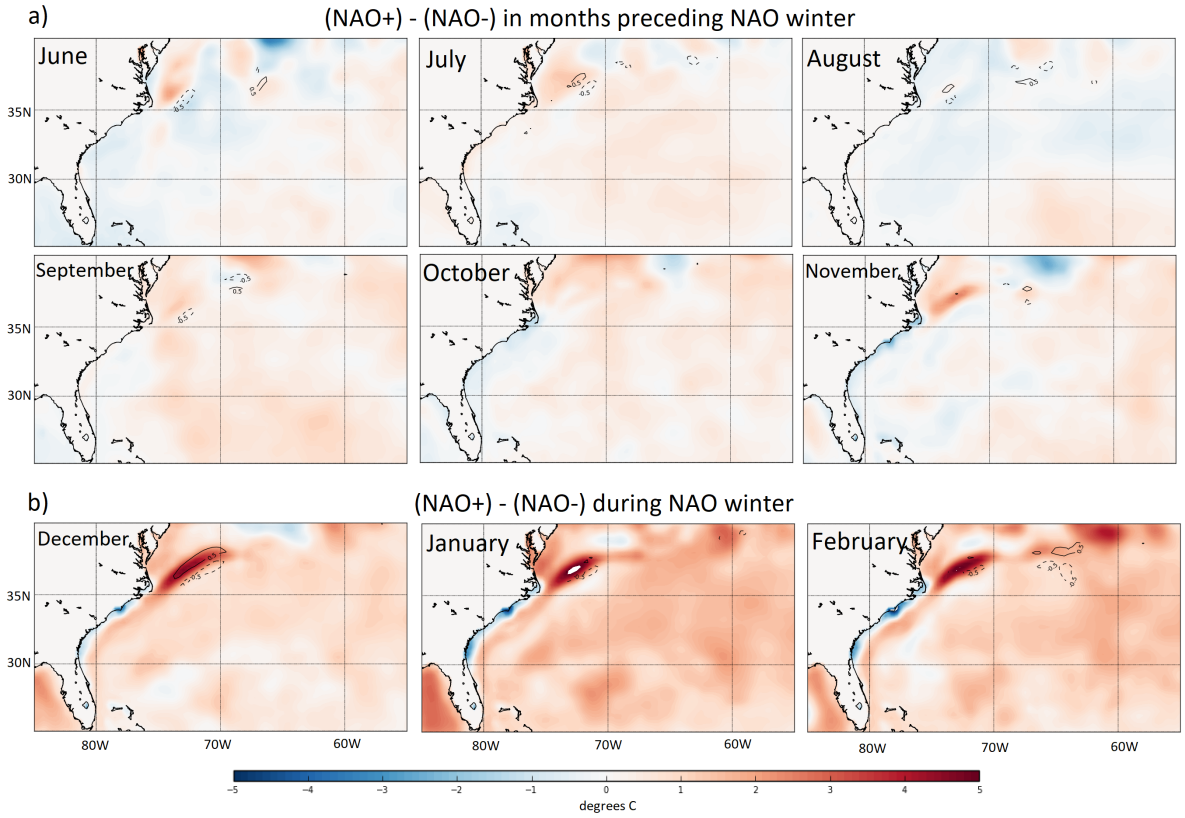


Fig. 5.12 Monthly analysis of the difference in SST between positive and negative NAO years (colour) and surface currents (black lines). Solid black lines are 0.5 m/s and dashed lines are -0.5 m/s. a) Months preceding NAO positive or negative winter (June-November). The years are 2009, 2010 for NAO- and 2011, 2013, 2014, 2015, 2016 for NAO+. b) Months during NAO positive or negative winter (December-February). The years for December as those listed above, and the years for January and February are 2010, 2011 for NAO- and 2012, 2014, 2015, 2016, 2017 for NAO+.

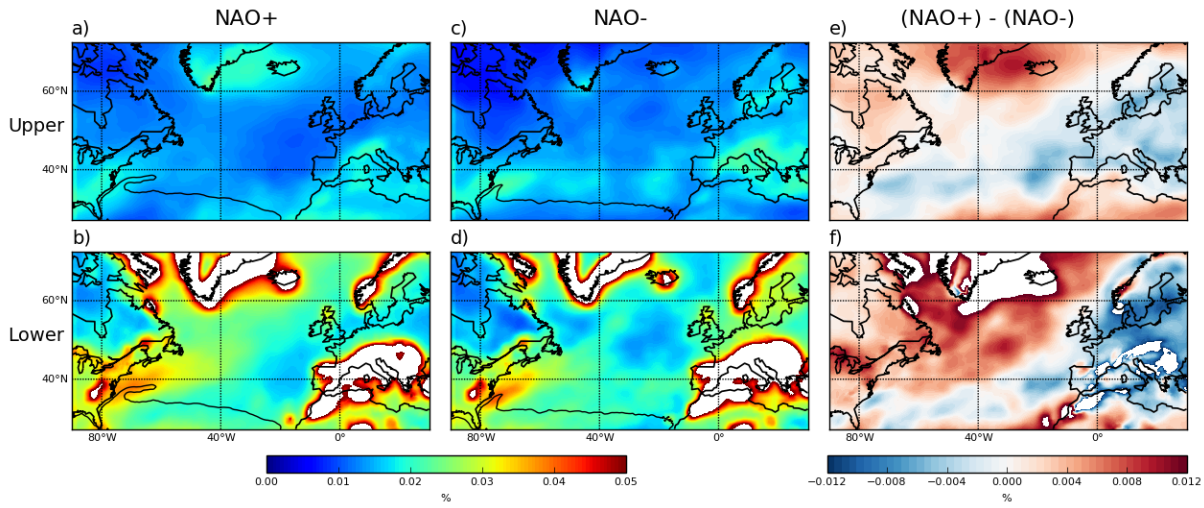


Fig. 5.13 Mesoscale kinetic energy (MKE) as a percentage of eddy kinetic energy (EKE), integrated over the upper atmosphere (300-600 hPa) in (a) positive (c) and negative NAO phases and the lower atmosphere (625-925 hPa) in (b) positive (d) and negative NAO phases. The difference between percentage contribution of MKE to EKE in positive and negative NAO winters is displayed in (e) upper atmosphere and (f) lower atmosphere. The 21 °C SST isotherm is shown in black contours in panels a,b,c,d. At positive saturation, white is shown.

injection of negative potential vorticity (PV) air at high levels. It has also been proposed by numerous studies that PV anomalies associated with extra-tropical cyclones can feedback onto the large scale (sections 4.1.2 & 5.1). For example, negative PV can be found in the cold sector of extra-tropical cyclones, and can affect blocking frequency and lifetime, reinforcing the anticyclonic circulation of a block (e.g. Pfahl et al., 2015). However, in this study, there is a higher frequency of $PV < 0$ extending north-eastwards from the Gulf Stream warm tongue region in NAO+. This is the direction of travel of extra-tropical storms, and upstream of the blocking areas. This appears to contradict the hypothesis that $PV < 0$ will maintain the blocking, related to NAO-. Alternatively, the mesoscale activity might strengthen the PV front in NAO+ by injecting low PV at the right place (see isentropic PV gradient in figure 5.7) and so feedback positively on NAO+, and in NAO- it might reinforce the NAO- by injecting low PV in the range of latitude where there is low PV. This hypothesis warrants further investigation through a modelling study at high resolution (at least 0.25°) run for climatological time scales.

The focus of this study is on the mesoscale kinetic energy (MKE) and its production terms (shear and buoyancy), however, it is interesting to examine the magnitude of MKE compared to the eddy kinetic energy (EKE). In the calculation for MKE (equation 4.1), the prime and bar terms were calculated using the low and high pass filter for mesoscales

(section 5.4). For EKE, the prime was calculated by taking the departure of from the time mean (DJF, as in figure 5.2), and the bar term is the time mean. These therefore both have the same units of m^2s^{-2} or Jkg^{-1} for values on a level, and kJm^{-2} when integrated over pressure levels. Once integrated over the upper and lower levels, the contribution of MKE as a percentage of EKE was calculated (figure 5.13). MKE contributes most to EKE in the lower levels over the Gulf Stream warm tongue region, making up approximately 0.04% over 625-925 hPa. The contribution of MKE to EKE over the upper levels (300-600 hPa) is around half this value. When comparing this percentage between the two NAO phases, we see the same signature over the warm tongue region that has been explored with previous variables. Although this percentage contribution to EKE is small, it is still an instability that is apparent in observations and suggested as important for characteristics of extra-tropical cyclones, including precipitation banding (see section 2.8.5). Although upright instability is routinely parametrised, this shear instability is missing from most climate models, and could have an effect on downstream blocking, which has been shown to be a cause of many forecast busts over Europe (Rodwell et al., 2013; Scaife et al., 2011).

Several studies have analysed in depth the relationship between NAO and Gulf Stream shift (e.g. Frankignoul et al., 2001; Sasaki and Schneider, 2011; Taylor and Stephens, 1998) and have emphasised that robustness is increased when the NAO leads the Gulf Stream by a year or two. This result was not reproduced in this study (not shown), but this likely reflects the persistent positive phase of the NAO since 2010 (our 5 NAO+ are nearly consecutive years), allowing time for the upper ocean to adjust.

5.7 Conclusions

This observational study uses high resolution reanalysis data (ERA5) to investigate mesoscale signatures of the North Atlantic Oscillation (NAO) in the atmosphere and ocean. The distribution of mesoscale buoyancy, shear production and negative potential vorticity (PV) in the atmosphere, along with sea surface temperature (SST) and surface currents in the ocean are described, and a difference with NAO phase is found. In positive NAO winters, embedded within the classic large-scale SST tripole is a warming and extension of the Gulf Stream warm tongue, along with a displacement and acceleration of surface currents. Mesoscale activity in the atmosphere appears to follow this extension of the warm tongue of the Gulf Stream. This appears to be a new feature of NAO air-sea interactions which is embedded within the basin scale NAO patterns (meridional shift of storm track, SST tripole) discussed previously in the literature. Further downstream mesoscale activity seems to reflect more passively the general poleward migration of synoptic activity in positive NAO conditions.

The analysis, although based on a short record with ERA5, is reproduced in the longer ERA-Interim dataset, albeit with a weaker magnitude.

The new mesoscale NAO signal highlighted in this study is consistent with the interpretation of forcing of the atmosphere by the ocean, in light of results by Sheldon et al. (2017), as opposed to the more dominant atmospheric forcing of the SST tripole on large (basin) spatial scale. Other studies have demonstrated this forcing is important in the western boundary current regions, such as the Gulf Stream, with an effect not just limited to the boundary layer (section 2.2.1). The positive NAO drives the tripole SST pattern and, presented here, also a strengthening of the Gulf Stream warm tongue. Such an SST distribution leads to more shear instability downstream of the warm tongue, opening the possibility of a positive feedback between the ocean and the NAO on scales smaller than those having been discussed so far in the literature. This behaviour has been proposed in previous studies, but until now has not been diagnosed in a high resolution reanalysis or with this shear instability. This hypothesis, and whether this mesoscale signal can affect the storm-track and its variability further downstream, remains to be investigated in future work.

In summary, this analysis shows the presence of previously unreported mesoscale signatures in the NAO, with the atmospheric feature anchored downstream of that in the ocean (figures 5.4 and 5.6).

The results of the studies in chapters 4, 5 and 6 will be discussed and summarised in the context of the overarching aim of this thesis. Open questions and future work will form the final chapter.

Chapter 6

Conclusions

6.1 Summary and discussion

This thesis has examined different aspects of the relationship between the ocean and the atmosphere on a variety of scales. This tropical cyclone study has revealed a robust empirical signal relating SST ~18 months prior to the typhoon season activity in a domain around southern China (chapter 3). However, using this SST signal alone does not provide a skilful statistical model for tropical cyclones within this domain. This is likely due to the importance of atmospheric processes, which are important for steering the cyclone, and are only predictable at lead times of a few months.

Chapter 4 sought to identify a mesoscale instability in a suite of model runs, reminiscent of Sheldon et al. (2017). This instability was present in all simulations, with resolution shown to not directly relate to intensity. Ensemble analysis also revealed a large spread between members, suggesting that the mechanism proposed by Sheldon et al. (2017), in which the SST influences this atmospheric instability, was not robust, or perhaps there was too much spread observed within the model atmosphere.

The climatological study in chapter 5 showed the importance of resolution for this mesoscale instability and also the effect of the underlying SST. While previous studies have examined the North Atlantic Oscillation (NAO) large-scale tripole in SST, the final study has shown a smaller scale feature embedded within. This local signal was shown to only be present when the SST was able to resolve the small scales of the Gulf Stream SST. The new mesoscale NAO signal highlighted in this study is reflecting a forcing of the atmosphere by the ocean, as opposed to the more dominant atmospheric forcing of the SST tripole on large (basin) spatial scale. This hypothesis, and whether this mesoscale signal can affect the storm-track and its variability further downstream, remains to be investigated in future work.

Chapter 3 revealed a robust empirical relationship and it would be interesting to further explore the mechanisms behind this. Such observational studies are useful to explore the relationships, but a modelling study with a coupled model is required to determine the processes at play. Any statistical analysis on tropical cyclone activity is limited by the length of the observational records (section 2.6), and by focussing on landfalling storms, the period analysed can be extended further back in time as it is likely that few storms will be missing from the records. However, this will reduce an already small sample by restricting the domain, especially if dividing by category, with only approximately 26 tropical cyclones per year in the western North Pacific (Zhan et al., 2012). To further examine the predictability of tropical cyclones at a long lead time or over a domain, a GCM would be ideal as it could provide a large enough sample to conduct a robust analysis, including the ability to investigate decadal signals such as the PDO.

The fundamental limitation of the study in chapter 4 was the analysis of a single storm. This storm was chosen as it has previously been examined in the motivating study (Sheldon et al., 2017). This storm was in 2004 and so the operational forecast at the time had a resolution of 0.4°. Since 2017, the operational forecast resolution has been 0.1°, higher than any datasets analysed, and the 51 member operational ensemble at this time was 0.2°, and so it would be useful to examine a more recent storm with this dataset. The Sheldon et al. (2017) study used a control and a smooth warm tongue, but my analysis used realistic SSTs (much like the control). In examining more storms, ideally characteristics of the warm tongue would be analysed, so that storms passing over SSTs with varying gradients could be compared. Chapter 5 showed that the warm tongue does vary, particularly in relation to NAO. Therefore, analysing storms from different NAO years would be a good starting point.

The length of the ERA5 reanalysis dataset used for chapter 5 is currently restricted to 2008 to present, and in the beginning of 2019 further years (back to 1950) will be released. Increasing the sample size of NAO years in this dataset would be valuable, and the effect of changing the SST boundary condition could be examined, as it changed from HadISST2 (0.25°) in 2007, to OSTIA (0.05°) thereafter (Hirahara et al., 2016). It has been shown that extra-tropical cyclones can have an effect on blocking (section 5.1), and so this could be explored in further analysis. Using more *PV* diagnostics and trajectory analysis could help to identify the exact mechanism whereby this relationship found in this study is originating from, and feeding back onto the large-scale.

6.2 Perspectives

I have proposed that the mesoscale process of shear instability is missing in climate models, which have a horizontal resolution in the atmosphere of 80-310 km and vertical resolution ranging from about 20 to 80 levels (CMIP5 models) (Zappa et al., 2013a). Results in chapters 4 and 5 have shown that this instability is apparent and is related to the NAO. I therefore suggest that the absence of this process, which is not parametrised nor resolved, can have a detrimental effect on the downstream forecast. It has been shown in previous work (Lindstrom and Nordeng, 1992) that including this parametrisation within a model improves forecast skill, and so whilst this is not resolved in climate models, there should be research into developing a parametrisation as well as understanding what the effect of this missing process has on forecasts on all time scales. Blocking over western Europe is a large source of error in climate models and is affected by the upstream position and strength of the storm track (de Vries et al., 2013; Luo et al., 2010; Woollings et al., 2008). Therefore, this missing process examined, modulated by ocean-atmosphere interactions over the Gulf Stream, may affect downstream forecasts of blocking episodes.

In figure 1.1, the ocean was treated as 'additional complexity', however, this analysis has shown that the ocean is a fundamental part of the climate system, influencing it and being influenced by it on a variety of scales, as has been found in previous studies (e.g Scaife et al., 2011; Woollings et al., 2012). Therefore, it should be included in the fundamental part of climate modelling, with the same care as the atmosphere. For both the atmospheric model and the oceanic model, horizontal and vertical resolution are important. For such small scale instabilities as those that have been investigated, fine vertical as well as horizontal resolution is required as the aspect ratio of the grid compared with the characteristic slope of the flow is central in determining the flow that can be properly represented (Lean and Clark, 2003). The aspect ratio of many mesoscale systems scales as U/fH, where U is an upper tropospheric velocity scale, f is the Coriolis parameter and H is a tropospheric depth scale. This is of order 30 or so, so that the vertical grid spacing should be roughly 30 times less than the horizontal spacing. The substantial benefits in refining both horizontal and vertical resolution give some support to scaling arguments deduced from quasi-geostrophic theory implying that horizontal and vertical resolution ought to be chosen consistently (Roeckner et al., 2006). Lean and Clark (2003) found that a 24 km 45-level model is sufficient to represent the overall frontal structure, but approximately 100 vertical levels and a 2 km horizontal grid length are needed to resolve the slantwise circulations in the frontal zone. The change of vertical resolution could affect precipitation partitioning between convective- and grid-scale as well as the vertical profiles of convection-related quantities such as temperature, humidity, clouds, convective heating and drying, and entrainment and detrainment (Xie et al., 2017).

The UK Met Office Unified Model in the Global Coupled 2 (GC2) configuration has a warm bias of up to almost 7 K in the Gulf Stream SSTs in the winter season, and the dynamical response is to enhance vertical motion in the transient eddies over the Gulf Stream, with local as well as remote effects via a planetary Rossby wave response (Lee et al., 2018). In this region with intense ocean-atmosphere interaction, this model is unable to correctly respond to variability or changes in the Gulf Stream. As shown in previous chapters, mesoscale activity in the Gulf Stream is important for processes within the atmosphere and perhaps whilst this bias is present, flux corrected models should be considered. There is a large signal-noise ratio error in regions associated with the NAO (chapter 1), possibly due to a missing signal from the ocean. With correct representation of the Gulf Stream, it is possible that this signal-noise ratio will be increased.

References

Alexander, M. A., Deser, C., and Timlin, M. S. (1999). The reemergence of SST anomalies in the North Pacific Ocean. *Journal of climate*, 12(8):2419–2433.

Ba, J., Keenlyside, N. S., Latif, M., Park, W., Ding, H., Lohmann, K., Mignot, J., Menary, M., Otterå, O. H., Wouters, B., et al. (2014). A multi-model comparison of Atlantic multidecadal variability. *Climate dynamics*, 43(9-10):2333–2348.

Baker, L., Shaffrey, L., Sutton, R., Weisheimer, A., and Scaife, A. (2018). An intercomparison of skill and overconfidence/underconfidence of the wintertime North Atlantic Oscillation in multimodel seasonal forecasts. *Geophysical Research Letters*, 45(15):7808–7817.

Balmaseda, M. A., Mogensen, K., and Weaver, A. T. (2013). Evaluation of the ECMWF ocean reanalysis system ORAS4. *Quarterly Journal of the Royal Meteorological Society*, 139(674):1132–1161.

Bender, M. A. and Ginis, I. (2000). Real-case simulations of hurricane-ocean interaction using a high-resolution coupled model: Effects on hurricane intensity. *Monthly Weather Review*, 128(4):917–946.

Bender, M. A., Ginis, I., and Kurihara, Y. (1993). Numerical simulations of tropical cyclone-ocean interaction with a high-resolution coupled model. *Journal of Geophysical Research: Atmospheres (1984–2012)*, 98(D12):23245–23263.

Bender, M. A., Knutson, T. R., Tuleya, R. E., Sirutis, J. J., Vecchi, G. A., Garner, S. T., and Held, I. M. (2010). Modeled impact of anthropogenic warming on the frequency of intense Atlantic hurricanes. *Science*, 327(5964):454–458.

Bengtsson, L., Hodges, K. I., Esch, M., Keenlyside, N., Kornblueh, L., LUO, J.-J., and Yamagata, T. (2007). How may tropical cyclones change in a warmer climate? *Tellus A*, 59(4):539–561.

Bennetts, D. and Hoskins, B. (1979). Conditional symmetric instability-a possible explanation for frontal rainbands. *Quarterly Journal of the Royal Meteorological Society*, 105(446):945–962.

Bjerknes, J. (1922). Life cycle of cyclones and the polar front theory of atmospheric circulation. *Geophys. Publik.*, 3(1):1–18.

Bjerknes, J. (1964). Atlantic air-sea interaction. In *Advances in geophysics*, volume 10, pages 1–82. Elsevier.

Blackmon, M. L. (1976). A climatological spectral study of the 500 mb geopotential height of the northern hemisphere. *Journal of the Atmospheric Sciences*, 33(8):1607–1623.

Boddy, R. and Smith, G. (2009). *Statistical methods in practice: for scientists and technologists*. John Wiley & Sons.

Bonjean, F. and Lagerloef, G. S. (2002). Diagnostic model and analysis of the surface currents in the tropical Pacific Ocean. *Journal of Physical Oceanography*, 32(10):2938–2954.

Booth, J. F., Thompson, L., Patoux, J., and Kelly, K. A. (2012). Sensitivity of midlatitude storm intensification to perturbations in the sea surface temperature near the Gulf Stream. *Monthly Weather Review*, 140(4):1241–1256.

Booth, J. F., Thompson, L. A., Patoux, J., Kelly, K. A., and Dickinson, S. (2010). The signature of the midlatitude tropospheric storm tracks in the surface winds. *Journal of Climate*, 23(5):1160–1174.

Bryan, F. O., Tomas, R., Dennis, J. M., Chelton, D. B., Loeb, N. G., and McClean, J. L. (2010). Frontal scale air–sea interaction in high-resolution coupled climate models. *Journal of Climate*, 23(23):6277–6291.

Camargo, S. J., Robertson, A. W., Gaffney, S. J., Smyth, P., and Ghil, M. (2007). Cluster analysis of typhoon tracks. Part II: Large-scale circulation and ENSO. *Journal of Climate*, 20(14):3654–3676.

Camp, J., Roberts, M., MacLachlan, C., Wallace, E., Hermanson, L., Brookshaw, A., Arribas, A., and Scaife, A. (2015). Seasonal forecasting of tropical storms using the Met Office GloSea5 seasonal forecast system. *Quarterly Journal of the Royal Meteorological Society*, 141(691):2206–2219.

Carr III, L. and Elsberry, R. L. (1990). Observational evidence for predictions of tropical cyclone propagation relative to environmental steering. *Journal of the Atmospheric Sciences*, 47(4):542–546.

Catto, J. L., Shaffrey, L. C., and Hodges, K. I. (2010). Can climate models capture the structure of extratropical cyclones? *Journal of Climate*, 23(7):1621–1635.

Cawley, G. C. and Talbot, N. L. (2010). On over-fitting in model selection and subsequent selection bias in performance evaluation. *Journal of Machine Learning Research*, 11(Jul):2079–2107.

Cayan, D. R. (1992). Latent and sensible heat flux anomalies over the northern oceans: Driving the sea surface temperature. *Journal of Physical Oceanography*, 22(8):859–881.

Chagnon, J., Gray, S., and Methven, J. (2013). Diabatic processes modifying potential vorticity in a North Atlantic cyclone. *Quarterly Journal of the Royal Meteorological Society*, 139(674):1270–1282.

Challinor, A. J., Osborne, T., Morse, A., Shaffrey, L., Wheeler, T., Weller, H., and Vidale, P. L. (2009). Methods and resources for climate impacts research: achieving synergy. *Bulletin of the American Meteorological Society*, 90(6):836–848.

Chan, J. C. (1985). Identification of the steering flow for tropical cyclone motion from objectively analyzed wind fields. *Monthly weather review*, 113(1):106–116.

Chan, J. C. (2000). Tropical cyclone activity over the western North Pacific associated with El Niño and La Niña events. *Journal of Climate*, 13(16):2960–2972.

Chan, J. C. (2005). The physics of tropical cyclone motion. *Annu. Rev. Fluid Mech.*, 37:99–128.

Chan, J. C. (2007). Interannual variations of intense typhoon activity. *Tellus A*, 59(4):455–460.

Chan, J. C. and Gray, W. M. (1982). Tropical cyclone movement and surrounding flow relationships. *Monthly Weather Review*, 110(10):1354–1374.

Chan, J. C., Shi, J.-e., and Lam, C.-m. (1998). Seasonal forecasting of tropical cyclone activity over the western North Pacific and the South China Sea. *Weather and forecasting*, 13(4):997–1004.

Chen, S. S., Zhao, W., Donelan, M. A., Price, J. F., and Walsh, E. J. (2007). The cblast-hurricane program and the next-generation fully coupled atmosphere-wave-ocean models for hurricane research and prediction. *Bulletin of the American Meteorological Society*, 88(3):311–317.

Church, J. A., Clark, P. U., Cazenave, A., Gregory, J. M., Jevrejeva, S., Levermann, A., Merrifield, M., Milne, G., Nerem, R., Nunn, P., et al. (2013). Sea level change. *Climate change*, pages 1137–1216.

Chylek, P., Folland, C. K., Dijkstra, H. A., Lesins, G., and Dubey, M. K. (2011). Ice-core data evidence for a prominent near 20 year time-scale of the Atlantic Multidecadal Oscillation. *Geophysical Research Letters*, 38(13).

CL Chan, J., Shi, J.-e., and Liu, K. S. (2001). Improvements in the seasonal forecasting of tropical cyclone activity over the western North Pacific. *Weather and forecasting*, 16(4):491–498.

Cronin, M. F., Bond, N., Booth, J., Ichikawa, H., Joyce, T. M., Kelly, K., Kubota, M., Qiu, B., Reason, C., Rouault, M., et al. (2010). Monitoring ocean-atmosphere interactions in western boundary current extensions. *Proceedings of the OceanObs*, 9.

Czaja, A. and Blunt, N. (2011). A new mechanism for ocean–atmosphere coupling in midlatitudes. *Quarterly Journal of the Royal Meteorological Society*, 137(657):1095–1101.

Czaja, A. and Frankignoul, C. (2002). Observed impact of Atlantic SST anomalies on the North Atlantic Oscillation. *Journal of Climate*, 15(6):606–623.

Czaja, A. and Marshall, J. (2001). Observations of atmosphere-ocean coupling in the North Atlantic. *Quarterly Journal of the Royal Meteorological Society*, 127(576):1893–1916.

Dare, R. A. and McBride, J. L. (2011). The threshold sea surface temperature condition for tropical cyclogenesis. *Journal of climate*, 24(17):4570–4576.

D'Asaro, E., Black, P., Centurioni, L., Chang, Y.-T., Chen, S. S., Foster, R., Graber, H. C., Harr, P., Hormann, V., Lien, R.-C., et al. (2014). Impact of typhoons on the ocean in the Pacific. *Bulletin of the American Meteorological Society*, 95(9):1405–1418.

de Vries, H., Woollings, T., Anstey, J., Haarsma, R. J., and Hazeleger, W. (2013). Atmospheric blocking and its relation to jet changes in a future climate. *Climate dynamics*, 41(9-10):2643–2654.

Dee, D., Uppala, S., Simmons, A., Berrisford, P., Poli, P., Kobayashi, S., Andrae, U., Balmaseda, M., Balsamo, G., Bauer, P., et al. (2011). The ERA-Interim reanalysis: Configuration and performance of the data assimilation system. *Quarterly Journal of the Royal Meteorological Society*, 137(656):553–597.

Delworth, T., Manabe, S., and Stouffer, R. (1993). Interdecadal variations of the thermohaline circulation in a coupled ocean-atmosphere model. *Journal of Climate*, 6(11):1993–2011.

Deser, C. and Blackmon, M. L. (1993). Surface climate variations over the North Atlantic Ocean during winter: 1900–1989. *Journal of Climate*, 6(9):1743–1753.

Donlon, C. J., Martin, M., Stark, J., Roberts-Jones, J., Fiedler, E., and Wimmer, W. (2012). The operational sea surface temperature and sea ice analysis (OSTIA) system. *Remote Sensing of Environment*, 116:140–158.

Dunnavan, G. M. and Diercks, J. W. (1980). An analysis of super typhoon Tip (October 1979). *Monthly Weather Review*, 108(11):1915–1923.

Dunstone, N., Smith, D., Scaife, A., Hermanson, L., Eade, R., Robinson, N., Andrews, M., and Knight, J. (2016). Skilful predictions of the winter North Atlantic Oscillation one year ahead. *Nature Geoscience*, 9(11):809.

Eade, R., Smith, D., Scaife, A., Wallace, E., Dunstone, N., Hermanson, L., and Robinson, N. (2014). Do seasonal-to-decadal climate predictions underestimate the predictability of the real world? *Geophysical research letters*, 41(15):5620–5628.

Eady, E. T. (1949). Long waves and cyclone waves. *Tellus*, 1(3):33–52.

ECMWF (2016). New forecast model cycle brings highest-ever resolution. www.ecmwf.int/en/about/media-centre/news/2016/new-forecast-model-cycle-brings-highest-ever-resolution. Accessed: 12-03-2016.

ECMWF (2017). Modeling and prediction. Atmospheric Dynamics. www.ecmwf.int/en/research/modelling-and-prediction/atmospheric-dynamics. Accessed: 02-04-2017.

Eliassen, A. (1962). On the vertical circulation in frontal zones. *Geofys. publ*, 24(4):147–160.

Elmore, K. L., Baldwin, M. E., and Schultz, D. M. (2006). Field significance revisited: spatial bias errors in forecasts as applied to the Eta model. *Monthly weather review*, 134(2):519–531.

Elsner, J. B., Kossin, J. P., and Jagger, T. H. (2008). The increasing intensity of the strongest tropical cyclones. *Nature*, 455(7209):92–95.

Emanuel, K. (2003). Tropical cyclones. *Annual Review of Earth and Planetary Sciences*, 31(1):75–104.

Emanuel, K. (2005). Increasing destructiveness of tropical cyclones over the past 30 years. *Nature*, 436(7051):686–688.

Emanuel, K., Sundararajan, R., and Williams, J. (2008). Hurricanes and global warming: Results from downscaling IPCC AR4 simulations. *Bulletin of the American Meteorological Society*, 89(3):347–367.

Emanuel, K. A. (1983). On assessing local conditional symmetric instability from atmospheric soundings. *Monthly weather review*, 111(10):2016–2033.

Emanuel, K. A. (1991). The theory of hurricanes. *Annual Review of Fluid Mechanics*, 23(1):179–196.

Feldstein, S. B. (2000). The timescale, power spectra, and climate noise properties of teleconnection patterns. *Journal of Climate*, 13(24):4430–4440.

Fowler, A. and Hennessy, K. (1995). Potential impacts of global warming on the frequency and magnitude of heavy precipitation. *Natural Hazards*, 11(3):283–303.

Frankignoul, C., Czaja, A., and L'Heveder, B. (1998). Air–sea feedback in the North Atlantic and surface boundary conditions for ocean models. *Journal of climate*, 11(9):2310–2324.

Frankignoul, C., de Coëtlogon, G., Joyce, T. M., and Dong, S. (2001). Gulf Stream variability and ocean–atmosphere interactions. *Journal of physical Oceanography*, 31(12):3516–3529.

Frankignoul, C. and Hasselmann, K. (1977). Stochastic climate models, Part II Application to sea-surface temperature anomalies and thermocline variability. *Tellus*, 29(4):289–305.

Fudeyasu, H., Hirose, S., Yoshioka, H., Kumazawa, R., and Yamasaki, S. (2014). A global view of the landfall characteristics of tropical cyclones. *Trop. Cyclone Res. Rev*, 3:178–192.

Gaspar, P., Grégoris, Y., and Lefevre, J.-M. (1990). A simple eddy kinetic energy model for simulations of the oceanic vertical mixing: Tests at station Papa and Long-Term Upper Ocean Study site. *Journal of Geophysical Research: Oceans*, 95(C9):16179–16193.

Gastineau, G., Mignot, J., Arzel, O., and Huck, T. (2018). North Atlantic Ocean Internal Decadal Variability: Role of the Mean State and Ocean-Atmosphere Coupling. *Journal of Geophysical Research: Oceans*, 123(8):5949–5970.

Gentry, M. S. and Lackmann, G. M. (2010). Sensitivity of simulated tropical cyclone structure and intensity to horizontal resolution. *Monthly Weather Review*, 138(3):688–704.

Gerber, E. P. and Vallis, G. K. (2007). Eddy–zonal flow interactions and the persistence of the zonal index. *Journal of the Atmospheric Sciences*, 64(9):3296–3311.

Gray, W. M. (1984). Atlantic seasonal hurricane frequency. Part II: Forecasting its variability. *Monthly Weather Review*, 112(9):1669–1683.

Hall, R., Erdélyi, R., Hanna, E., Jones, J. M., and Scaife, A. A. (2015). Drivers of North Atlantic polar front jet stream variability. *International Journal of Climatology*, 35(8):1697–1720.

Hayes, S., McPhaden, M., and Wallace, J. (1989). The influence of sea-surface temperature on surface wind in the eastern equatorial pacific: Weekly to monthly variability. *Journal of Climate*, 2(12):1500–1506.

Hill, K. A. and Lackmann, G. M. (2011). The impact of future climate change on TC intensity and structure: A downscaling approach. *Journal of Climate*, 24(17):4644–4661.

Hirahara, S., Balmaseda, M. A., de Boisseson, E., and Hersbach, H. (2016). Sea Surface Temperature and Sea Ice Concentration for ERA5. Technical report, ECMWF.

Hirata, H. and Kawamura, R. (2014). Scale interaction between typhoons and the North Pacific subtropical high and associated remote effects during the Baiu/Meiyu season. *Journal of Geophysical Research: Atmospheres*, 119(9):5157–5170.

Holland, G. J. (1997). The maximum potential intensity of tropical cyclones. *Journal of the atmospheric sciences*, 54(21):2519–2541.

Holton, J. (2004). An introduction to dynamic meteorology. *Burlington, MA: Elsevier*.

Holton, J. R. and Hakim, G. J. (2012). *An introduction to dynamic meteorology*, volume 88. Academic press.

Horn, M., Walsh, K., Zhao, M., Camargo, S. J., Scoccimarro, E., Murakami, H., Wang, H., Ballinger, A., Kumar, A., Shaevitz, D. A., et al. (2014). Tracking scheme dependence of simulated tropical cyclone response to idealized climate simulations. *Journal of Climate*, 27(24):9197–9213.

Hoskins, B. J., James, I. N., and White, G. H. (1983). The shape, propagation and mean-flow interaction of large-scale weather systems. *Journal of the atmospheric sciences*, 40(7):1595–1612.

Hoskins, B. J. and Revell, M. J. (1981). The most unstable long wavelength baroclinic instability modes. *Journal of the Atmospheric Sciences*, 38(7):1498–1503.

Hoskins, B. J. and Valdes, P. J. (1990). On the existence of storm-tracks. *Journal of the atmospheric sciences*, 47(15):1854–1864.

Huang, B., Banzon, V. F., Freeman, E., Lawrimore, J., Liu, W., Peterson, T. C., Smith, T. M., Thorne, P. W., Woodruff, S. D., and Zhang, H.-M. (2015). Extended Reconstructed Sea Surface Temperature Version 4 (ERSST. v4). Part I: Upgrades and Intercomparisons. *Journal of Climate*, 28(3):911–930.

Hurrell, J. W., Kushnir, Y., Ottersen, G., and Visbeck, M. (2003). An overview of the North Atlantic Oscillation. *The North Atlantic Oscillation: climatic significance and environmental impact*, 134:1–35.

Joos, H. and Wernli, H. (2012). Influence of microphysical processes on the potential vorticity development in a warm conveyor belt: A case-study with the limited-area model COSMO. *Quarterly Journal of the Royal Meteorological Society*, 138(663):407–418.

Jung, T., Gulev, S., Rudeva, I., and Soloviov, V. (2006). Sensitivity of extratropical cyclone characteristics to horizontal resolution in the ECMWF model. *Quarterly Journal of the Royal Meteorological Society*, 132(619):1839–1857.

Kelly, K. A., Small, R. J., Samelson, R., Qiu, B., Joyce, T. M., Kwon, Y.-O., and Cronin, M. F. (2010). Western boundary currents and frontal air–sea interaction: Gulf Stream and Kuroshio Extension. *Journal of Climate*, 23(21):5644–5667.

Keyser, D. and Shapiro, M. (1990). Fronts, jet streams and the tropopause. *Extratropical Cyclones: The Erik Palmén Memorial Volume*, pages 167–191.

Kidston, J., Frierson, D., Renwick, J., and Vallis, G. K. (2010). Observations, simulations, and dynamics of jet stream variability and annular modes. *Journal of Climate*, 23(23):6186–6199.

Kim, J.-H., Ho, C.-H., Kim, H.-S., Sui, C.-H., and Park, S. K. (2008). Systematic variation of summertime tropical cyclone activity in the western North Pacific in relation to the Madden-Julian oscillation. *Journal of Climate*, 21(6):1171–1191.

Knapp, K. R., Knaff, J. A., Sampson, C. R., Riggio, G. M., and Schnapp, A. D. (2013). A pressure-based analysis of the historical western North Pacific tropical cyclone intensity record. *Monthly Weather Review*, 141(8):2611–2631.

Knapp, K. R., Kruk, M. C., Levinson, D. H., Diamond, H. J., and Neumann, C. J. (2010). The international best track archive for climate stewardship (IBTrACS) unifying tropical cyclone data. *Bulletin of the American Meteorological Society*, 91(3):363–376.

Knight, J. R., Allan, R. J., Folland, C. K., Vellinga, M., and Mann, M. E. (2005). A signature of persistent natural thermohaline circulation cycles in observed climate. *Geophysical Research Letters*, 32(20).

Knutson, T. R., McBride, J. L., Chan, J., Emanuel, K., Holland, G., Landsea, C., Held, I., Kossin, J. P., Srivastava, A., and Sugi, M. (2010). Tropical cyclones and climate change. *Nature Geoscience*, 3(3):157–163.

Kobayashi, S., Ota, Y., Harada, Y., Ebita, A., Moriya, M., Onoda, H., Onogi, K., Kamahori, H., Kobayashi, C., Endo, H., et al. (2015). The JRA-55 reanalysis: General specifications and basic characteristics. *Journal of the Meteorological Society of Japan. Ser. II Vol. 93 (2015) No. 1 p. 5-48*, 93(1):5–48.

Kushnir, Y., Robinson, W., Bladé, I., Hall, N., Peng, S., and Sutton, R. (2002). Atmospheric GCM response to extratropical SST anomalies: Synthesis and evaluation. *Journal of Climate*, 15(16):2233–2256.

Kwon, Y.-O., Alexander, M. A., Bond, N. A., Frankignoul, C., Nakamura, H., Qiu, B., and Thompson, L. A. (2010). Role of the Gulf Stream and Kuroshio–Oyashio systems in large-scale atmosphere–ocean interaction: A review. *Journal of Climate*, 23(12):3249–3281.

Lander, M. A. (1994). An exploratory analysis of the relationship between tropical storm formation in the western North Pacific and ENSO. *Monthly Weather Review*, 122(4):636–651.

Lander, M. A. (1996). Specific tropical cyclone track types and unusual tropical cyclone motions associated with a reverse-oriented monsoon trough in the western North Pacific. *Weather and Forecasting*, 11(2):170–186.

Landsea, C. (2007). Counting Atlantic tropical cyclones back to 1900. *Eos, Transactions American Geophysical Union*, 88(18):197–202.

Landsea, C. and Franklin, J. (2013). How 'good' are the best tracks? Estimating uncertainty in the Atlantic hurricane database. *Mon. Weather Rev*, 141:3576–3592.

Landsea, C. W. (2000). Climate variability of tropical cyclones: past, present and future. *Storms. Routledge, New York*, pages 220–241.

Landsea, C. W., Anderson, C., Charles, N., Clark, G., Dunion, J., Fernandez-Partagas, J., Hungerford, P., Neumann, C., and Zimmer, M. (2004). The Atlantic hurricane database re-analysis project: Documentation for the 1851–1910 alterations and additions to the HURDAT database. *Hurricanes and Typhoons: Past, Present and Future*, pages 177–221.

Lau, N.-C. and Wallace, J. M. (1979). On the distribution of horizontal transports by transient eddies in the northern hemisphere wintertime circulation'. *Journal of the Atmospheric Sciences*, 36(10):1844–1861.

Lean, H. W. and Clark, P. A. (2003). The effects of changing resolution on mesocale modelling of line convection and slantwise circulations in FASTEX IOP16. *Quarterly Journal of the Royal Meteorological Society*, 129(592):2255–2278.

Lee, R. W., Woollings, T. J., Hoskins, B. J., Williams, K. D., O'Reilly, C. H., and Masato, G. (2018). Impact of Gulf Stream SST biases on the global atmospheric circulation. *Climate Dynamics*, pages 1–19.

Liebmann, B., Hendon, H. H., and Glick, J. D. (1994). The relationship between tropical cyclones of the western Pacific and Indian Oceans and the Madden-Julian oscillation. *Journal of the Meteorological Society of Japan*, 72(3):401–412.

Lin, I., Pun, I.-F., and Wu, C.-C. (2009). Upper-ocean thermal structure and the western North Pacific category 5 typhoons. Part II: Dependence on translation speed. *Monthly Weather Review*, 137(11):3744–3757.

Lin, I., Wu, C.-C., Pun, I.-F., and Ko, D.-S. (2008). Upper-ocean thermal structure and the western North Pacific category 5 typhoons. Part I: Ocean features and the category 5 typhoons' intensification. *Monthly Weather Review*, 136(9):3288–3306.

Lin, N., Emanuel, K., Oppenheimer, M., and Vanmarcke, E. (2012). Physically based assessment of hurricane surge threat under climate change. *Nature Climate Change*, 2(6):462–467.

Lindstrom, S. S. and Nordeng, T. E. (1992). Parameterized slantwise convection in a numerical model. *Monthly weather review*, 120(5):742–756.

Lindzen, R. S. and Nigam, S. (1987). On the role of sea surface temperature gradients in forcing low-level winds and convergence in the tropics. *Journal of the Atmospheric Sciences*, 44(17):2418–2436.

Liu, K. S. and Chan, J. C. (2008). Interdecadal variability of western North Pacific tropical cyclone tracks. *Journal of Climate*, 21(17):4464–4476.

Livezey, R. E. and Chen, W. (1983). Statistical field significance and its determination by Monte Carlo techniques. *Monthly Weather Review*, 111(1):46–59.

Lu, M.-M., Lee, C.-T., and Wang, B. (2013). Seasonal prediction of accumulated tropical cyclone kinetic energy around Taiwan and the sources of the predictability. *International Journal of Climatology*, 33(13):2846–2854.

Luo, D., Zhou, W., and Wei, K. (2010). Dynamics of eddy-driven North Atlantic Oscillations in a localized shifting jet: zonal structure and downstream blocking. *Climate dynamics*, 34(1):73.

Ma, X., Chang, P., Saravanan, R., Montuoro, R., Hsieh, J.-S., Wu, D., Lin, X., Wu, L., and Jing, Z. (2015). Distant influence of Kuroshio eddies on North Pacific weather patterns? *Scientific reports*, 5:17785.

Madonna, E., Wernli, H., Joos, H., and Martius, O. (2014). Warm conveyor belts in the ERA-Interim dataset (1979–2010). Part I: Climatology and potential vorticity evolution. *Journal of climate*, 27(1):3–26.

Manganello, J. V., Hodges, K. I., Cash, B. A., Kinter III, J. L., Altshuler, E. L., Fennessy, M. J., Vitart, F., Molteni, F., and Towers, P. (2016). Seasonal forecasts of tropical cyclone activity in a high-atmospheric-resolution coupled prediction system. *Journal of Climate*, 29(3):1179–1200.

Mantua, N. J., Hare, S. R., Zhang, Y., Wallace, J. M., and Francis, R. C. (1997). A Pacific interdecadal climate oscillation with impacts on salmon production. *Bulletin of the american Meteorological Society*, 78(6):1069–1080.

Marshall, J., Johnson, H., and Goodman, J. (2001). A study of the interaction of the North Atlantic Oscillation with ocean circulation. *Journal of Climate*, 14(7):1399–1421.

McBride, J. L. (1995). Tropical cyclone formation. *Global Perspectives on Tropical Cyclones*, 693(2):63–105.

McDonald, R. E., Bleaken, D. G., Cresswell, D. R., Pope, V. D., and Senior, C. A. (2005). Tropical storms: representation and diagnosis in climate models and the impacts of climate change. *Climate Dynamics*, 25(1):19–36.

McTaggart-Cowan, R., Davies, E. L., Fairman Jr, J. G., Galarneau Jr, T. J., and Schultz, D. M. (2015). Revisiting the 26.5C sea surface temperature threshold for tropical cyclone development. *Bulletin of the American Meteorological Society*, 96(11):1929–1943.

Menary, M. B., Hodson, D. L., Robson, J. I., Sutton, R. T., Wood, R. A., and Hunt, J. A. (2015). Exploring the impact of CMIP5 model biases on the simulation of North Atlantic decadal variability. *Geophysical Research Letters*, 42(14):5926–5934.

Merrill, R. (1993). Tropical cyclone structure. *Global guide to tropical cyclone forecasting*, pages 2–1.

Merrill, R. T. (1984). A comparison of large and small tropical cyclones. *Monthly Weather Review*, 112(7):1408–1418.

Minobe, S., Kuwano-Yoshida, A., Komori, N., Xie, S.-P., and Small, R. J. (2008). Influence of the Gulf Stream on the troposphere. *Nature*, 452(7184):206–209.

Molinari, J. and Vollaro, D. (2013). What percentage of western North Pacific tropical cyclones form within the monsoon trough? *Monthly Weather Review*, 141(2):499–505.

Molinari, J. and Vollaro, D. (2014). Symmetric instability in the outflow layer of a major hurricane. *Journal of the Atmospheric Sciences*, 71(10):3739–3746.

Morcrette, C. J. (2004). *Radar and modelling studies of upright and slantwise convection*. PhD thesis, University of Reading.

Munk, W. H. (1950). On the wind-driven ocean circulation. *Journal of meteorology*, 7(2):80–93.

Murakami, H., Wang, Y., Yoshimura, H., Mizuta, R., Sugi, M., Shindo, E., Adachi, Y., Yukimoto, S., Hosaka, M., Kusunoki, S., et al. (2012). Future changes in tropical cyclone activity projected by the new high-resolution MRI-AGCM. *Journal of Climate*, 25(9):3237–3260.

Nakamura, H., Sampe, T., Goto, A., Ohfuchi, W., and Xie, S.-P. (2008). On the importance of midlatitude oceanic frontal zones for the mean state and dominant variability in the tropospheric circulation. *Geophysical Research Letters*, 35(15).

Nakamura, H., Sampe, T., Tanimoto, Y., and Shimpo, A. (2004). Observed associations among storm tracks, jet streams and midlatitude oceanic fronts. *Earth's Climate*, pages 329–345.

Nakamura, H. and Wallace, J. M. (1990). Observed changes in baroclinic wave activity during the life cycles of low-frequency circulation anomalies. *Journal of the Atmospheric Sciences*, 47(9):1100–1116.

Newman, M., Alexander, M. A., Ault, T. R., Cobb, K. M., Deser, C., Di Lorenzo, E., Mantua, N. J., Miller, A. J., Minobe, S., Nakamura, H., et al. (2016). The Pacific decadal oscillation, revisited. *Journal of Climate*, 29(12):4399–4427.

Nicholls, N. (1979). A possible method for predicting seasonal tropical cyclone activity in the Australian region. *Monthly Weather Review*, 107(9):1221–1224.

Nicholls, N. (1985). Predictability of interannual variations of Australian seasonal tropical cyclone activity. *Monthly weather review*, 113(7):1144–1149.

O'Neill, L. W., Chelton, D. B., and Esbensen, S. K. (2010). The effects of sst-induced surface wind speed and direction gradients on midlatitude surface vorticity and divergence. *Journal of Climate*, 23(2):255–281.

Palmen, E. (1948). On the formation and structure of tropical hurricanes. *Geophysica*, 3(1):26–38.

Persson, A. (2015). User guide to ECMWF forecast products (ECMWF, version 1.2). Technical report, ECMWF.

Pfahl, S., Madonna, E., Boettcher, M., Joos, H., and Wernli, H. (2014). Warm conveyor belts in the ERA-Interim dataset (1979–2010). Part II: Moisture origin and relevance for precipitation. *Journal of Climate*, 27(1):27–40.

Pfahl, S., Schwierz, C., Croci-Maspoli, M., Grams, C. M., and Wernli, H. (2015). Importance of latent heat release in ascending air streams for atmospheric blocking. *Nature Geoscience*, 8(8):610.

Pinto, J. G., Zacharias, S., Fink, A. H., Leckebusch, G. C., and Ulbrich, U. (2009). Factors contributing to the development of extreme North Atlantic cyclones and their relationship with the NAO. *Climate dynamics*, 32(5):711–737.

Ranson, M., Kousky, C., Ruth, M., Jantarasami, L., Crimmins, A., and Tarquinio, L. (2014). Tropical and extratropical cyclone damages under climate change. *Climatic change*, 127(2):227–241.

Rayner, N., Parker, D. E., Horton, E., Folland, C., Alexander, L., Rowell, D., Kent, E., and Kaplan, A. (2003). Global analyses of sea surface temperature, sea ice, and night marine air temperature since the late nineteenth century. *Journal of Geophysical Research: Atmospheres*, 108(D14).

Reuter, G. and Yau, M. (1990). Observations of slantwise convective instability in winter cyclones. *Monthly Weather Review*, 118(2):447–458.

Reynolds, R. W., Rayner, N. A., Smith, T. M., Stokes, D. C., and Wang, W. (2002). An improved in situ and satellite SST analysis for climate. *Journal of climate*, 15(13):1609–1625.

Rhein, M., Rintoul, S., Aoki, S., Campos, E., Chambers, D., Feely, R., Gulev, S., Johnson, G., Josey, S., Kostianoy, A., et al. (2013). Chapter 3: Observations: Ocean. *Climate Change*.

Roberts, J., Champion, A., Dawkins, L., Hodges, K., Shaffrey, L., Stephenson, D., Stringer, M., Thornton, H., and Youngman, B. (2014). The XWS open access catalogue of extreme European windstorms from 1979 to 2012. *Natural Hazards and Earth System Sciences*, 14:2487–2501.

Roberts, M. J., Vidale, P. L., Mizielinski, M. S., Demory, M.-E., Schiemann, R., Strachan, J., Hodges, K., Bell, R., and Camp, J. (2015). Tropical Cyclones in the UPSCALE Ensemble of High-Resolution Global Climate Models. *Journal of Climate*, 28(2):574–596.

Rodwell, M. J., Magnusson, L., Bauer, P., Bechtold, P., Bonavita, M., Cardinali, C., Diamantakis, M., Earnshaw, P., Garcia-Mendez, A., Isaksen, L., et al. (2013). Characteristics of occasional poor medium-range weather forecasts for Europe. *Bulletin of the American Meteorological Society*, 94(9):1393–1405.

Roeckner, E., Brokopf, R., Esch, M., Giorgetta, M., Hagemann, S., Kornblueh, L., Manzini, E., Schlese, U., and Schulzweida, U. (2006). Sensitivity of simulated climate to horizontal and vertical resolution in the ECHAM5 atmosphere model. *Journal of Climate*, 19(16):3771–3791.

Roemmich, D. and Gilson, J. (2009). The 2004–2008 mean and annual cycle of temperature, salinity, and steric height in the global ocean from the Argo Program. *Progress in Oceanography*, 82(2):81–100.

Rohrer, M., Brönnimann, S., Martius, O., Raible, C. C., Wild, M., and Compo, G. P. (2018). Representation of extratropical cyclones, blocking anticyclones, and alpine circulation types in multiple reanalyses and model simulations. *Journal of Climate*, 31(8):3009–3031.

Rowell, D. P. (1998). Assessing potential seasonal predictability with an ensemble of multidecadal GCM simulations. *Journal of Climate*, 11(2):109–120.

Saha, S., Moorthi, S., Pan, H.-L., Wu, X., Wang, J., Nadiga, S., Tripp, P., Kistler, R., Woollen, J., Behringer, D., et al. (2010). The NCEP climate forecast system reanalysis. *Bulletin of the American Meteorological Society*, 91(8):1015–1057.

Sampe, T., Nakamura, H., Goto, A., and Ohfuchi, W. (2010). Significance of a midlatitude SST frontal zone in the formation of a storm track and an eddy-driven westerly jet. *Journal of Climate*, 23(7):1793–1814.

Sasaki, Y. N. and Schneider, N. (2011). Interannual to decadal Gulf Stream variability in an eddy-resolving ocean model. *Ocean Modelling*, 39(3-4):209–219.

Scaife, A., Arribas, A., Blockley, E., Brookshaw, A., Clark, R., Dunstone, N., Eade, R., Fereday, D., Folland, C., Gordon, M., et al. (2014). Skillful long-range prediction of European and North American winters. *Geophysical Research Letters*, 41(7):2514–2519.

Scaife, A. A., Copsey, D., Gordon, C., Harris, C., Hinton, T., Keeley, S., O'Neill, A., Roberts, M., and Williams, K. (2011). Improved Atlantic winter blocking in a climate model. *Geophysical Research Letters*, 38(23).

Scaife, A. A., Ineson, S., Knight, J. R., Gray, L., Kodera, K., and Smith, D. M. (2013). A mechanism for lagged North Atlantic climate response to solar variability. *Geophysical Research Letters*, 40(2):434–439.

Scaife, A. A. and Smith, D. (2018). A signal-to-noise paradox in climate science. *npj Climate and Atmospheric Science*, 1(1):28.

Scaife, A. A., Woollings, T., Knight, J., Martin, G., and Hinton, T. (2010). Atmospheric blocking and mean biases in climate models. *Journal of Climate*, 23(23):6143–6152.

Schultz, D. M. (2001). Reexamining the cold conveyor belt. *Monthly Weather Review*, 129(9):2205–2225.

Schultz, D. M., Keyser, D., and Bosart, L. F. (1998). The effect of large-scale flow on low-level frontal structure and evolution in midlatitude cyclones. *Monthly weather review*, 126(7):1767–1791.

Seltzer, M. A., Passarelli, R., and Emanuel, K. (1985). The possible role of symmetric instability in the formation of precipitation bands. *Journal of the atmospheric sciences*, 42(20):2207–2219.

Shabbar, A., Huang, J., and Higuchi, K. (2001). The relationship between the wintertime North Atlantic Oscillation and blocking episodes in the North Atlantic. *International Journal of Climatology*, 21(3):355–369.

Shaevitz, D. A., Camargo, S. J., Sobel, A. H., Jonas, J. A., Kim, D., Kumar, A., LaRow, T. E., Lim, Y.-K., Murakami, H., Reed, K. A., et al. (2014). Characteristics of tropical cyclones in high-resolution models in the present climate. *Journal of Advances in Modeling Earth Systems*, 6(4):1154–1172.

Shaman, J., Samelson, R., and Skyllingstad, E. (2010). Air–sea fluxes over the Gulf Stream region: Atmospheric controls and trends. *Journal of Climate*, 23(10):2651–2670.

Shay, L. K., Goni, G. J., and Black, P. G. (2000). Effects of a warm oceanic feature on Hurricane Opal. *Monthly Weather Review*, 128(5):1366–1383.

Sheldon, L., Czaja, A., Vannière, B., Morcrette, C., Sohet, B., Casado, M., and Smith, D. (2017). A 'warm path'for Gulf Stream–troposphere interactions. *Tellus A: Dynamic Meteorology and Oceanography*, 69(1):1299397.

Short, C. J. and Petch, J. (2018). How well can the Met Office Unified Model forecast tropical cyclones in the western North Pacific? *Weather and Forecasting*, 33(1):185–201.

Simpson, R. H. and Saffir, H. (1974). The hurricane disaster potential scale. *Weatherwise*, 27(8):169.

Small, R., Xie, S., O'Neill, L., Seo, H., Song, Q., Cornillon, P., Spall, M., Minobe, S., et al. (2008). Air–sea interaction over ocean fronts and eddies. *Dynamics of Atmospheres and Oceans*, 45(3-4):274–319.

Small, R. J., Tomas, R. A., and Bryan, F. O. (2014). Storm track response to ocean fronts in a global high-resolution climate model. *Climate dynamics*, 43(3-4):805–828.

Smirnov, D., Newman, M., Alexander, M. A., Kwon, Y.-O., and Frankignoul, C. (2015). Investigating the local atmospheric response to a realistic shift in the Oyashio sea surface temperature front. *Journal of Climate*, 28(3):1126–1147.

Smith, R. K. and Montgomery, M. T. (2016). Understanding hurricanes. *Weather*, 71(9).

Solomon, S. (2007). *Climate change 2007-the physical science basis: Working group I contribution to the fourth assessment report of the IPCC*, volume 4. Cambridge University Press.

Stenchikov, G., Hamilton, K., Stouffer, R. J., Robock, A., Ramaswamy, V., Santer, B., and Graf, H.-F. (2006). Arctic Oscillation response to volcanic eruptions in the IPCC AR4 climate models. *Journal of Geophysical Research: Atmospheres*, 111(D7).

Stocker, T., Qin, D., Plattner, G., Tignor, M., Allen, S., and Boschung, J. (2013). IPCC, 2013: Summary for policy makes in climate change 2013: The physical science basis. Contribution of working group I to the fifth assessment report of the Intergovernmental Panel on Climate Change.

Stommel, H. (1948). The westward intensification of wind-driven ocean currents. *Eos, Transactions American Geophysical Union*, 29(2):202–206.

Strachan, J., Vidale, P. L., Hodges, K., Roberts, M., and Demory, M.-E. (2013). Investigating global tropical cyclone activity with a hierarchy of AGCMs: The role of model resolution. *Journal of Climate*, 26(1):133–152.

Stull, R. (2011). *Meteorology for Scientists and Engineers, 3rd Ed. Chapter 13*. Univ. of British Columbia.

Taylor, A. H. and Stephens, J. A. (1998). The North Atlantic oscillation and the latitude of the Gulf Stream. *Tellus A*, 50(1):134–142.

Thiébaux, J., Rogers, E., Wang, W., and Katz, B. (2003). A new high-resolution blended real-time global sea surface temperature analysis. *Bulletin of the American meteorological Society*, 84(5):645–656.

Thompson, D. W., Lee, S., and Baldwin, M. P. (2003). Atmospheric processes governing the northern hemisphere annular mode/North Atlantic oscillation. *Geophysical Monograph-American Geophysical Union*, 134:81–112.

Torn, R. D. and Snyder, C. (2012). Uncertainty of tropical cyclone best-track information. *Weather and Forecasting*, 27(3):715–729.

Trenberth, K. E., Cheng, L., Jacobs, P., Zhang, Y., and Fasullo, J. (2018). Hurricane Harvey links to Ocean Heat Content and Climate Change Adaptation. *Earth's Future*.

Vallis, G. K. and Gerber, E. P. (2008). Local and hemispheric dynamics of the North Atlantic Oscillation, annular patterns and the zonal index. *Dynamics of atmospheres and oceans*, 44(3):184–212.

Vannière, B., Czaja, A., Dacre, H., and Woollings, T. (2017a). A "Cold Path" for the Gulf Stream–Troposphere Connection. *Journal of Climate*, 30(4):1363–1379.

Vannière, B., Czaja, A., Dacre, H., Woollings, T., and Parfitt, R. (2016). A potential vorticity signature for the cold sector of winter extratropical cyclones. *Quarterly Journal of the Royal Meteorological Society*, 142(694):432–442.

Vannière, B., Czaja, A., and Dacre, H. F. (2017b). Contribution of the cold sector of extratropical cyclones to mean state features over the Gulf Stream in winter. *Quarterly Journal of the Royal Meteorological Society*, 143(705):1990–2000.

Vecchi, G. A. and Knutson, T. R. (2008). On Estimates of Historical North Atlantic Tropical Cyclone Activity. *Journal of Climate*, 21(14):3580–3600.

Vecchi, G. A. and Knutson, T. R. (2011). Estimating annual numbers of Atlantic hurricanes missing from the HURDAT database (1878-1965) using ship track density. *Journal of Climate*, 24(6):1736–1746.

Velden, C. S. and Leslie, L. M. (1991). The basic relationship between tropical cyclone intensity and the depth of the environmental steering layer in the Australian region. *Weather and Forecasting*, 6(2):244–253.

Visbeck, M., Chassignet, E. P., Curry, R. G., Delworth, T. L., Dickson, R. R., and Krahmann, G. (2003). The ocean's response to North Atlantic Oscillation variability. *The North Atlantic Oscillation: climatic significance and environmental impact*, 134:113–145.

Vitart, F. (2006). Seasonal forecasting of tropical storm frequency using a multi-model ensemble. *Quarterly Journal of the Royal Meteorological Society*, 132(615):647–666.

Wallace, J. M., Mitchell, T., and Deser, C. (1989). The influence of sea-surface temperature on surface wind in the eastern equatorial Pacific: Seasonal and interannual variability. *Journal of Climate*, 2(12):1492–1499.

Wallace, J. M., Smith, C., and Jiang, Q. (1990). Spatial patterns of atmosphere-ocean interaction in the northern winter. *Journal of Climate*, 3(9):990–998.

Walsh, K., Fiorino, M., Landsea, C., and McInnes, K. (2007). Objectively determined resolution-dependent threshold criteria for the detection of tropical cyclones in climate models and reanalyses. *Journal of climate*, 20(10):2307–2314.

Wang, B. and Chan, J. C. (2002). How strong ENSO events affect tropical storm activity over the western North Pacific. *Journal of Climate*, 15(13):1643–1658.

Webster, P. J., Holland, G. J., Curry, J. A., and Chang, H.-R. (2005). Changes in tropical cyclone number, duration, and intensity in a warming environment. *Science*, 309(5742):1844–1846.

Wernli, B. H. and Davies, H. C. (1997). A Lagrangian-based analysis of extratropical cyclones. I: The method and some applications. *Quarterly Journal of the Royal Meteorological Society*, 123(538):467–489.

Wilks, D. S. (2016). "The stippling shows statistically significant grid points": How research results are routinely overstated and overinterpreted, and what to do about it. *Bulletin of the American Meteorological Society*, 97(12):2263–2273.

Woollings, T. (2011). Ocean effects of blocking. *Science*, 334(6056):612–613.

Woollings, T., Barriopedro, D., Methven, J., Son, S.-W., Martius, O., Harvey, B., Sillmann, J., Lupo, A. R., and Seneviratne, S. (2018). Blocking and its response to climate change. *Current Climate Change Reports*, 4(3):287–300.

Woollings, T., Gregory, J. M., Pinto, J. G., Reyers, M., and Brayshaw, D. J. (2012). Response of the North Atlantic storm track to climate change shaped by ocean–atmosphere coupling. *Nature Geoscience*, 5(5):313.

Woollings, T., Hoskins, B., Blackburn, M., and Berrisford, P. (2008). A new Rossby wave–breaking interpretation of the North Atlantic Oscillation. *Journal of the Atmospheric Sciences*, 65(2):609–626.

Wu, L. and Liu, Z. (2005). North Atlantic decadal variability: Air–sea coupling, oceanic memory, and potential Northern Hemisphere resonance. *Journal of Climate*, 18(2):331–349.

Wu, L., Wen, Z., Huang, R., and Wu, R. (2012). Possible linkage between the monsoon trough variability and the tropical cyclone activity over the western North Pacific. *Monthly Weather Review*, 140(1):140–150.

Xiao-qin, L. and Bing-ke, Z. (2013). Analysis of the climatic characteristics of landing tropical cyclones in east China. *Journal of Tropical Meteorology*, 19(2):145–153.

Xie, S., Lin, W., and Zhang, G. (2017). Is convection sensitive to model vertical resolution and why? In *AGU Fall Meeting Abstracts*.

Xie, S.-P. (2004). Satellite observations of cool ocean–atmosphere interaction. *Bulletin of the American Meteorological Society*, 85(2):195–208.

Zappa, G., Shaffrey, L. C., and Hodges, K. I. (2013a). The ability of CMIP5 models to simulate North Atlantic extratropical cyclones. *Journal of Climate*, 26(15):5379–5396.

Zappa, G., Shaffrey, L. C., Hodges, K. I., Sansom, P. G., and Stephenson, D. B. (2013b). A multimodel assessment of future projections of North Atlantic and European extratropical cyclones in the CMIP5 climate models. *Journal of Climate*, 26(16):5846–5862.

Zehr, R. M. (1992). Tropical cyclogenesis in the western North Pacific. Technical report, Colorado State University.

Zeng, Z., Wang, Y., and Wu, C.-C. (2007). Environmental dynamical control of tropical cyclone intensity-An observational study. *Monthly weather review*, 135(1):38–59.

Zhan, R. and Wang, Y. (2016). CFSv2-based statistical prediction for seasonal accumulated cyclone energy (ACE) over the western North Pacific. *Journal of Climate*, 29(2):525–541.

Zhan, R., Wang, Y., and Lei, X. (2011). Contributions of ENSO and East Indian Ocean SSTA to the interannual variability of northwest pacific tropical cyclone frequency. *Journal of Climate*, 24(2):509–521.

Zhan, R., Wang, Y., and Ying, M. (2012). Seasonal forecasts of tropical cyclone activity over the western North Pacific: A review. *Trop. Cyclone Res. Rev*, 1:307–324.

Zhao, M., Held, I., Vecchi, G., Scoccimarro, E., Wang, H., Wehner, M., Lim, Y., LaRow, T., Camargo, S., Walsh, K., et al. (2013). Robust direct effect of increasing atmospheric CO2 concentration on global tropical cyclone frequency—a multi-model inter-comparison. *CLIVAR Var, Fall*.

Zhao, M., Held, I. M., Lin, S.-J., and Vecchi, G. A. (2009). Simulations of global hurricane climatology, interannual variability, and response to global warming using a 50-km resolution GCM. *Journal of Climate*, 22(24):6653–6678.